
SAPIENZA
UNIVERSITÀ DI ROMA

**Sapienza University of Rome**

Department of Mechanical and Aerospace Engineering
PhD in Aeronautical and Space Engineering

Thesis For The Degree Of Doctor Of Philosophy

# Multi-physics thermal characterization of rocket combustion chambers

Advisor
**Prof. Francesco Creta**

Co-Advisor
**Dr. Pasquale E. Lapenna**

Candidate
**Arianna Remiddi**
**1608595**

**Academic Year 2021/2022 (XXXV cycle)**

*The important thing is not to stop questioning.*
*Albert Einstein*

## Abstract

This thesis is devoted to the numerical modeling and thermal characterization of technological devices based on combustion and operating under severe thermodynamic conditions.
Several approaches are proposed throughout the thesis, sharing the same tabulated chemistry approach for the turbulent combustion modeling and the implementation in Unsteady Reynolds Averaged Navier-Stokes settings. First, single-region solvers will be discussed, dealing only with the modeling of the fluid domain. This approach is selected to collect a significant amount of data at a reasonable computational cost, allowing therefore parametric investigations and the development of data-driven models. Such analyses will be mainly devoted to the assessment of the effect of geometrical and injection parameters over the flow field and thermal load in a combustion chamber. The information gathered through the parametric analyses is then used as stepping stone for the preliminary implementation of a data-driven model for the thermal characterization of complex multi-injector geometries.
The fidelity of the approach will be then increased including also the description of the heat transfer across different continua, through the simulation of multi-region test cases and hence introducing the coupled simulation of fluid and solid domains. In order to do so, a multi-region solver for Conjugate Heat Transfer is developed, featuring an interface boundary condition that guarantees temperature and heat flux continuity across the interfaces between an arbitrary number of solid and fluid domains. Also, an efficient coupling strategy aimed to the further reduction of the computational costs in convection-dominated phenomena is developed, based on the alternation between the two major approaches for coupled simulations found in the literature: directly coupled approach with Conjugate Heat Transfer and thermally chained simulations. Such a strategy will allow for the description of laboratory-scale test cases for the entire duration of the experimental runs. An extension of the solver will be also presented, accounting for pressure-dependence effects and allowing therefore the simulation of low-to-high Mach number flows such as the nozzle expansion downstream a combustion chamber.
The main applications to which the thesis work is devoted are non-premixed, turbulent flames in combustion chambers under high pressure operating conditions, representative of the conditions encountered in Liquid Rocket Engines, simulated in both two-dimensional and three-dimensional settings. Nonetheless, a brief excursus on premixed injection modeling, relevant to gas turbine and aeronautical applications, will be given in the final section of the thesis, with particular reference to the peculiar challenges raised by this type of flames. More specifically, the topic of premixed hydrogen combustion will be tackled. Hydrogen flames present several modeling challenges, starting from the higher flame temperatures and laminar flame speeds compared to other conventional fuels, to the intrinsic instabilities that characterize premixed flames, that can be generated by either thermo-diffusive or hydrodynamic effects. A data-driven tabulated chemistry approach for premixed hydrogen combustion modeling will be proposed.

# Contents

# List of Figures

# List of Tables

# List of publications

Part of the results presented in this thesis have been already presented in international conferences and published in peer-reviewed scientific journals. A list of published papers is presented below, together with presentations given at international conferences.

**Journals**

- G. Indelicato, P. E. Lapenna, **A. Remiddi** and F. Creta. *"An efficient modeling framework for wall heat flux prediction in rocket combustion chambers using non adiabatic flamelets and wall-functions"*. 2021 International Journal of Heat and Mass Transfer 169, 120913
- (*in press*) **A. Remiddi**, G. Indelicato, P. E. Lapenna, F. Creta, *"Efficient time-resolved thermal characterization of single and multi-injector rocket combustion chambers"*, Proceedings of the Combustion Institute.
- G. Indelicato, **A. Remiddi**, P. E. Lapenna, F. Creta, N. P. Longmire, and D. T. Banuti, *"Dataset of Wall-Resolved Large-Eddy Simulations Turbulent Pseudoboiling in Cryogenic Hydrogen Pipe Flows"*, Journal of Thermophysics and Heat Transfer 0 0:0, 1-14
- (*in press*) **A. Remiddi**, P. E. Lapenna, G. Indelicato, M. Valorani, M. Pizzarelli, F. Creta, *"Heat transfer in rocket combustion chambers firing plates: role of injector confinement"*, Journal of Propulsion and Power.

**Conferences**

- **A. Remiddi**, G. Indelicato, R. Lamioni, P. E. Lapenna and F. Creta. *"Numerical investigation of confinement effects on a supercritical LOX-Methane flame"* 42nd Meeting the Italian Section of the Combustion Institute. Ravenna, Italy-2019.
- G. Indelicato, F. Vona, **A. Remiddi**, P. E. Lapenna and F. Creta. *"A flamelet-based numerical framework for the simulation of low-to-high Mach number flows in LRE"*. 2020 Joint Propulsion Conference, AIAA, Propulsion and Energy Forum and Exposition. Virtual.
- **A. Remiddi**, G. Indelicato, P. E. Lapenna, F. Creta. *"Effects of injector lateral confinement on LRE wall heat flux characterization: numerical investigation towards data-driven modeling"*. 2021 AIAA Scitech Forum, 0416. Virtual.
- G. Indelicato, **A. Remiddi**, P. E. Lapenna, F. Creta. *"Application of wall functions approaches in the context of LRE combustion chambers simulations"*. 2021 AIAA Scitech Forum, 1375. Virtual.
- **A. Remiddi**, G. Indelicato, P. E. Lapenna, F. Creta. *"Thermal characterization in LRE: a parametric analysis on injector arrangement"*. 2021 AIAA Propulsion and Energy Forum, 3567. Virtual.
- **A. Remiddi**, G. Indelicato, P.E. Lapenna, F. Creta, *"A flamelet-based numerical framework for Conjugate Heat Transfer in LRE relevant conditions"*, AIDAA XXVI International Congress, 2021. Virtual.

- P. E. Lapenna, **A. Remiddi**, G. Indelicato, M. Pizzarelli, M. Valorani, F. Creta, *"Towards high-fidelity numerical simulations of injectors near-field in LRE combustion chambers"*,AIDAA XXVI International Congress, 2021. Virtual.
- D. Cavalieri, G. Indelicato, **A. Remiddi**, P.E. Lapenna, F. Creta, *"Theoretical and numerical modelling of multicomponent transcritical diffuse interfaces"*, AIDAA XXVI International Congress, 2021. Virtual.
- **A. Remiddi**, G. Indelicato, P. E. Lapenna, F. Creta. *"Multi-physics modeling of Liquid Rocket Engine combustion chambers"*, 43rd Meeting of the Italian Section of the Combustion Institute, Ischia (NA), Italy-2021.
- G. Indelicato, **A. Remiddi**, P. E. Lapenna, F. Creta. *"From turbulent combustion to Liquid Rocket Engines: an overview of applications"*, 43rd Meeting of the Italian Section of the Combustion Institute, Ischia (NA), Italy-2021.
- **A. Remiddi**, G. Indelicato, P. E. Lapenna, F. Creta. *"Development and validation of an efficient numerical framework for Conjugate Heat Transfer in Liquid Rocket Engines"*. 2022 AIAA Scitech Forum, 2119. Virtual.
- G. Indelicato, P. E. Lapenna, N. P. Longmire, **A. Remiddi**, D. T. Banuti, F. Creta. *"Dataset of wall-resolved large eddy simulations for the investigation of turbulent pseudo-boiling and wall-functions in cryogenic hydrogen pipe flows"*. 2022 AIAA Scitech Forum, 0339. Virtual.
- **A. Remiddi**, G. Indelicato, P. E. Lapenna, F. Creta, *"Multi-region thermal characterization in LRE combustion chambers"*, Conference: EUCASS 3AF 2022 (9th European Conference for Aeronautics and Space Sciences), 2022. Lille, France.
- P. E. Lapenna, **A. Remiddi**, G. Indelicato, M. Valorani, M. Pizzarelli, F. Creta, *"Characterization of the injectors near-field region of LRE combustion chambers"*, Conference: EUCASS 3AF 2022 (9th European Conference for Aeronautics and Space Sciences), 2022. Lille, France.
- G. Indelicato, **A. Remiddi**, P. E. Lapenna, F. Creta, *"Validation and development of wall-function models for Liquid Rocket Engine applications"*, Conference: EUCASS 3AF 2022 (9th European Conference for Aeronautics and Space Sciences), 2022. Lille, France.
- P. E. Lapenna, **A. Remiddi**, G. Indelicato, F. Creta. *"A data driven Filtered Wrinkled Flamelet model for premixed hydrogen-air flames"*, 44th Meeting of the Italian Section of the Combustion Institute, Naples, Italy-2021.

**Author's details**

ORCID: https://orcid.org/0000-0002-3604-4879

Scopus ID: 57219112384

# Chapter 1

# Introduction

**Contents**



High pressure combustion is at the basis of many high energy density systems, ranging the spectrum of interest from power generation cycles, to aeronautical engines and eventually to space transportation systems. The tendency to operate at increasingly higher pressures is dictated by the demand of increasingly higher performance: it is in fact known, that the combustion intensity scales with pressure, leading to an higher energy released per unit volume, and therefore an higher efficiency. Concurrently, in the majority of the propulsion systems, such operating conditions have the additional beneficial effect of allowing to reduce the size of engine and tankage. Such severe operating conditions have however some crucial drawbacks, most notably the increase of the thermal load over the walls, which therefore require active cooling systems to avoid thermal failures. These circumstances worsen the already critical issue of thermal management, a problem that is particularly adverse when dealing with complex structures that make the experimental investigations prohibitive.

## 1.1 The role of numerical investigations

Thanks to the growth of the High Performance Computing (HPC) capabilities, experimental testing has been increasingly replaced by numerical modeling. Computational Fluid Dynamics (CFD) is becoming in this context a major design tool, providing a twofold advantage. For one thing, CFD can actively support the design phase of real engine configurations, acting as a surrogate of experimental tests and reducing therefore significantly the development time and costs. Secondly it can shed light on the complex and interrelated phenomena occurring inside a combustion

chamber. The degree of fidelity of the numerical approach must adapt to the dimensions of the sought target: if on one side understanding of the physical phenomena underlying the turbulent high-pressure combustion requires the highest resolution and can be achieved only by means of high-fidelity DNS simulations, although limited to paradigmatic configurations, on the other side the characterization of industrial- or laboratory-scale configurations requires the recourse to some stiffness-reduction techniques and can be efficiently tackled only by LES or URANS simulations. The numerical simulation of high-pressure, turbulent, multi-physics flows is however not lacking in challenges representing therefore still an open research topic [5, 94]. Among the many, it is worth mentioning the wide range of spatial and time scales characterizing the turbulent reacting flows, to which are added the scales of the physical phenomena which are not directly related to the combustion process but represent its direct contour, e.g. convective or radiative heat transfer and interaction with surrounding structures. Specific modeling solutions must be sought and applied depending on the peculiarity of the configuration considered. A preliminary classification of the applications that will be dealt with in this thesis can be made based on the combustion regime, either diffusive or premixed. The major challenges raised by each class of applications will be discussed in the following Sections, together with a literature survey on the main approaches employed by the scientific community.

## 1.2 Rocket combustion chambers

Propulsion systems for space transportation are probably one of the most extreme applications for high energy density systems based on combustion. In particular, space agencies and private companies have been recently engaged in the development of next-generation Liquid Rocket Engines (LRE) characterized by the non-premixed Oxygen-Methane combustion [4, 6, 35, 78, 104]. The interest in such propellant combination comes from its high performance, featuring the highest specific impulse among hydrocarbons as well as its sustainability and reusability characteristics [96]. The remarkable reusability characteristics are mainly given by the low rate of coking in regenerative cooling systems [69] and the limited tendency to soot production in the combustion chamber [59]. Convective and radiative heat transfer, propellant mixing and high-pressure turbulent combustion are only some of the physical phenomena involved, making the LRE propulsion system design an intrinsically multi-scale problem.

### 1.2.1 The problem of thermal characterization

Given the extreme operating conditions of LRE thrust chambers, the thermal characterization is a key aspect of the design process, directly influencing the engine reliability, operating life and possible reusability. The operating life of a LRE is typically governed by the thermal loads to be sustained in the most thermally solicited part, which is the throat region [91, 92]. For this reason the lateral part of the combustion chamber, as well as the nozzle sections have been largely investigated by means of numerical simulations using various approaches [10]. However, in the context of reusability and the ensuing increased attention to the entire system, more detailed analyses of the injection region are expected to be of interest. The whole injection region, especially the injector's faceplate, lacks a dedicated and thorough investigation in the recent literature in terms of a

complete thermal characterization. This is hindered by the lack of experimental data, due to the actual difficulty in accessing the faceplate with experimental probes. The most common assumption adopted is therefore to consider the faceplate as represented by the adjacent and more instrumentally accessible combustion chamber lateral wall [105, 120]. A detailed knowledge of the thermal loads in the injection region, however, is crucial for the optimal design of an engine, as suggested by Suslov et al. in [113].

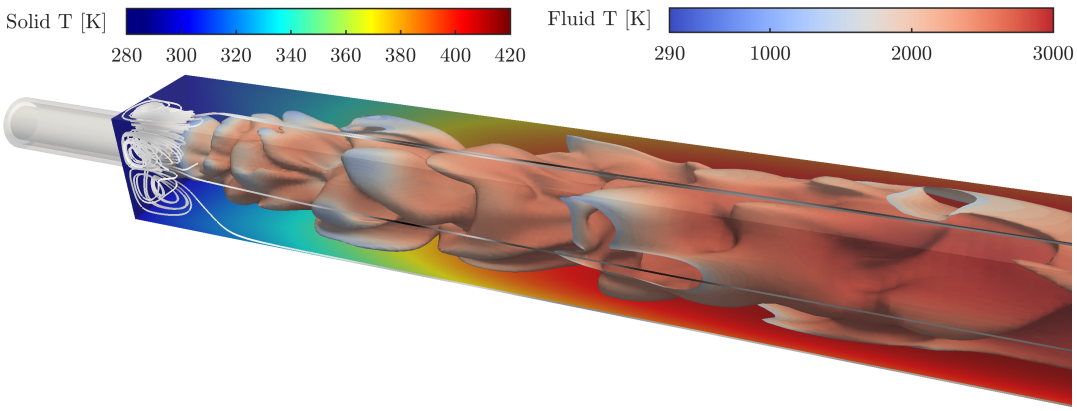


**Figure 1.1:** Zoomed view of the injection region in the TUMrig combustor. Istantaneous isosurface of the stoichiometric mixture fraction colored by temperature, with superimposed streamlines of the time-averaged velocity field.

### 1.2.2 Non-premixed literature survey

A plethora of numerical studies have recently focused on the prediction of the turbulent mixing and combustion of gaseous oxygen and gaseous methane (GOx/GCH4), as well as the thermal characterization of LREs withstanding extreme heat fluxes on the order of several MW/m$^2$ [10]. The approaches devoted to the LRE characterization are limited to the middle- and lower-fidelity Reynolds averaged Navier Stokes (RANS) and Large Eddy Simulations (LES) due to the large dimension of the configurations studied and their prohibitive computational costs. RANS approaches have been used to increase the predicting capabilities on heat fluxes as well as assessing numerical methods and parameters, see among many [16, 54, 80, 85]. With the purpose of the stiffness reduction, significant research efforts have also been devoted to the modeling of thermal boundary layers, taking advantage of wall modeled approaches using both algebraic [37] and ODE based models [79]. Moving towards higher fidelity approaches, LES simulations have been presented by many groups [19, 72, 84, 129] with the aim of shedding light on combustion processes and its impact on heat flux prediction. A number of experimental works are also available in the literature, this thesis will mainly refer to the single and multi-injector Methane-Oxygen combustor facilities, developed at the Technical University of Munich (TUM) [15, 83, 122].

#### Injection region

As already mentioned, the literature specifically devoted to the investigation of the injection region is rather limited. Schacht and Quentmeyer in [105] perform an experimental study on the axial

and circumferential variations of heat transfer rates, but still assuming the injector faceplate to be represented by the first station of the hot-gas lateral side of the combustion chamber. Similar hypotheses are employed by Wheeler and Kirby in [120] where due to to the difficulties in measuring injector face heat transfer coefficient, the latter is assumed to be equal to the value determined on the lateral wall near the injector. More recently, the thermal load in the injection region has been investigated by Betti [9] using a simplified pseudo-injectors approach.

**Parametric analyses and data-driven models**

The recourse to lower-fidelity approaches however, paves the way to the collection of a large amount of data, allowing therefore for parametric investigations and for the development of data-driven models. Analysis of coaxial injector parameters such as the thickness of the liquid oxygen post can be found in the work by Xu et al. [124], and a study of thermal boundary condition effect on swirl flames has been proposed by Ahdy et al. in [1]. An investigation of the effects of pressure and wall temperature for different propellants combination is proposed by Betti et al. in [10]. The recent work by Krügener et al. [54] presents the collection of a large database of two-dimensional RANS simulations generated varying several parameters both releated to the combustor geometry and operative conditions. Such a database is then used to train surrogate models of different fidelities using Deep Learning techniques.

**Coupled approaches**

As for the numerical investigation of the interaction between the hot-gas-side in LRE and the surrounding walls and cooling systems, several approaches can be found in the literature, and can be classified into two main categories. The class of *directly coupled* methods entails the simultaneous solution of fluid and solid domains, coupled at the interface through a Conjugate Heat Transfer (CHT) condition, enforcing temperature and heat flux continuity. Due to its significant computational cost, this method is mainly devoted to steady-state operations, as in the recent work by Rahn et al. [98], or to mono-species coolant flows, as done by Pizzarelli et al. in [93]. *Loose coupling* methods are instead based on the so-called thermal chaining technique, i.e. the alternate solution of single domains, either fluid or solid, with the subsequent imposition of one domain as boundary condition for the other. These methods require the assumption of a first guess initial condition, but guarantee a lower computational effort and are therefore more commonly applied to LRE [72, 83]. An intermediate solution is found in the literature for actively cooled combustion chambers, where a CHT condition is enforced between the solid wall and the coolant flows, while the coupling between the reacting flow and the solid structure is modeled through a thermally chained simulation. These works differs for the quantity that is iteratively imposed from one domain to the other: Song et al. and Rahn et al. in [97, 111] resort to the enforcement of heat flux conditions, while Betti et al. in [11] suggest a formulation in terms of heat transfer coefficient values.

## 1.3 Premixed combustion

In the context of high energy density systems, premixed combustion is better found in gas-turbines and aeronautical applications. Premixed flames are usually characterized by intrinsic instabilities

induced by the large temperature and density gradients due to the great amount of energy released by chemical reactions. The interaction of such instabilities with turbulence makes the turbulent premixed combustion a multi-scale phenomena still requiring some understanding and modeling [21, 53, 63].
Among the several applications of premixed combustion, hydrogen combustion has recently established itself as among the most efficient energy conversion procedures in the scenery of decarbonization and low-carbon economy since it releases just clean water as main product without generating any carbon dioxide, and is therefore attractive for a plethora of industrial applications: to name a few, hydrogen can act as main propellant in space transportation systems but also as green energy carrier in energy-intensive industries or in household burners. In aviation hydrogen is regarded as a potential fuel for medium range aircraft, guaranteeing lower costs and climate impact. Being a continuous energy source, hydrogen combustion can also solve the problem of daylight or seasonal intermittency of other sustainable sources.

### 1.3.1 The case of hydrogen combustion

Premixed hydrogen flames present several modeling challenges, starting from the higher flame temperatures and laminar flame speeds with respect to conventional fuels, to the aforementioned intrinsic instabilities that characterize premixed flames. These occur with two main mechanisms: the *Darrieus-Landau or hydrodynamic instabilities* (DL) and the *thermo-diffusive instabilities* (TD) [75]. The former are caused by the large density jumps across the flame front, which induce velocity changes and deviation of the streamlines. This leads in its turn to the wrinkling of the flame, with a perturbating effect which is always destabilizing [22, 76]. The TD instability instead, is the consequence of the disparity between the thermal conductivity of the mixture and the molecular diffusivity of the controlling reactant. The unbalance between these two terms causes local changes in the mixture composition and in the corresponding reaction rates, leading to changes in the flame speed and eventually to wrinkling that can be either stabilizing or destabilizing depending on the Lewis number of the controlling reactant [63, 66].
Hydrogen flames, being typically characterized by low Lewis numbers, are typically subject to small scale thermodiffusive instability, that cause the formations of small-scale cellular structures with localized quenching and have therefore a destabilizing effect and eventually interacts with the hydrodynamic instabilities causing increases of the flame speed of three to five times its stable value [8]. In this scenario, numerical simulations are fundamental for the understanding of the flame behaviour, but are still a challenging task when computational domains tend to the laboratory scale, becoming even prohibitive when approaching to the industrial scale.

### 1.3.2 Premixed literature survey

Several experimental investigations on the use of hydrogen premixed combustion in industrial-scale facilities have been conducted, usually referring to swirl-stabilized injection [17, 18, 24, 106]. On the numerical side, however, the simulation of a turbulent, high-pressure, premixed hydrogen flame remains a crucial issue.
High-fidelity DNS simulations have been performed for two-dimensional rectangular domains by Kadowaki et al. [43, 44], Sharpe and Falle [107] and Yuan et al. [126]. These studies were devoted

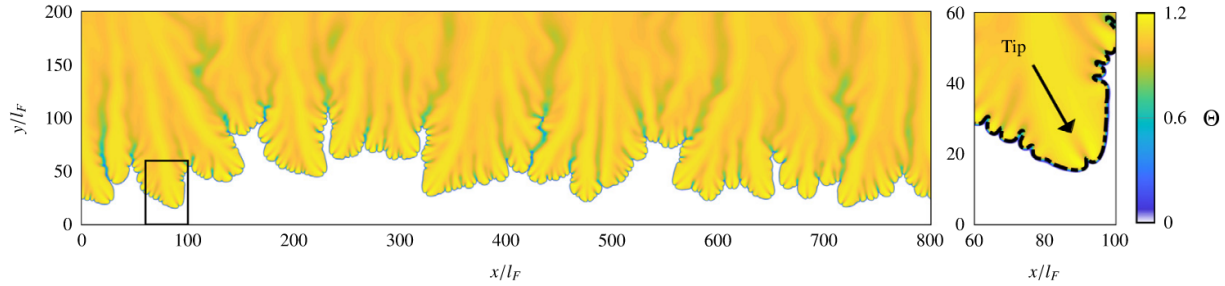


**Figure 1.2:** Normalized temperature for the large-scale DNS by Berger et al. [8].

to the propagation of an initially planar flame and report the formation of cellular structures along the flame front. Large cusped-like structured were identified in the simulations by Altantzis et al. and Frouzakis et al. [2, 29], both featuring detailed chemistry and variable transport coefficients. More recently, a dataset of two-dimensional DNS simulation of multi-step chemistry hydrogen/air premixed flames has been collected by Berger et al. [8] to investigate the occurrence of unstable flame structures and to assess therefore the characteristic scales of the flame front corrugations. The propagation of premixed flames subject to both hydrodynamic and thermodiffusive instabilities has also been investigated by Creta et al. in [22] through the collection of a DNS database of large scale flames.

### Tabulated approaches

Also in the case of premixed combustion, the lower-dimensional manifold representation typical of the flamelet-based models is a solution adopted aiming to reduce the cost of the numerical simulations. The baseline idea underlying these models is the assumption that the thermo-chemical reactions lie close to a very low-dimensional manifold and that the coupling with the fluid-dynamics can be parametrized by at most one or two variables [95]. Among the possible declinations of the tabulated approach, one of its original implementation is the F-TACLES approach [28]. It is based on the spatial filtering of a one-dimensional premixed detailed flame solution, in order to recover all the filtered quantities as functions of the filtered progress variable. The advantage of such a filtered tabulation compared to the approaches using a presumed PDF is that retains by construction the original stretched laminar flame speed also in absence of the turbulence leading to subgrid wrinkling [28]. An extension to this approach has been proposed by Lapenna et al. in [56], applied to corrugated and unsteady flames exhibiting thermal-diffusive instability effects. The idea is to retain the concept of the tabulated approach but employing a fully resolved, two-dimensional, unstable, self-wrinkling flame as starting solution for the filtering procedure. The recourse to a two-dimensional flame, as opposed to the one-dimensional steady flame used in other approaches, is mandatory to retain the main characteristics of intrinsically unstable flames, the paradigmatic structure of which is inherently multi-dimensional. It is observed that a thermochemical manifold parametrized by two independent variables gives a sufficiently accurate representation of the complex multi-scale, unsteady, stretched character of thermo-diffusively unstable flames, with a significant accuracy improvement with respect to the one-dimensional manifolds found in literature. Other tabulated approaches include the FPI (Flame Prolongation of ILDM) [31] and FGM (Flamelet Generated Manifolds) [118] methods. In both these approaches, the flame properties

are mapped onto a single scalar called progress variable under the hypothesis of fuel Lewis number close to unity. An extension to non-unity Lewis number combustion is proposed by Regele et al. in [101] where a two-scalars tabulated approach is presented, based on the original FPV-levelset (Flamelet Progress Variable) model [51, 52, 87, 88].

## 1.4 Objective and outline

The objective of this thesis is the numerical modeling of high energy density devices based on combustion. Among the many, two main issues will be addressed: the thermal characterization of rocket combustion chambers and the premixed combustion modeling typically found in devices for power generation. The first topic will be dealt with in more detail, addressing the thermal characterization of several configurations in the context of Liquid Rocket Engine applications and resorting to a numerical approach with scalable fidelity: ranging from the single-region simulation of combustion chambers under the low-Mach number assumption to the multi-region fully coupled simulation of low-to-high Mach number flows. Concerning the modeling of premixed injection, the case of hydrogen flames will be addressed through the development and preliminary validation of a tabulated chemistry model.

The following Chapters are organized as follows:

*Chapter 2: Theoretical modeling*

The theoretical aspects underlying the models enforced in the solvers are here presented and discussed. The flamelet-based approach is addressed, with particular attention to the frozen assumption, initially in the context of a low-Mach number approximation, then considering its extension to compressible cases. A brief overview on the employed wall modeling approaches is then presented, with particular reference to the thermal wall function of Han and Reitz and its adaptation to the LRE operative conditions. Finally the coupling conditions for the description of heat transfer across neighbouring continua are presented. Several coupling strategy are presented, resulting in a variable-fidelity approach guaranteeing the limitation of the overall computational costs.

*Chapter 3: Numerical framework*

The numerical implementation of the aforementioned models is discussed in this chapter. The resulting solvers are based on modified versions of the open-source OpenFOAM and OpenSMOKE++ frameworks. Remarks are given on the finite volume approach and the segregated solution strategy employed, with particular reference to the approaches used by the multi-region solver and to the coupling strategies enforced across the interfaces.

*Chapter 4: Single-region analysis of the thermal load in the injection region*

In this chapter the thermal load in a GOx/GCH4 combustion chamber is studied through a parametric analysis using a single-region solver. Several thermal boundary condition are enforced, both to mimic different injector configuration and to assess the effect of

the employed thermal modeling. Then, a consistent parametric analysis is performed, varying the lateral confinement length within a range of interest. From this, general trends about the confinement effects over the flow field and thermal load are gathered. Such data are then used as stepping stone for the development of a low-order, data-driven model for the preliminary thermal characterization of multi-injector combustion chambers.

*Chapter 5: Multi-region analysis of coupled combustion chambers*

Here the applications of the multi-region solver for the time-dependent characterization of rocket combustion chambers are presented. First, the code is validated by means of simple test-cases, i.e. a multi-layer plate with well-known analytical solution and a mono-species laminar backward facing step. Then the solver is applied to more complex configurations featuring turbulent reacting flows and reproducing the experimental runs of both single- and multi-injector configurations, in both two- and three-dimensional settings.

*Chapter 6: Single- and multi-region analysis of low-to-high Mach number flows*

In this chapter the accommodation of the solvers to account for compressible effects is presented. First the TUMrig combustor will be analyzed in a single-region setting through a parametric variation of the inlet mass flow in order to assess the effect on the ensuing thermal load. Then, a multi-region, coupled simulation of the same combustor is presented.

*Chapter 7: Towards the modeling of premixed hydrogen-air injection*

In the last section of this thesis the attention is moved towards the topic of premixed injection and combustion, with particular reference to hydrogen premixed flames. Such flames are characterized by some intrinsic instabilities and require therefore specific modeling solutions. This issue is introduced in Chap. 7 together with the development of a data-driven approach for LES simulations of unstable hydrogen premixed flames and its *a-priori* validation.

*Chapter 7: Conclusions*

# Chapter 2

# Theoretical modeling

## Contents



## Nomenclature

**Latin letters**

| | |
|---|---|
| $c_p$ | = Specific heat at constant pressure |
| $h$ | = Mixture enthalpy |
| $h_C$ | = Heat transfer coefficient |
| $h_{s,k}$ | = $k$-th species sensible enthalpy |
| $\Delta h^0_{f,k}$ | = $k$-th species heat of formation |
| $L$ | = Characteristic domain dimension |
| $n_s$ | = Number of species |
| $p$ | = Pressure |
| $q$ | = Heat flux |
| $t$ | = Time |
| $T$ | = Temperature |
| $U$ | = Velocity |
| $u_\tau$ | = Skin friction velocity |
| $y^+$ | = Wall unit |
| $Y_k$ | = $k$-th species mass fraction |
| $Z$ | = Mixture fraction |

**Greek letters**

| | |
|---|---|
| $\alpha$ | = Thermal diffusivity |
| $\Delta$ | = Numerical cell dimension |
| $\rho$ | = Density |
| $\lambda$ | = Thermal conductivity |
| $\Lambda_p$ | = Pressure ratio |
| $\phi$ | = Enthalpy defect |
| $\chi$ | = Scalar dissipation rate |
| $\psi$ | = Generic thermodynamic quantity |
| $\dot{\omega}_k$ | = $k$-th species reaction rate |
| $\dot{\omega}_T$ | = Temperature reaction rate |

| | |
|---|---|
| **Operators** | |
| $\widetilde{\cdot}$ = Favre average | $\square_{\mathrm{F}}$ = Fluid-side value |
| $\bar{\cdot}$ = Reynolds average | $\square_{\mathrm{int}}$ = Interface value |
| **Subscripts and superscripts** | $\square_{\mathrm{S}}$ = Solid-side value |
| $\square_{\mathrm{ad}}$ = Adiabatic value | $\square_t$ = Turbulent value |
| | $\square_w$ = Wall value |

In this Chapter the theoretical background of the main models employed is discussed. First, the tabulated approach for the thermo-chemistry problem is addressed, together with a number of model extension introduced to account for different effects, from turbulence and non-adiabaticity to compressibility and mono-species flows. Then a brief overview on the wall models is presented, followed by a description on the interface conditions usually employed in the multi-region solvers and by a novel coupling strategy proposed for a further stiffness reduction in convection-dominated phenomena.

## 2.1 Thermodynamic manifold

The combustion model used throughout the thesis is based on the traditional flamelet manifold approach [86], according to which a non-premixed flame can be represented as an ensemble of one-dimensional, laminar flames in the limit of high Damköhler number. Such one-dimensional flame structures are obtained solving the following flamelet equations, written in the space of the conserved scalar $Z$, called mixture fraction [48, 58]:

$$\frac{\partial Y_k}{\partial t} = \frac{1}{2}\chi\frac{\partial^2 Y_k}{\partial Z^2} + \frac{\dot{\omega}_k}{\rho} \tag{2.1}$$

$$\frac{\partial T}{\partial t} = \frac{1}{2}\chi\frac{1}{c_p}\Big[\frac{\partial^2 h}{\partial Z^2} + \sum_{k=1}^{n_s} h_k\frac{\partial^2 Y_k}{\partial Z^2}\Big] + \frac{\dot{\omega}_T}{c_p\rho} \tag{2.2}$$

where $Y_k$ is $k-$th species mass fraction, $\rho$ is the density of the mixture, $\chi$ represents the scalar dissipation rate of the mixture fraction which is usually parameterized as a function of its value $\chi_{st}$ at stoichiometric conditions [90], $T$ is the temperature, $\dot{\omega}_k$ and $\dot{\omega}_T = -\sum_k h_k\dot{\omega}_k$ are respectively the $k$-th species and temperature reaction rates, $c_p$ is the specific heat at constant pressure and $h$ is mixture enthalpy, defined as:

$$h = \sum_{k=1}^{n_s} Y_k h_k = \sum_{k=1}^{n_s} Y_k h_{s,k} + \sum_{k=1}^{n_s} Y_k \Delta h^0_{f,k} \tag{2.3}$$

being $h_{s,k}$ and $\Delta h^0_{f,k}$ the $k$-th species sensible enthalpy and heat of formation. The species are assumed to have constant and unitary Lewis numbers $Le_k = Le = 1$. The steady state solutions of the flamelet equations Eq. (2.1)- (2.2) represent the laminar thermochemical manifold.
This steady model is used since, under the hypothesis of high Damköhler numbers, unsteady flame features such as autoignition or quenching and re-ignition are not expected. More specifically, under rocket-like conditions, extremely elevated Damköhler numbers are experienced due to very small chemical timescales caused by the high pressures and by the absence of any inert species

in an oxy-combustion scenario. Under such conditions, the flame is invariably thinner than the small scale turbulent eddies and become almost insensitive to strain, while concurrently featuring extremely high quenching values for the strain rate or, equivalently, the scalar dissipation rate [58].

### 2.1.1 Including turbulence effects

In order to account for turbulence-chemistry interaction, the presumed Probability Density Function (PDF) approach is employed [94]. In this framework the laminar quantities $\psi$ are convoluted with a presumed multi-variate PDF:

$$\widetilde{\psi} = \int \psi(Z, \chi_{st}) \widetilde{P}(Z, \chi_{st}) dZ d\chi_{st} \tag{2.4}$$

in order to obtain the Favre filtered quantities $\widetilde{\psi} = \overline{\rho\psi}/\overline{\psi}$, where the overbar represents Reynolds averaging. The density-weighted, multi-variate PDF $P(Z, \chi_{st})$ is then modeled as the product of single-variate PDFs, assuming statistical independence between the variables. A beta-pdf is employed for the subgrid scale PDF of the mixture fraction using its mean value $\widetilde{Z}$ and its variance $\widetilde{Z''^2}$ as inputs [32], while a Dirac-delta distributions is used for the scalar dissipation, straightforwardly using its mean values $\widetilde{\chi}_{st}$. Such assumptions, in particular for the scalar dissipation rate, have shown to lead to reasonable results when unsteady simulations are carried out as done in the present work [62]. The values of $\widetilde{\psi}$ are computed and stored in the so-called flamelet tables, that can be written as follows:

$$\widetilde{\psi} = \widetilde{\psi}(\widetilde{Z}, \widetilde{Z''^2}, \widetilde{\chi_{st}}). \tag{2.5}$$

From the CFD standpoint each thermochemical variable locally required by the solver is then looked-up from the flamelet libraries providing the set of inputs represented by Eq. (2.5). Transport equations are solved to obtain the mean mixture fraction and its variance.

### 2.1.2 Extension to non-adiabatic effects

An additional variable is needed in order to account for non-adiabatic effects. For the approach used in this thesis, developed and validated by Indelicato et al. [37], such variable is the enthalpy defect $\phi$, representing a measure of the deviations from the adiabatic conditions of the mixture. The enthalpy of the adiabatic mixture between two streams can be defined as $h_{\mathrm{ad}} = h_{\mathrm{ox}} + Z(h_{\mathrm{f}} - h_{\mathrm{ox}})$ being $h_{\mathrm{ox}}$ and $h_{\mathrm{f}}$ the enthalpy of the oxidizer and of the fuel at the injection conditions [47, 60, 61]. The employed method stems from the formulation of Marracino and Lentini [73] originally developed to model the non-adiabatic effects of radiation due to soot in non-premixed flames, in which the enthalpy defect is uniformly applied throughout the $Z$ space. However, when applied to different non-adiabatic conditions, this method can lead to unacceptable temperature values as discussed in [55]. To overcome this issue, a modified enthalpy profile in mixture fraction space $h(Z)$ is employed [37], in which the maximum enthalphy loss is expected to occur at stoichiometric mixture fraction $Z_{st}$ without any enthalpy loss at the flamelet boundaries $Z = 0$ and $Z = 1$:

$$h(Z; \phi) = h_{\mathrm{ad}}(Z) - \phi f(Z; Z_{st}) \tag{2.6}$$

where $f(Z; Z_{\mathrm{st}})$ is a piece-wise linear function in $Z \in [0, 1]$ modulating the defect, defined as:

$$f(Z, Z_{\mathrm{st}}) = \begin{cases} \frac{Z}{Z_{\mathrm{st}}} & Z \leq Z_{\mathrm{st}} \\ 1 - \frac{Z - Z_{\mathrm{st}}}{1 - Z_{\mathrm{st}}} Z > Z_{\mathrm{st}} \end{cases} \tag{2.7}$$

The enthalpy profile is then fully characterized by means of the user-prescribed enthalpy defect $\phi$, spanning from $0$ kJ/kg up to flame quenching.

**Choice of the non-adiabatic model assumption**

The quenching value defined as upper bound of the enthalpy defect depends on additional non-adiabatic model assumptions made. Two of the approaches investigated in [37], namely the fully non-adiabatic or the frozen approach, are briefly described in the following.

- **Fully non-adiabatic (NA)**
  According to this approach both the temperature and species mass fractions are influenced by non-adiabatic effects, with the local reacting mixture responding to the heat losses instantaneously. The NA flamelets can be computed by solving Eq.(2.1) for $Y_k$ while imposing the enthalpy profile of Eq.(2.6) for each $\phi$ selected.

- **Semi-adiabatic or frozen (F)**
  In this approach, the composition of the reacting mixture is not influenced by non-adiabatic effects which leads only to a local temperature reduction. As a result, it is assumed that the species reaction rates become progressively smaller as the flame is influenced by non-adiabatic effects, inhibiting the occurrence of any further reaction close to the wall. Operatively the frozen flamelets are computed starting from the adiabatic flamelet profile and then applying the enthalpy defect of Eq.(2.6) to obtain the reduced flame temperature.

Throughout this thesis the frozen approach is used due to its better performance in terms of heat flux predictions in particular in proximity of the injection region. Moreover, the frozen approach is by construction compatible with the thermal wall-functions. As discussed by Indelicato et al. [37], in fact, although being rather arbitrary, the present frozen, piece-wise non-adiabatic model represents an efficient and effective way to avoid unphysical temperatures and, concurrently, have predictive capabilities on the heat flux at the walls. In addition, this approach is rather similar to the one proposed by Kim et al. [47] in which the non-adiabatic enthalpy profile is modelled using a different function $f$. Conversely, other approaches are based on additional source terms in the flamelet equations [67] or modifications to the flamelet progress variable approach [34, 50]. In addition, two other approaches have been tested by Wollny et al. [123] namely the heat release damping (HRD) method and the artificial radiation (AR) method. The former features a scaled chemical source term in the energy equation of the flamelets by means of a constant and arbitrary damping factor, while the latter provides an augmented radiative source term. More recently, a permeable thermal boundary condition was employed by Ma et al. [71] in the solution of counter-flow diffusion flames used instead of the flamelet equations. This method has also been employed and compared to other strategies by Zips et al. [128], assessing that the impact on heat flux estimation of these strategies is rather limited.

This being said the generic, laminar thermochemical property $\psi$ can expressed as a function of $Z$ as well as $\chi_{st}$ and $\phi$ as parameters:

$$\psi = \psi(Z; \chi_{st}, \phi). \tag{2.8}$$

When considering the interaction of turbulence, a delta-Dirac distribution of the presumed PDF is used for $\phi$. Figures 2.1 and 2.2 show respectively the effect of variable enthalpy defect $\phi$ and of variable scalar dissipation $\chi_{st}$ on the temperature profile, according to the semi-adiabatic model.

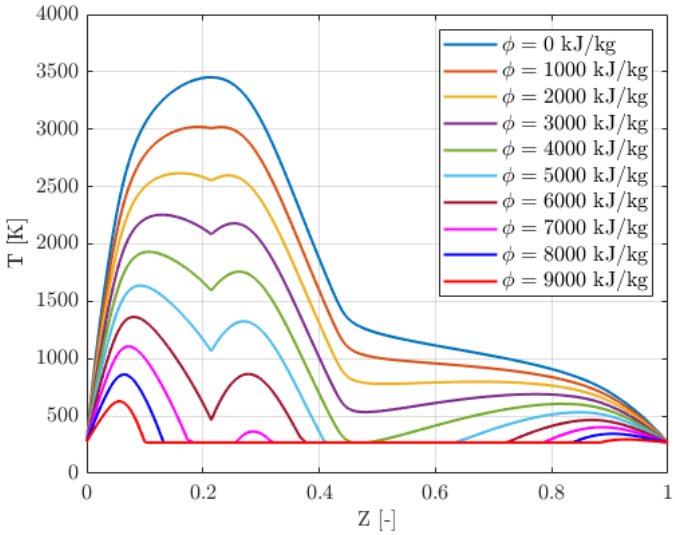


**Figure 2.1:** Effect of variable enthalpy defect on temperature ($\chi_{st} = 0\ s^{-1}$).

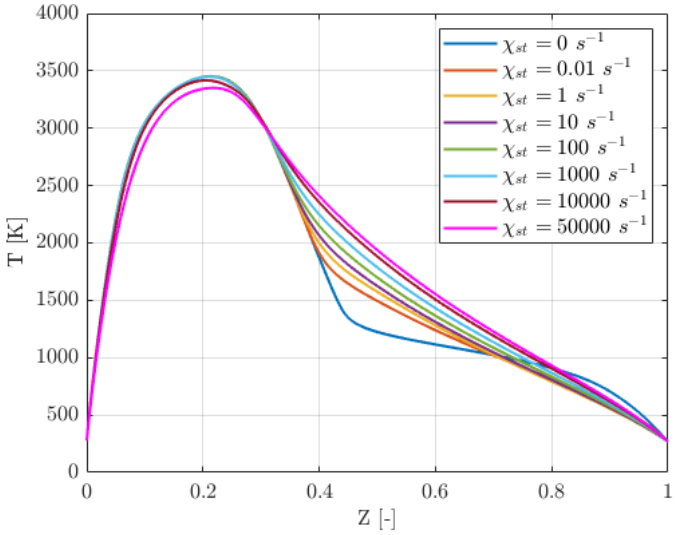


**Figure 2.2:** Effect of variable stoichiometric scalar dissipation on temperature ($\phi = 0$ kJ/kg).

These flamelet solutions are obtained by means of the OpenSMOKE++ library developed by the CRECK modeling group [23] which has been recently adapted to deal with flows under operating conditions that are of relevance for liquid rocket engines [37, 38, 62]. The employed chemical mechanism is the GRI 3.0 featuring 53 species and 325 reactions together with the provided

thermo-transport data [110]. Although being developed for standard pressure conditions, such mechanism has been successfully employed in many studies of high pressure, rocket-like, methane oxy-combustion cases [49, 55, 59, 62].

### 2.1.3 Extension to compressible flows

When the low-Mach number hypothesis is adopted, the tabulated properties are calculated at a given value of the thermodynamic pressure $p_0$, this hypothesis can be dropped introducing an additional quantity among the parameters of the libraries, representing the effect of pressure [39]. Such a quantity is the pressure ratio $\Lambda_p$ defined as:

$$\Lambda_p = \frac{p - p_{\min}}{p_{\max} - p_{\min}} \tag{2.9}$$

where $p$ is the pressure and $p_{\max}$, $p_{\min}$ are respectively the maximum and minimum value of the pressure expected in the field. Laminar flamelets are thus generated similarly to what described before, but for different values of $\Lambda_p$, $\phi$ and $\chi_s t$, the generic, laminar thermochemical property $\psi$ is now expressed as:

$$\psi = \psi(Z; \chi_{st}, \phi, \Lambda_p). \tag{2.10}$$

Also in the case of $\Lambda_p$, a delta-Dirac distribution of the presumed PDF is used to account for the effect of turbulence. Figure 2.3 reports the effect of the variable pressure on the equilibrium temperature profile, it is shown that temperature increases for increasing values of the normalized pressure ratio $\Lambda_p$.

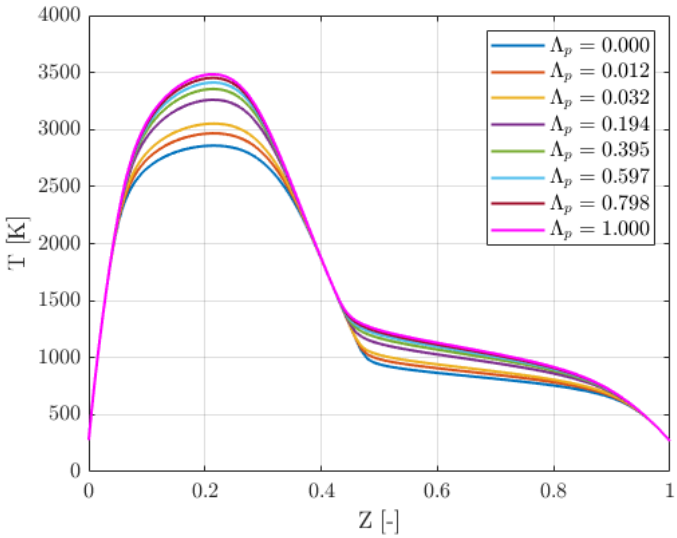


**Figure 2.3:** Effect of variable pressure on the equilibrium temperature ($\chi_{st} = 0\ s^{-1}$, $\phi = 0$ kJ/kg).

### 2.1.4 Application to non-reacting flows

The tabulated chemistry approach can be also applied to the single-species cases defining the conserved scalar as a non-dimensional temperature:

$$Z = \frac{T - T_{min}}{T_{max} - T_{min}} \tag{2.11}$$

An equivalent definition can be easily introduced in terms of enthalpy.

## 2.2 Wall modeling

Wall functions are introduced as stiffness-reduction technique for turbulent boundary layer modeling. They generally bridge the near-wall region with the fully turbulent flow by prescribing algebraic boundary conditions for mean turbulent quantities based on flow quantities far from the wall [14, 27]. The enforcement of wall functions lightens the grid requirements, since the last computational node before the wall should fall within the outer layer of a turbulent boundary layer, in order to patch the outer flow solution with the universal velocity and temperature profiles [46, 65, 117].

The variety of thermal wall functions can be divided into three main categories on the basis of the modeling complexity. Those categories are briefly listed below, and investigated in detail by Indelicato et al. in [37]. The intermediate formulation, that will be used throughout this thesis, will be then addressed in detail in the following Subsection.

- **Reynolds analogy**
  The first group of wall functions is based on the assumption of the similarity between the thermal and the kinematic boundary layer [12] and of constant properties across the boundary layer. The thermal diffusivity at the wall is obtained scaling the wall turbulent viscosity with a prescribed value of the turbulent Prandtl number.

- **Analytical wall models**
  The second class of wall functions introduces the variability of density and viscosity across the boundary layer, as a consequence of strong temperature gradients. They are based on the analytical determination of wall heat flux and turbulent thermal diffusivity stemming from the integration of the energy transport equation [3, 33, 99, 125].

- **Wall-coupled models**
  The most complex class of wall functions accounts for the mutual interaction between velocity and temperature near the wall due to chemistry and compressible effects, and derives from a DNS analysis of a turbulent reactive channel flow [14].

### 2.2.1 Han and Reitz formulation

The thermal wall function that will be employed in this work derives from the original formulation of Han and Reitz [33] and has been recently adapted for the operating conditions of Liquid Rocket Engines by Indelicato et al. [37].

Some simplifying hypotheses are adopted, among these: the gradients parallel to the wall are negligible with respect to the normal gradients, pressure is assumed as a sole function of time (i.e. negligible pressure gradients), no Dufour or Soret effects nor radiation phenomena are considered, the ideal gas model is assumed and the heat capacity $c_p$ is constant across the boundary layer. Under these hypotheses and under the assumption of frozen chemistry, the modeled heat flux at the wall reads:

$$q_w = \frac{\rho c_p u_\tau T \ln(T/T_w)}{2.1 \ln(y^+) + 2.5} \tag{2.12}$$

From the modeled wall heat flux, a turbulent thermal diffusivity $\alpha_{t,w}$ can be defined from the Fourier's expression of the heat flux at wall as:

$$\alpha_{t,w} = \frac{q_w}{c_{p,w} \frac{\partial \tilde{T}}{\partial y}} - \overline{\alpha}_w \tag{2.13}$$

For the complete derivation of the model the reader is referred to [37].

## 2.3 Coupling conditions for multi-region solvers

One of the key aspects of multi-region solvers for the thermal characterization is the boundary condition chosen to model the heat transfer across the interface. As already mentioned in the introduction, a first classification of the solution methods can be made based on the interface condition.

- **Direct coupling**
  The class of directly coupled methods entails the simultaneous solution of fluid and solid domains, coupled at the interface through a Conjugate Heat Transfer (CHT) condition, enforcing temperature and heat flux continuity. Due to its significant computational cost, this method is mainly devoted to steady-state operations [98].

- **Loose coupling**
  Loose coupling methods are instead based on the thermal chaining technique, i.e. the alternate solution of single domains, either fluid or solid, with the subsequent imposition of the solution of one domain as boundary condition for the other. These methods require the assumption of a first guess initial condition, but guarantee a lower computational effort and are therefore more commonly applied to more complex configurations. These methods can be furtherly classified on the basis of the quantity chosen as boundary condition: temperature, heat flux [72, 83, 111], or heat transfer coefficient [11].

### 2.3.1 Conjugate Heat Transfer condition

The Conjugate Heat Transfer (CHT) condition, characterizing the directly coupled methods, prescribes the continuity of temperature and heat flux across the interface:

$$\begin{cases} T_{\mathrm{F,int}} = T_{\mathrm{S,int}} = T_{\mathrm{int}} \\ q_{\mathrm{F}}\big|_{\mathrm{int},n=0^+} = \lambda_{\mathrm{F}} \frac{\partial T_{\mathrm{F}}}{\partial n}\Big|_{\mathrm{int},n=0^+} = \lambda_{\mathrm{S}} \frac{\partial T_{\mathrm{S}}}{\partial n}\Big|_{\mathrm{int},n=0^-} = q_{\mathrm{S}}\big|_{\mathrm{int},n=0^-} \end{cases} \tag{2.14}$$

where the subscripts $F$, $S$ and $int$ respectively stand for fluid, solid and interface, $n$ is the local coordinate normal to the interface, $q$ is the heat flux and $\lambda$ is the thermal conductivity of the considered continua.
The finite difference form of Eq. 2.14 reads:

$$\begin{cases} T_{\mathrm{F,int}} = T_{\mathrm{S,int}} = T_{\mathrm{int}} \\ \lambda_F \frac{T_F - T_{\mathrm{int}}}{\Delta_F} = \lambda_S \frac{T_{\mathrm{int}} - T_S}{\Delta_S} \end{cases} \tag{2.15}$$

with $\Delta$ the distance between the interface patch and the nearest cell center, and results in a constraint for the unknown interface temperature $T_{\mathrm{int}}$. A schematic view of the interface is given in Fig. 2.4 to ease the discussion.

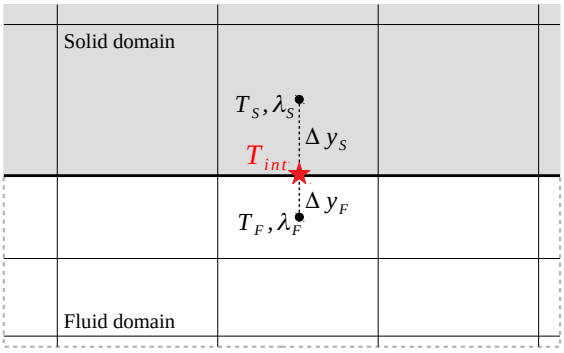


**Figure 2.4:** Schematic view of the interface between a generic solid (gray) and fluid domain (white).

The CHT boundary condition has to be adapted to the non-adiabatic flamelet-based combustion model and to a consistent use of the thermal wall function. The conductivity $\lambda_{\mathrm{F}}$ is taken from the flamelet libraries as a function of the conserved scalar $Z$, requiring in its turn the knowledge of $T_{\mathrm{int}}$. An iterative solution is therefore needed in proximity of the interface patches, where the temperature value varies at each iteration. Such a procedure depends on the kind of flow under analysis.

### Single-species flows

For single-species, non-reacting flows $Z$ is, as said, a non-dimensional temperature. The interface temperature $T_{\mathrm{int}}$ is therefore straightforwardly non-dimensionalized into the corresponding interface value of $Z_{\mathrm{int}}$, which is then used to access the libraries and retain the updated value of the conductivity $\lambda_{\mathrm{F}} = \lambda_{\mathrm{F}}(Z)$.

### Multi-species flows

For multi-species, reacting flows, the thermo-chemical quantities such as the conductivity $\lambda_{\mathrm{F}} = \lambda_{\mathrm{F}}(Z, \phi_H)$ are stored as functions of the mixture fraction and the enthalpy defect, the latter directly depending on $T_{\mathrm{int}}$. An iterative procedure is therefore performed defining a first guess of the enthalpy defect $\phi'_{\mathrm{H}}$ to access the tables and read $\lambda'_{\mathrm{F}} = \lambda'_{\mathrm{F}}(Z, \phi'_{\mathrm{H}})$. The latter is fed into Eq. 2.15 to obtain

the interface temperature $T'_{\text{int}}$, which in turn is used to determine an updated $\phi''_H$, i.e. the enthalpy defect corresponding to $T'_{\text{int}}$ for the given $Z_{\text{int}}$. The procedure is iterated until convergence.

**Turbulent flows**

In a turbulent, wall-modeled setting $\lambda_{\text{F}}$ is substituted by the effective conductivity $\lambda_{\text{F}_{\text{Eff}}}$, i.e. the sum of the laminar and turbulent contributions, being the first one directly read from the flamelet libraries, and the latter determined by the thermal wall-function [33, 37]. In particular, the laminar value is recovered from the tables as previously explained, while the turbulent one is calculated from the thermal wall function as $\lambda_t = c_p * \alpha_{t,w}$ being $\alpha_{t,w}$ the turbulent thermal diffusivity at the wall calculated as shown in Subsec. 2.2.1. In this way, the conductivity $\lambda_{\text{F}_{\text{Eff}}}$ retains within the CHT interface condition the information on the wall treatment.

### 2.3.2 Newton condition

Among the possible boundary condition usually employed in the context of the thermally chained simulation the Newton condition will be here considered. Within this work it will be used to model a fluid-to-solid interface, and consists in a continuity equation for temperature and heat flux conceptually equivalent to Eq. 2.14 and 2.15.

$$\begin{cases} T_{\text{F,int}} = T_{\text{S,int}} = T_{\text{int}} \\ q_{\text{F}}\big|_{\text{int},n=0^+} = h_C\left(T_{\text{ad}} - T_{\text{int}}\right) = \lambda_{\text{S}} \frac{\partial T_{\text{S}}}{\partial n}\Big|_{\text{int},n=0^-} = q_{\text{S}}\big|_{\text{int},n=0^-} \end{cases} \tag{2.16}$$

with the heat transfer coefficient $h_C$ defined as follows:

$$h_C = \frac{q}{T_{\text{ad}} - T_{\text{w}}} \tag{2.17}$$

For this condition, the contribution of the fluid-side is expressed in terms of heat transfer coefficient $h_C$ and adiabatic temperature $T_{\text{ad}}$, two reference quantities that can be considered constant in time, and does not require therefore the instantaneous solution of the fluid-dynamic flow, allowing to proceed n faster time-scales with the solution of the solid conduction problem.

## 2.4 Mixed coupling strategy

The enforcement of the CHT condition implies the coupling of the involved time scales, and requires a time-step dependent on the slowest process, resulting in a strong coupling and a computational cost of the coupled simulation proportional to the overall stiffness of the considered problem. The severity of this problem grows with the complexity of the fluid-dynamic field, becoming of particular concern when turbulent mixing and combustion are considered. Moreover, for several applications it is not possible to define a thermal steady-state, and hence it is not even possible to initialize the numerical simulation in a near-equilibrium configuration to speed up the convergence.
An alternative coupling strategy suitable for convection-dominated phenomena, i.e. cases where the fluid-to-solid convective heating is the prevailing process over solid-to-fluid heat conduction,

is presented in this Section. The objective of the approach is to further reduce the overall cost of the transient simulation so as to simulate the entire experiment time, without additional thermal modeling assumptions. The idea consists in a thermally chained approach initialized with a directly coupled simulation: the CHT condition Eq. 2.15 is enforced until the fluid-dynamic field reaches a statistical steady state. At this point the solid-to-fluid cooling effect is considered negligible, and the solution of the chemically reactive flow is replaced by a Newton condition enforced on the interface patch. The heat transfer coefficient $h_C$ used in Eq. 2.16 and defined in Eq. 4.1 is determined from a calculation which takes advantage of both the fully coupled CHT simulation (providing heat flux $q$ and interface temperature $T_{\text{int}}$) and of a simulation of the same configuration bounded with adiabatic wall conditions ($T_{\text{ad}}$). This change in the interface condition allows therefore to interrupt the fluid solution and continue the time-resolved simulation only in the solid domain, with a faster time scale depending on the heat conduction problem, the coupling strategy is briefly outlined in Fig. 2.5.

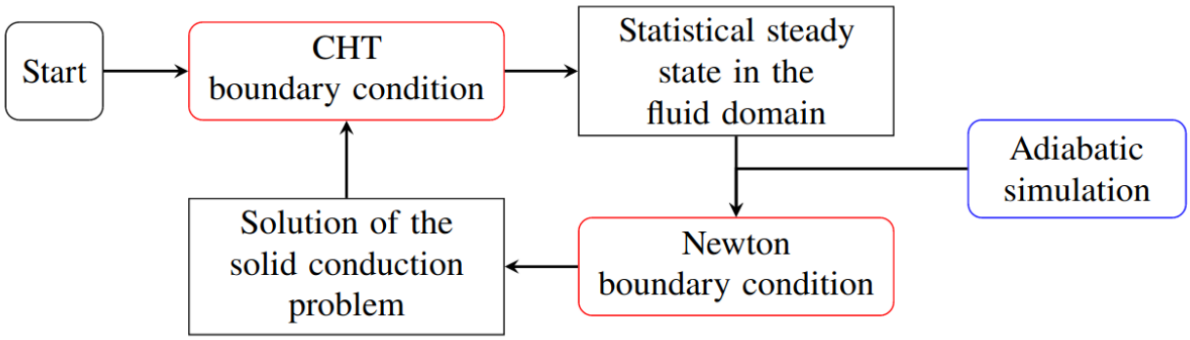


**Figure 2.5:** Flowchart of the coupling strategy.

Compared to the standard thermally chained approaches, the proposed methodology does not rely on any tentative initial temperature or heat flux value, as it is initialized with a CHT solution. As a result it does not need any iterative procedure to guarantee the solution convergence and it can be used on complex configurations which are concurrently characterized by different levels of the heat fluxes and thermal conditions of the solid regions. It is possible, for instance, to apply this mixed coupling strategy only on specific patches of the solid domain, while maintaining the standard fully coupled interface modeling on the others.

### 2.4.1 Choice of the Newton condition among others

The Newton condition has been chosen among the number of conditions generally employed in the thermally chained simulations due to its weak dependence on the unknown $T_{\text{int}}$, as also suggested by Betti et al. [11]. This condition allows in fact to maintain the time-dependence in the calculation of the interface temperature, allowing to properly describe transient phenomena. The validity of the condition, as well as the soundness of the hypothesis of constant $h_C$ will be extensively addressed in the results section, specifically in Chap. 5.
Figure 2.6 shows the interface temperatures obtained on the lateral wall of a combustion chamber for several time instants, according to several methods: fully coupled interface (CHT condition), enforcement of a constant heat transfer coefficient $h_C$ (Newton condition) and enforcement of a

constant heat flux $q$. It is shown that, although initially the three condition are in good agreement, when approaching to solid-conduction time scales the enforcement of a constant $q$ leads to an over-estimation of the interface temperature, since it neglects by definition the time variation of interface temperature value and the subsequent variation of transmitted heat flux, that decreases on account of the reduced difference between the flow and the interface temperatures. The Newton condition, instead, does not rely on any assumption on the interface temperature, providing therefore a more truthful solution.

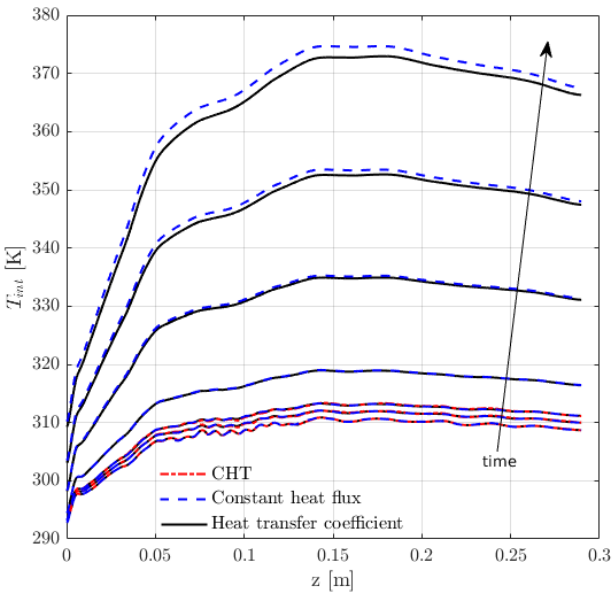


**Figure 2.6:** Comparison between different loose coupling methods and direct solution. The direct coupling condition (CHT, dashed red line) is compared to the main loose coupling approaches: enforcement of a constant heat flux (dashed blue) and enforcement of a constant heat transfer coefficient (solid black).

### 2.4.2 Time-step management in the mixed coupling strategy

When considering a multi-domain problem consisting in a turbulent reacting flow coupled with a solid conduction problem, the slowest and therefore driving process is obviously the fluid-dynamic problem, characterized by a time-scale that can be more than two orders of magnitude smaller than the time-scale in the solid conduction problem. The mixed coupling strategy is specifically introduced to ease the computational effort needed by these configuration, allowing to take the fluid flow solution out of the equation when the Newton condition is prescribed, and proceed on the time scale required by the less demanding solid conduction problem. This also allows to use a less stringent solver tolerance, speeding up furthermore the solution convergence.

In order to implement the mixed coupling strategy, it is necessary to define the time intervals after which move from one boundary condition to the other, namely the respective duration of the CHT-bounded and Newton-bounded simulations. The statistical steady-state of the fluid domain is obtained after a multiple of the so-called flow-through time:

$$t_F = \frac{L}{U} \tag{2.18}$$

with $U$ the fluid particle velocity and $L$ the test-case characteristic dimension.

The definition of the corresponding time for the solid conduction problem is not as straightforward, and is obtained from the solution of the eigenvalue problem associated to the solid conduction equation, extracting at last the slowest timescale. In this case, the solid width normal to the interface surface is taken as characteristic direction of the domain $L_S$, and the general heat equation can be written as follows:

$$\frac{\partial T}{\partial t} = \frac{\lambda}{\rho c_p}\frac{\partial^2 T}{\partial x^2} \tag{2.19}$$

with $x \in [0, L_S]$ and

$$\text{B.C.} \begin{cases} -\lambda \frac{\partial T}{\partial x}\big|_{x=0} = h_C(T_{\text{ad}} - T_{\text{w}_0}) \\ -\lambda \frac{\partial T}{\partial x}\big|_{x=L_S} = h_{C_{\text{L}_S}}(T_{\text{ext}} - T_{\text{w}_{\text{L}_S}}) \end{cases} \tag{2.20}$$

where for the sake of generality the equation has been considered bounded by two Newton conditions, representative on one side $(x = 0)$ of the heat exchange e.g. with a fluid, and on the other $(x = L_S)$ of the heat lost for natural convection with the external ambient

The solution of the eigenproblem associated to Eq. 2.19 depends on the solid characteristics, as width, conductivity, density and heat capacity, and on the Biot number at the interface, a non-dimensional number defined as in Eq. 2.21 representative of the ratio between the outwards convective heat transfer and the heat conduction within the solid (cfr. Fig 2.7).

$$Bi = \frac{h_C L}{\lambda} \tag{2.21}$$

In the case of a capacitively cooled rocked combustion chamber, it is possible to resort to the simplifying hypothesis of negligible heat transfer with the external air compared to the heat exchanged at the hot gas side interface, the characteristic solid time step obtained in this case is:

$$t_S = \left[\frac{\lambda_S}{\rho_S c_{p_S} L_S^2}\frac{\pi^2}{4}\left(2 + \frac{1}{\text{Bi}_\text{F} + 1}\right)^2\right]^{-1} \tag{2.22}$$

With $Bi_F$ the Biot number calculated at the fluid-to-solid interface and $L_S$ is the solid width.

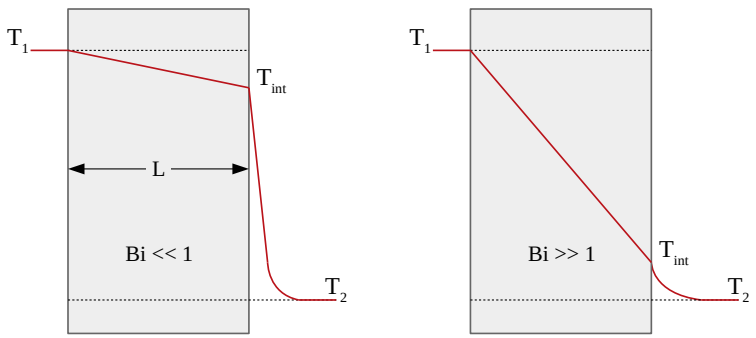


**Figure 2.7:** Comparison of fully developed temperature profiles in two plates with different Biot numbers.

# Chapter 3

# Numerical framework

## Contents



## Nomenclature

**Latin letters**

| | |
|---|---|
| $c_p$ | = Specific heat at constant pressure |
| $C_d$ | = Model constant |
| $C_g$ | = Model constant |
| $C_\mu$ | = Model constant |
| $C_\chi$ | = Model constant |
| $d$ | = Distance between neighbouring nodes |
| $h$ | = Mixture enthalpy |
| $k$ | = Turbulent kinetic energy |
| $p$ | = Pressure |
| $t$ | = Time |
| $u$ | = Velocity |
| $x_i$ | = Cartesian coordinate |
| $Z$ | = Mixture fraction |

**Greek letters**

| | |
|---|---|
| $\alpha$ | = Thermal diffusivity |
| $\delta_{i,j}$ | = Kroenecker delta |
| $\epsilon$ | = Turbulent dissipation rate |
| $\rho$ | = Density |
| $\mu$ | = Viscosity |
| $\nu_t$ | = Turbulent viscosity |
| $\tau_t$ | = Turbulent time scale |
| $\chi$ | = Scalar dissipation rate |
| $\psi$ | = Generic scalar property |

In this Chapter the numerical implementation of the framework is given. First the complete set of equations employed will be summarized for each category of settings analyzed, i.e. low-Mach

and pressure-dependent equations for reacting flows, as well as the equation for the solid domains in the case of multi-region solvers. All the solvers employed throughout the thesis are developed in the context of the OpenFOAM and OpenSMOKE++ [23] frameworks, which are open-source, object-oriented C++ platforms for the integration of Partial Differential Equations (PDEs) based on the finite volume approach. Some remarks on such an approach are then given, together with a description of the segregated strategy adopted for the time and space integration. An analysis of the time-step management in multi-physics and multi-domain solvers is finally given.

## 3.1 Governing equations

In this section are reported the governing equations for mass, momentum, energy and conserved scalar for a reactive mixture under low-Mach number hypothesis and their extension to compressible flows, followed by the thermal Fourier equation solved within the solid domains. In the following sections and chapters, the Unsteady Reynolds Averaged Navier-Stokes approach is selected when dealing with fluid domains for its superior capabilities, compared to steady RANS, to better characterize the turbulent non-premixed flames resolving at least the main macroscopic reacting flow features of injection problems, while maintaining a reasonable computational cost [62, 68].

### 3.1.1 Low-Mach number flows

The continuity, momentum and energy equations under the low-Mach number hypothesis read:

$$\frac{\partial \bar{\rho}}{\partial t} + \frac{\partial (\bar{\rho}\widetilde{u_i})}{\partial x_i} = 0 \tag{3.1}$$

$$\frac{\partial (\bar{\rho}\widetilde{u_i})}{\partial t} + \frac{\partial (\bar{\rho}\widetilde{u_i}\widetilde{u_j})}{\partial x_j} = -\frac{\partial \bar{p}}{\partial x_i} + \frac{\partial}{\partial x_j}\left[(\bar{\mu} + \bar{\rho}\nu_t)\left(\frac{\partial \widetilde{u_i}}{\partial x_j} + \frac{\partial \widetilde{u_j}}{\partial x_i} - \frac{2}{3}\delta_{ij}\frac{\partial \widetilde{u_l}}{\partial x_l}\right)\right] \tag{3.2}$$

$$\frac{\partial (\bar{\rho}\widetilde{h})}{\partial t} + \frac{\partial (\bar{\rho}\widetilde{u_i}\widetilde{h})}{\partial x_i} = \frac{\partial}{\partial x_i}\left[\left(\bar{\alpha} + \frac{\bar{\rho}\nu_t}{\mathrm{Sc}_t}\right)\frac{\partial \widetilde{h}}{\partial x_i}\right] \tag{3.3}$$

with $\bar{\cdot}$ and $\widetilde{\cdot}$ the already mentioned symbols of Reynolds and Favre averages, $u_i$ the $i-$th component of the velocity along Cartesian coordinate $x_i$ ($i = 1, 2, 3$), $\mu$ the mixture viscosity and $\delta_{ij}$ is the Kronecker delta $\alpha$ the laminar thermal diffusivity, $Sc_t$ a turbulent Schmidt number set to $0.85$ and $\nu_t$ the turbulent viscosity. The energy equation 3.3 is solved in terms of mean enthalpy of the mixture, while the continuity equation 3.1 is substituted, in the context of a pressure-based solver, by the following pressure equation that guarantees the mass conservation:

$$\frac{\partial \bar{\rho}}{\partial t} + \frac{\partial \left(\bar{\rho} A_D^{-1} H\right)}{\partial x_i} - \frac{\partial}{\partial x_i}\left(\bar{\rho} A_D^{-1}\frac{\partial p}{\partial x_i}\right) = 0 \tag{3.4}$$

where $A_D$ and $H$ the coefficient matrices coming from the discretized version of the momentum equation in a finite volume context (cfr. [26] and Sec. 3.4.1).

The set of equations is completed by the transport equation for the mixture fraction $Z$ and its variance $Z''^2$:

$$\frac{\partial(\bar{\rho}\widetilde{Z})}{\partial t}+\frac{\partial(\bar{\rho}\widetilde{u_i}\widetilde{Z})}{\partial x_i}=\frac{\partial}{\partial x_i}\left[\left(\bar{\alpha}+\frac{\bar{\rho}\nu_t}{Sc_t}\right)\frac{\partial\widetilde{Z}}{\partial x_i}\right] \tag{3.5}$$

$$\frac{\partial(\bar{\rho}\widetilde{Z''^2})}{\partial t}+\frac{\partial(\bar{\rho}\widetilde{u_i}\widetilde{Z''^2})}{\partial x_i}=\frac{\partial}{\partial x_i}\left[\left(\bar{\alpha}+\frac{\bar{\rho}\nu_t}{Sc_t}\right)\frac{\partial\widetilde{Z''^2}}{\partial x_i}\right]+C_g\left(\bar{\alpha}+\frac{\bar{\rho}\nu_t}{Sc_t}\right)\left|\frac{\partial\widetilde{Z}}{\partial x_i}\right|^2-C_d\bar{\rho}\frac{\epsilon}{k}\cdot\widetilde{Z''^2} \tag{3.6}$$

where $C_d$ and $C_g$ are model constants respectively set to $2.00$ and $2.86$.

In this case and in the following, the standard $k-\epsilon$ model [121] is used to calculate $k$ and $\epsilon$ representing respectively the turbulent kinetic energy and its dissipation rate. Following the uRANS formulation, the turbulent viscosity $\nu_t$ is then evaluated as:

$$\nu_t=C_\mu\frac{k^2}{\epsilon} \tag{3.7}$$

with $C_\mu=0.09$. On the other hand the stoichiometric scalar dissipation rate is proportional to the mixture fraction variance $\widetilde{Z''^2}$ according to the following algebraic relation [94]:

$$\widetilde{\chi}_{st}=C_\chi\frac{\epsilon}{k}\widetilde{Z''^2} \tag{3.8}$$

with $C_\chi=2.00$ as a model constant and $\tau_t=k/\epsilon$ representing a characteristic turbulent time scale.

### 3.1.2 Extension to the pressure parametrization

When the low-Mach number hypothesis is dropped and pressure-dependent effects are considered, additional terms have to be accounted in the energy equation 3.3, which now reads:

$$\frac{\partial(\bar{\rho}\widetilde{h})}{\partial t}+\frac{\partial(\bar{\rho}\widetilde{u_i}\widetilde{h})}{\partial x_i}=\frac{\partial}{\partial x_i}\left[\left(\bar{\alpha}+\frac{\bar{\rho}\nu_t}{\mathrm{Sc}_t}\right)\frac{\partial\widetilde{h}}{\partial x_i}\right]+\frac{\partial p}{\partial t}+\widetilde{u_i}\frac{\partial p}{\partial x_i} \tag{3.9}$$

The pressure-terms inside the energy equation are responsible for the variation of the static enthalpy, as for example happens inside the nozzle due to the supersonic expansion of the flow.

### 3.1.3 Solid conduction problem

The solid conduction problem is tackled with the thermal Fourier equation for the enthalpy balance:

$$\frac{\partial(\rho h)}{\partial t}=\frac{\partial}{\partial x_j}\left(\alpha\frac{\partial h}{\partial x_j}\right) \tag{3.10}$$

where the thermal diffusivity $\alpha$ can be accommodated to account for either homogeneous, porous or anisotropic continua by means of specific correction factors. The thermophysical model associated to the solid domain calculates therefore the temperature based on the solved enthalpy field and the specific heat capacity $c_p$ defined as an input.

## 3.2 Finite Volume approach

OpenFOAM relies on the Finite Volume Method (FVM) [26], a space discretization technique which first divides the computational domain non-overlapping Control Volumes (CVs) and then solves for the central node of each control volume the discretized equations. The characteristic of the CVs of being non-overlapping ensures that each face bounding the CV is shared with only one neighbouring cell. Each cell is labeled, $P$ will be used in the following to identify the central node of the CV in which the solution is sought. It follows that:

$$\int_{\mathrm{CV}} (x - x_P) dV = 0 \tag{3.11}$$

$$\int_{\mathrm{S}} (x - x_P) dS = 0 \tag{3.12}$$

Considering a the standard form of the transport equation for a general scalar property $\psi$:

$$\frac{\partial \rho\psi}{\partial t} + \nabla \cdot (\rho \mathbf{u}\psi) - \nabla(\rho\Gamma_\psi \nabla\psi) = \Omega_\psi \tag{3.13}$$

it is possible to derive how each term is discretized both in time and space, with an accuracy level at least equal to the order of the original equation [41], in this case second-order, as Eq. 3.13 includes the second derivative of $\psi$ in space in the diffusion term. For a second-order accurate method, the variation of the object function $\psi(\mathbf{x}, t)$ must be linear both in time and space:

$$\psi(\mathbf{x}) = \psi(\mathbf{x}_P) + (\mathbf{x} - \mathbf{x}_P)(\nabla\psi)_P \tag{3.14}$$

$$\psi(t + \Delta t) = \psi(t) + \Delta t \left(\frac{\partial \psi}{\partial t}\right)_t \tag{3.15}$$

According to the Finite Volume approach, Eq. 3.13 has to be verified over the control volume around the centroid $P$ in its integral form:

$$\int_t^{t+\Delta t} \left[ \frac{\partial}{\partial t} \int_{CV} \rho\psi dV + \int_{CV} \nabla \cdot (\rho \mathbf{u}\psi) dV - \int_{CV} \nabla(\rho\Gamma_\psi \nabla\psi) dV \right] dt = \int_t^{t+\Delta t} \int_{CV} \Omega_\psi dV dt \tag{3.16}$$

The discretization of each term will be discussed in the following subsections [36, 41].

### 3.2.1 Spatial discretization

Considering Eq. 3.14 and 3.11, and adopting for the sake of brevity the notation:

$$\psi_P = \psi(\mathbf{x}_P) \tag{3.17}$$

the general integral over the control volume reads:

$$\begin{aligned}\int_{CV}\psi dV &= \int_{cv}[\psi_P + (\mathbf{x}-\mathbf{x}_P)(\nabla\psi)_P]dV \\ &= \psi_P\int_{CV}dV + (\nabla\psi)_P\int_{CV}(\mathbf{x}-\mathbf{x}_P)dV \\ &= \psi_P V_P\end{aligned} \tag{3.18}$$

Invoking the Gauss' theorem, the linear expansion in Eq. 3.14 and Eq. 3.12 it is possible to derive an equivalent expression for the surface integrals:

$$\begin{aligned}\int_{CV}\nabla\cdot\psi &= \int_S \psi ds \\ &= \sum_k\left(\int_{S_k}\psi ds\right) \\ &= \sum_k \psi_k\int_{S_k}ds + \sum_k(\nabla\psi)_k\int_{S_k}(\mathbf{x}-\mathbf{x}_k)ds \\ &= \sum_k S_k\psi_k\end{aligned} \tag{3.19}$$

where the surface integral has been decomposed in the sum of the integral over each Control Volume's edge $\int_S \mathbf{a}ds = \sum_k\left(\int_{S_k}\mathbf{a}ds\right)$, $\psi_k$ indicates the value of $\psi$ in the $k$-th face central node and $S_k$ is the outward-pointing face area vector. Since the CVs are defined by construction with outward-pointing normals, the face area vector points outwards from $P$ only if the $k$-th face belongs to the CV centered in $P$.

The two identities just derived are used to discretize each term of the general transport equation in the integral form (cfr. Eq. 3.16), as reported in the following. Note that in this section only the spatial discretization is tackled.

**Convection term**

Making reference to Eq. 3.19:

$$\begin{aligned}\int_{CV}\nabla\cdot(\rho\mathbf{u}\psi)dV &= \sum_k S_k(\rho\mathbf{u}\psi)_k \\ &= \sum_k S_k(\rho\mathbf{u})_k\psi_k \\ &= \sum_k F\psi_k\end{aligned} \tag{3.20}$$

where the mass flux through the $k$-th face has been defined as $F = S_k(\rho\mathbf{u})_k$. Each quantity on the $k$-th node (in this case $(\rho\mathbf{u})_k$ and $\psi_k$) is obtained by linear interpolation from the centroid node $P$ and the considered surface [26].

**Diffusion term**

Making again reference to Eq. 3.19:

$$\begin{aligned}\int_{CV} \nabla(\rho\Gamma_\psi \nabla\psi) dV &= \sum_k S_k (\rho\Gamma_\psi \nabla\psi)_k \\ &= \sum_k S_k (\rho\Gamma_\psi)_k (\nabla\psi)_k\end{aligned} \tag{3.21}$$

where the term $(\nabla\psi)_k$ can be written in a finite difference form considering two consecutive nodes in the case of orthogonal meshes. In the common case of non-orthogonal meshes, i.e. grids where the $S_k$ normal is not aligned with the distance between two neighbour nodes, an additive correction factor must me introduced:

$$S_k(\nabla\psi)_k = v(\nabla\psi)_k + n(\nabla\psi)_k \tag{3.22}$$

with $v$ and $h$ the components of $S_k$ in a frame of reference aligned with the distance between neighbouring nodes.

**Source term**

The source term $\Omega_\psi$ can be a general function of $\psi$, therefore no general discretization procedure can be outlined. This term collects all the terms of Eq. 3.16 that cannot be written as convection, diffusion or temporal terms.

### 3.2.2 Temporal discretization

The temporal discretization is based on the assumption that the CV does not change in time. The general transport equation in integral form Eq. 3.16 can be rewritten under this assumption, and introducing the space-discretized terms (Eq. 3.20 and 3.21) in the so-called "semi-discretized" form:

$$\int_t^{t+\Delta t} \left[ \left( \frac{\partial}{\partial t} \rho\psi \right)_P V_P + \sum_k F\psi_k - \sum_k S_k (\rho\Gamma_\psi)_k (\nabla\psi)_k \right] dt = \int_t^{t+\Delta t} \Omega_\psi V_P dt \tag{3.23}$$

The time derivative can be calculated in a finite difference form between the $n$-th and the $(n+1)$-th instant as:

$$\left( \frac{\partial \rho\psi}{\partial t} \right)_P = \frac{(\rho\psi)_P{}^{n+1} - (\rho\psi)_P{}^n}{\Delta t} \tag{3.24}$$

while the time integral can be calculated resorting to Eq. 3.15 as:

$$\int_t^{t+\Delta t} \psi(t) dt = \frac{1}{2}(\psi^{n-1} + \psi^n)\Delta t \tag{3.25}$$

Substituting in Eq. 3.23 the final second order accurate discretized equation is obtained, according to the Crank-Nicholon method:

$$\begin{aligned}\frac{(\rho\psi)_P{}^{n+1} - (\rho\psi)_P{}^{n}}{\Delta t}V_P + \sum_k F\psi_k^{n+1}\Delta t - \sum_k S_k(\rho\Gamma_\psi)_k(\nabla\psi)_k^{n+1}\Delta t + \\ + \sum_k F\psi_k^{n}\Delta t - \sum_k S_k(\rho\Gamma_\psi)_k(\nabla\psi)_k^{n}\Delta t = \\ = \Omega_\psi V_P\end{aligned} \tag{3.26}$$

The discretized equation is second-order accurate in time, and requires the knowledge of the values $\psi$ and $\nabla\psi$ in both the current time instant and the previous one. The face values are calculated interpolating from the cells centroids values as mentioned in the previous sections.

Regrouping all the coefficients multiplying $\psi_P$ and $\psi_k$ it is possible to obtain an algebraic equation for the generic quantity $\psi_P$ valid for each CV:

$$a_P\psi_P^n + \sum_k a_{k,P}\psi_k^n = \Omega_\psi \tag{3.27}$$

with $k$ spanning over all the faces shared between the CV and neighbouring cells. For a numerical grid with $N$ Control Volumes the previous equation is inserted in a system of equation in the matricial form:

$$[A]_{\mathrm{NxN}}[U]_{\mathrm{Nx1}} = [B]_{\mathrm{Nx1}} \tag{3.28}$$

where $[A]$ is a sparse matrix, with coefficients $a_P$ on the diagonal and $a_{k,P}$ off the diagonal, non-zero if the considered face is shared between an owner and a neighbour cell, $[U]$ is the vector of the generic variable $\psi$ for each CV and $[B]$ is the vector of the source terms [36, 41].

It is common to neglect the variation of the face values of $\psi$ and $\nabla\psi$ in time in order to obtain a discretized transport equation which is only first-order accurate and combines the old and new time-level convection, diffusion and source terms, leaving the temporal derivative unchanged:

$$\frac{(\rho\psi)_P{}^{n+1} - (\rho\psi)_P{}^{n}}{\Delta t}V_P + \sum_k F\psi_k\Delta t - \sum_k S_k(\rho\Gamma_\psi)_k(\nabla\psi)_k\Delta t = \Omega_\psi V_P \tag{3.29}$$

In this case, $\psi_k$ and $(\nabla\psi)_k$ can be evaluated according to several methods, briefly discussed in the following.

**Explicit discretization**

The face values of $\psi$ and $\nabla\psi$ are determined from the previous time instant, here denoted with $n$ in contrast with the current instant $n+1$, as well as the linear part of the source term.

$$\psi_k = f_x\psi_P^n + (1 - f_x)\psi_P^n \tag{3.30}$$

$$(\nabla\psi)_k = \Delta\frac{\psi_N^n - \psi_P^n}{d} \tag{3.31}$$

with $N$ denoting the neighbour cell to the considered CV and $d$ the distance between the neighbouring nodes, under the hypothesis of orthogonal mesh. According to this method, all the terms

of Eq. 3.29 depend only on the previous instant, and therefore there is no need of solving the system of equation.

**Euler Implicit method**

The face values are in this case expressed in terms of the new time instant $n+1$:

$$\psi_k = f_x \psi_P^{n+1} + (1 - f_x)\psi_P^{n+1} \tag{3.32}$$

$$(\nabla\psi)_k = \Delta \frac{\psi_N^{n+1} - \psi_P^{n+1}}{d} \tag{3.33}$$

Although being still a first-order accurate method, this approach foresees the solution of a system of equation similar to Eq. 3.27, guaranteeing an higher numerical stability with respect to the explicit discretization.

**Backward differencing in time**

This temporal scheme is second-order accurate in time but still neglects the temporal variation of the face values. Each term of the original Eq. 3.16 is initially discretized to the second-order accuracy leading to Eq. 3.26, then the temporal derivative is obtained considering the Taylor series expansion of $\psi$ in time around $\psi(t + \Delta t) = \psi^{n+1}$ and truncating it after the first order with a truncation error that scales with $\Delta t$.

$$\begin{aligned} \psi(t) = \psi^n &= \psi^{n+1} - \frac{\partial\psi}{\partial t}\Delta t + \frac{1}{2}\frac{\partial^2\psi}{\partial t^2}\Delta t^2 + = (\Delta t^3) = \\ &\approx \psi^{n+1} \end{aligned} \tag{3.34}$$

$$\begin{aligned} \frac{\partial\psi}{\partial t} &= \frac{\psi^{n+1} - \psi^n}{\Delta t} + \frac{1}{2}\frac{\partial^2\psi}{\partial t^2}\Delta t + O(\Delta t^2) \\ &\approx \frac{\psi^{n+1} - \psi^n}{\Delta t} \end{aligned} \tag{3.35}$$

Since the temporal derivative is discretized up to second order, the whole discretization of the transport equation will be second-order accurate even if the temporal variation of $\psi$ and $\nabla\psi$ is neglected. This methods requires the knowledge of a third time instant $n-1$, and produces a system of algebraic equations that must be solved for $\psi_P^{n+1}$.

## 3.3 Courant number limit

Time and space discretizations are usually not independent, but are linked by the Courant-Friedrichs-Lewy condition [20], a constraint of the maximum value that the Courant number $Co$ must assume in order to ensure the convergence of the numerical scheme.

$$\mathrm{Co} = \frac{u_k^n \Delta t}{d} \leq \mathrm{Co}_{\max} \tag{3.36}$$

$\mathrm{Co}_{\max}$ can be different for different numerical schemes, in general the following condition is imposed:

$$\Delta t^n = \mathrm{Co}_{\mathrm{sel}} \min\left(\frac{d}{u_k^n}\right) \tag{3.37}$$

with $\mathrm{Co}_{\mathrm{sel}}$ the selected Courant number lower than the maximum value $\mathrm{Co}_{\max}$. It follows that to fine meshes with CV nodes close to each other (i.e. small $d$) or fluid-dynamic flows with high velocity fields (i.e. large $u_k$) correspond a small time-integration step $\Delta t$ and a subsequent high computational cost.

### 3.3.1 The case of multi-domain coupled configurations

A crucial aspect for coupled solvers is the interplay between time scales of different physical phenomena. In the case of solid conduction problems a Diffusion number $Di$ can be defined, providing a measure of the rate at which information is transported:

$$Di = \frac{\lambda}{C_p \rho} \frac{\Delta_t}{\Delta x^2} = \alpha \frac{\Delta_t}{\Delta x^2} \tag{3.38}$$

with $\alpha$ the thermal diffusivity and $\Delta t$, $\Delta x$ respectively the time and space discretization steps.

Similarly to what seen with the Courant number, a maximum admissible value of $Di$ can be imposed, resulting in an operative limiting factor for the performance of the numerical schemes employed.

$$\Delta t = \mathrm{Di}_{\mathrm{sel}} \min\left(\frac{\Delta x^2}{\alpha}\right) \tag{3.39}$$

with $\mathrm{Di}_{\mathrm{sel}}$ the selected Diffusion number lower than the maximum value $\mathrm{Di}_{\max}$.

When a multi-domain and multi-physics simulation is performed, a time step is calculated for each domain in order to meet the Courant or Diffusion number limit. For coupled simulations, the minimum among the time steps calculated for all the coupled domains is selected and used for the time-integration.

## 3.4 Segregated approach for single-region solvers

The OpenFOAM implementation is based on a segregated approach, i.e. the sequential solution of the Eq. 3.1-3.6. The main categories of codes for the solution of the system of equation can be divided in:

- **Density-based codes**: where the mass conservation equation is used to calculate the density and the Equation of State (EoS) is used to calculate the pressure,
- **Pressure-based codes**: where the equations are reformulated in terms of momentum and pressure equations.

In both cases the velocity is derived starting from the momentum conservation equation. In this Section the second approach will be discussed, together with the main pressure-based algorithms usually found in CFD codes, the Semi-Implicit Method for Pressure Linked Equations (SIMPLE) and the Pressure Implicit with Splitting of Operator (PISO), and their combination, the PIMPLE algorithm.

### 3.4.1 Derivation of the Pressure Equation

The bottom line of the pressure-based solvers is the solution of a pressure equation that guarantees the mass conservation (Eq. 3.4). This is derived from the Navier-Stokes system, here in a simplified form under the hypothesis of incompressible flow [36, 41]. Using the notation seen in Eq. 3.28, the semi-discretized form of the momentum equation at the generic $m$-th iteration and for the $i$-th velocity component reads:

$$[A]^{m-1}_{\mathrm{NxN}}[U]^{m}_{i,\mathrm{Nx1}} = [Q]^{m-1}_{i,\mathrm{Nx1}} - [G]_{i,\mathrm{Nx1}}(p^m) \tag{3.40}$$

with $[A]$ the matrix of linearized coefficients, $[Q]$ the vector of the source terms and $[G]$ the gradient operator. The coefficient matrix $[A]$ can be split in its diagonal (D) and non-diagonal (ND) contributions in order to highligth the contributions of the CVs and of the neighbouring cells. Neglecting the source terms for the sake of simplicity it is obtained:

$$[A_{\mathrm{D}} + A_{\mathrm{ND}}][U]^{m}_{i} = -[G]_i(p^m) \tag{3.41}$$

A predicted value of the velocity $[U]^{*}_{i}$ can be calculated using the pressure value from the previous iteration $m-1$ by enforcing the momentum equation:

$$[A_{\mathrm{D}} + A_{\mathrm{ND}}]^{m-1}[U]^{*}_{i} = -[G]_i(p^{m-1}) \tag{3.42}$$

This velocity does not satisfies in principle the continuity constraint, thus it is necessary to introduce a velocity correction term $U^{'}$ such that the corrected velocity verifies the following definition and constraint:

$$\begin{cases} U^{**} = U^{*} + U^{'} \\ \nabla \cdot (\rho U^{**}) = 0 \end{cases} \tag{3.43}$$

This is achieved searching a pressure correction term $p^{'}$ for pressure:

$$p^{*} = p^{m-1} + p^{'} \tag{3.44}$$

that introduces a correction on both pressure and velocity:

$$[A_{\mathrm{D}} + A_{\mathrm{ND}}][U]^{**}_{i} = -[G]_i(p^{*}) \tag{3.45}$$

By substituting the definitions of $U^{**}$ and $p^{*}$ and developing all the terms, the equation becomes:

$$[A_{\mathrm{D}} + A_{\mathrm{ND}}][U]^{*}_{i} + [A_{\mathrm{D}} + A_{\mathrm{ND}}][U]^{'}_{i} = -[G]_i(p^{m-1}) - [G]_i(p^{'}) \tag{3.46}$$

which can be simplified taking into account the expression of the predicted velocity Eq. 3.42, leading to a relation between the pressure and the velocity correction:

$$[A_{\mathrm{D}} + A_{\mathrm{ND}}][U]^{'}_{i} = -[G]_i(p^{'}) \tag{3.47}$$

In a first approximation, it is possible to assume the velocity correction equal to zero in the neigh-

bour cells, i.e. $[A_{\mathrm{ND}}][U_i^{'}] = 0$, obtaining a simplified expression for the velocity correction:

$$[U]_i^{'} = -[A_{\mathrm{D}}]^{-1}[G]_i(p^{'}) \tag{3.48}$$

where the notation $[\cdot]^{-1}$ indicates the inverse of the matrix. It is now possible to substitute the velocity correction $[U]_i^{'}$ in the continuity constraint Eq. 3.43 and considering the definition of the corrected velocity $[U]^{**}$, it is finally possible to obtain an equation for the unknown pressure correction $p^{'}$, based on the velocity velocity value predicted with the pressure at the previous iteration:

$$\nabla(\rho U_i^*) - \nabla\left(\rho[A_{\mathrm{D}}]^{-1}[G]_i(p^{'})\right) = 0 \tag{3.49}$$

In order to get to the pressure equation form implemented in OpenFOAM for pressure-based solvers (cfr. Eq. 3.4), it is necessary to solve for the corrected pressure $p^*$ rather than for the correction term $p^{'}$. It is possible to obtain a definition of the predicted velocity $U^*$ from Eq. 3.42:

$$[U]_i^* = -[A_{\mathrm{D}}]^{-1}[G]_i(p^{m-1}) + [A_{\mathrm{D}}]^{-1}[H] \tag{3.50}$$

with $[H]$ the explicit part of the derivative operator containing explicit contributions from the convective term and the generic source terms initially assumed to be negligible.

$$[H] = [A_{\mathrm{D}}][U]_i - [A][U]_i \tag{3.51}$$

being $[H]$ depending on the velocity field, its implementation depends on the specific algorithm selected for the solution, as will be shown in the following.

The predicted velocity expression in Eq. 3.50 can be substituted in Eq. 3.49 to obtain a pressure equation depending on the pressure at the previous time instant $m-1$ and on the pressure correction $p^{'}$.

$$-\nabla\left(\rho[A_{\mathrm{D}}]^{-1}[G]_i(p^{m-1})\right) + \nabla\left(\rho[A_{\mathrm{D}}]^{-1}[H]\right) - \nabla\left(\rho[A_{\mathrm{D}}]^{-1}[G]_i(p^{'})\right) = 0 \tag{3.52}$$

By recalling the definition of the corrected velocity $p^*$ Eq. 3.44 it is finally possible to obtain a pressure equation equivalent to Eq. 3.4:

$$\nabla\left(\rho[A_{\mathrm{D}}]^{-1}[G]_i(p^*)\right) - \nabla\left(\rho[A_{\mathrm{D}}]^{-1}[H]\right) = 0 \tag{3.53}$$

The presence of the matrix $[H]$ as a source term of the pressure equation, causes a coupling between the pressure and velocity fields. In the following a brief outline of how the main solution algorithms deal with this coupling will be given.

#### PISO Algorithm

The Pressure Implicit with Splitting of Operator has been originally proposed by Issa [40] and can be summarized into three main steps:

1. **Momentum predictor**: the momentum equation is solved using the pressure value from the previous time step to obtain a prediction of the velocity.

2. **Pressure solution**: the pressure equation is solved to obtain the first estimate of the new pressure field.

3. **Explicit velocity correction**: the velocity field is corrected as a consequence of the updated pressure field.

The explicit correction of the velocity neglects the contribution of the neighbour velocities, therefore an iterative procedure is needed. According to the PISO algorithm, the matrix $[H]$ is corrected with the updated velocity and the loop is restarted from step 2.

**SIMPLE Algorithm**

The Semi-Implicit Method for Pressure Linked Equations is suited for steady-state problems as originally proposed by Patankar [82].

1. An approximation of the velocity field is obtained by solving the momentum equation with the pressure field from the previous time instant. The equation is implicitly under-relaxed with a velocity under-relaxation factor.

2. The pressure equation is solved to obtain the new pressure field.

3. The new conservative fluxes are calculated on the basis of the new pressure field.

The entire process is iterated from step 1, as a consequence $[H]$ is updated at the beginning of each iteration with the velocity from the previous one.

**PIMPLE Algorithm**

The algorithm used in the present thesis work is the PIMPLE algorithm, which operatively is a merging between the two methods introduced above. In PIMPLE loops intermediate steps are considered, the notation $\psi^{m,a}$ will e used to denote the generic property $\psi$ at the sub-step $a$ (with $a \in [0, N_a]$) between the steps $m$ and $m+1$. With this notation it is possible to consider nested loops.

1. The momentum equation is solved using the pressure value from the previous time step $p^{m,a-1}$ to obtain the velocity $U^{m,a}$. For steady state problem the under-relaxation factor is used as in the SIMPLE algorithm.

2. The transport equations for mixture fraction, mixture fraction variance and any other scalars are solved using $p^{m,a-1}$ and $U^{m,a}$

3. The thermodynamic quantities are extracted from the libraries

4. The discretization matrices and correction factor and calculated

5. The corrected pressure $p^{m,a}$ is calculated

6. The turbulent quantities are updated.

The implementation of the PIMPLE algorithm in OpenFOAM is schematized in Alg. 1, where the two nested loops of which the method is composed are highlighted: the overall "outer" loop, and the "inner" loop, retracing the PISO structure and consisting of the steps 4 and 5 of the list above.

**Algorithm 1** Single-region solver

```
1: for nOuterCorr do                                   ▷ Pimple loop
2:     UEqn.H
3:     ZEqn.H
4:     HEqn.H
5:     Update thermodynamic quantities
6:     for nInnerCorr do                               ▷ Piso loop
7:         pEqn.H
8:     end for
9: end for
```

## 3.5 Segregated approach for multi-region solvers

In multi-region solvers specific sections of the code are activated depending on whether the domain under analysis is fluid or solid. Alg. 2 outlines the structure of a multi-region solver amenable for an arbitrary number of solid and fluid domains. Since the Fourier thermal equation Eq. 3.10 does not require iterative correction, the solution of the solid conduction problem is inserted in the segregated strategy within the "outer" loop after the solution of the solid domain. The domains are coupled by an explicit call to the interface condition (lines 7 and 14 in Alg. 2) which uses the temperature and conductivity values in one domain to calculate the balance equation Eq. 2.15 with the other domain. The time-step between two consecutive iterations of the outer loop is discussed in Sec. 3.3.1.

**Algorithm 2** Multi-region solver

```
1: for nOuterCorr do                                   ▷ Pimple loop
2:     for Fluid domain do
3:         UEqn.H
4:         ZEqn.H
5:         HEqn.H
6:         Update thermodynamic quantities
7:         Update CHT boundary condition
8:         for nInnerCorr do                           ▷ Piso loop
9:             pEqn.H
10:        end for
11:    end for
12:    for Solid domain do
13:        Energy equation                             ▷ ∂(ρh)/∂t = ∂/∂x_j (α ∂h/∂x_j)
14:        Update CHT boundary condition
15:    end for
16: end for
```

# Chapter 4

# Single-region analysis of the thermal load in the injection region

## Contents



## Nomenclature

**Latin letters**

| | |
|---|---|
| $C$ | = Nominal confinement length |
| $h_C$ | = Heat transfer coefficient |
| $L_C$ | = Confinement length |
| $k$ | = Turbulent kinetic energy |
| $O/F$ | = Oxidizer-to-fuel ratio |
| $p$ | = Pressure |
| $p_0$ | = Outlet pressure |
| $q$ | = Heat flux |
| $R$ | = Combustion chamber radius |
| $T$ | = Temperature |
| $U$ | = Velocity |
| $u_\tau$ | = Skin friction velocity |
| $x$ | = Radial coordinate |
| $y^+$ | = Wall unit |
| $z$ | = Longitudinal coordinate |
| $Z$ | = Mixture fraction |

**Operators**

| | |
|---|---|
| $\langle\cdot\rangle$ | = Surface average |

**Subscripts and superscripts**

| | |
|---|---|
| $\square_{\mathrm{ad}}$ | = Adiabatic value |
| $\square_{\mathrm{exp}}$ | = Experimental value |
| $\square_{\mathrm{F}}$ | = Fuel value |
| $\square_W$ | = Wall value |

In this Chapter the thermal characterization of a realistic combustor in LRE-like operative condition is performed in a single-region setting. The combustion chamber analyzed is the TUMrig experimental combustor developed at the Technical University of Munich (TUM) [15] and used

as a reference testcase by a number of groups in the rocket community [37, 54, 72, 81, 83, 103, 129], consisting in a square-section chamber equipped with a single shear coaxial injector emanating a gaseous oxygen/gaseous methane (GOx/GCH4) turbulent, non-premixed flame. The analysis is performed resorting to a low-Mach number solver in a single-region setting, therefore neglecting the heat transfer within the surrounding solid walls and modeling it with a thermal boundary condition. In a first instance, a two-dimensional axis-symmetric approximation is used. In particular, two baseline configurations are defined in order to model different situations encountered within an hypothetical multi-injector plate: a wall-bounded configuration is chosen to investigate the injector-wall interaction, while a symmetric condition is used to mimic the mutual interaction between injectors located in the inner part of the injection plate. For each of these configurations, a first analysis is performed with fixed geometry and varying boundary conditions in order to assess the effect of the thermal modeling on the flow-field. Secondly, the lateral dimension of the chamber, namely the confinement, is parametrically varied in a range of interest to investigate the effect of the injectors placement and mutual distance on the ensuing thermal load. A data-driven model for the thermal characterization of multi-injector chambers is finally proposed, on the basis of the collected database.

## 4.1 Introduction to the test case

The experimental TUMrig combustor is adopted as baseline case, consisting in a 12x12 mm square-section capacitively cooled combustion chamber equipped with a single shear coaxial GOx/GCH4 injector. The injection conditions employed in the present work are taken from the reference work by Celano et al. [15], corresponding to the nominal operating point at a chamber pressure of $20$ bar and $O/F = 2.6$ with an oxidizer mass flow rate of $0.0045$ kg/s and a fuel mass flow rate of $0.0017$ kg/s. A two-dimensional axis-symmetric approximation is used, the numerical domain considered is therefore a wedge of an equivalent cylindrical combustion chamber, with a chamber radius defined to guarantee the same mass-flux as the reference square-section experimental chamber as commonly done for RANS and uRANS [16]. Consistently with the low-Mach number formulation, the computational domain is truncated at the nozzle inlet where a uniform pressure is imposed, as shown in Fig. 4.1.

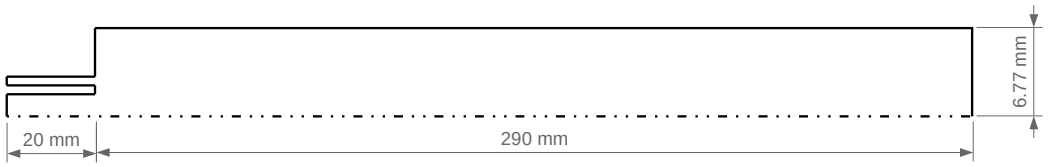


**Figure 4.1:** Geometry and configuration of the TUMrig 2D in a single-region setting and under the low-Mach number hypothesis.

As mentioned in the Chapter introduction, two configurations have been defined in order to simulate the different situations met within a generic multi-injector plate. With reference to Fig. 4.2, a wall-bounded configuration has been adopted to investigate the injector-wall interaction (upper sub-figure), while a symmetry boundary condition has been used to mimic the mutual interaction between injectors located in the inner part of the firing plate (lower sub-figure). For the sake

of clarity, the two representative configurations are drawn, in Fig. 4.2, on a hypothetical multi-dimensional problem with multiple injection elements (central sub-figure). The color-coded fields represent instantaneous temperature in the central sub-figure and time-averaged temperature in the upper and lower sub-figures.

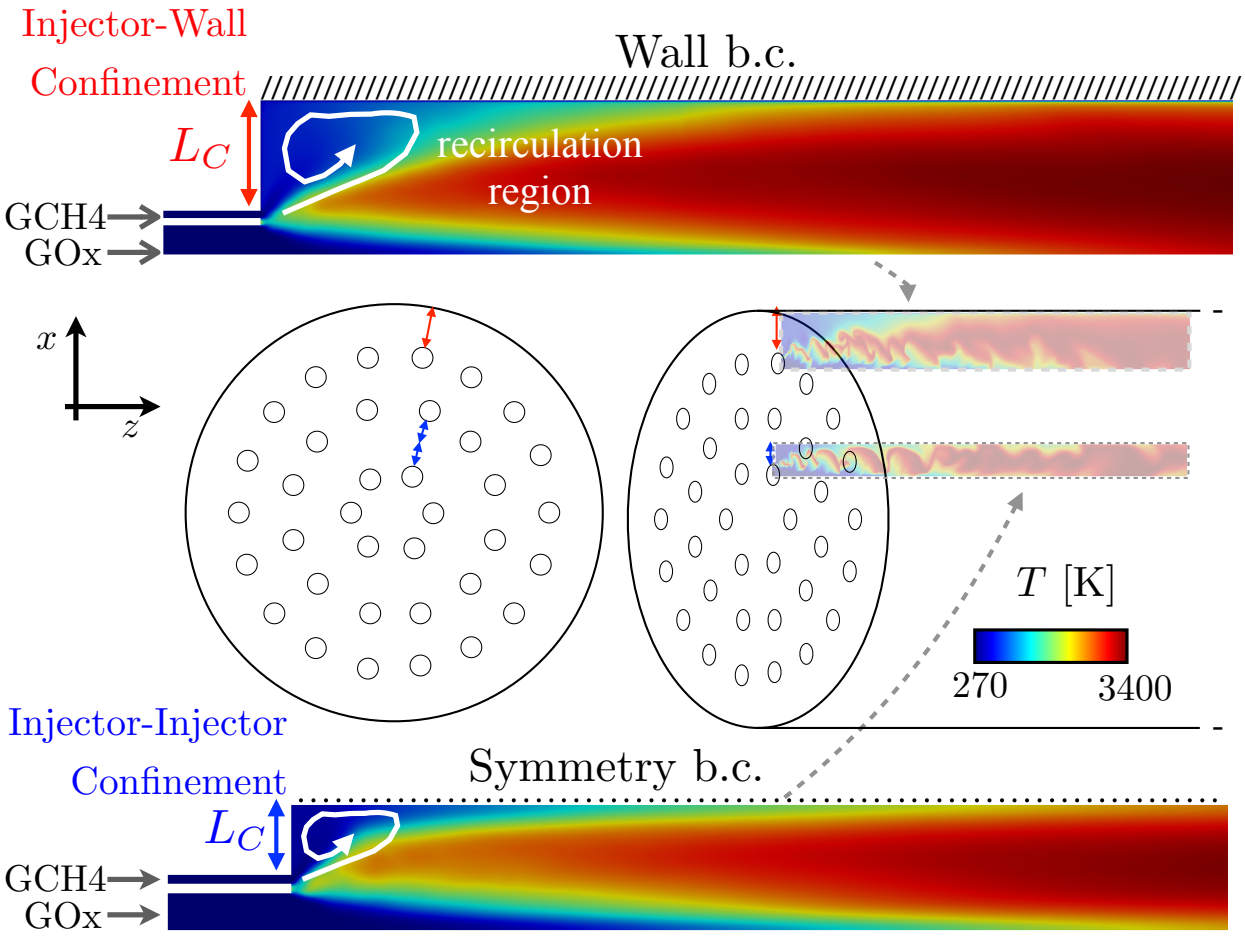


**Figure 4.2:** Schematic of the 2D axis-symmetric configurations studied: wall-bounded configuration representative of the injector-wall interaction and symmetric configuration representative of the injector-injector interaction.

### 4.1.1 Grid assessment study

A grid independence analysis is performed comparing the results of three different numerical grids, obtained by recursively doubling the number of computational points in each direction. Owing to the intrinsic differences of the two configurations, a specific numerical grid has been defined for each of the cases. Note that, in the following, experimental and literature results [15, 83] can be used as reference validation data only for the wall-bounded configuration. The meshes employed are named W-C, W-M, and W-F for the wall-bounded cases, and S-C, S-M and S-F for the symmetric ones, with the first letter referring to the bounding condition and the second letter standing respectively for Coarse, Medium and Fine, indicating increasing refinement levels. The main grid characteristics are given in Tab. 4.1.

| | Finite Volumes | | Finite Volumes |
|---|---|---|---|
| W-C | $6.8 \cdot 10^3$ | S-C | $7.8 \cdot 10^3$ |
| W-M | $27.5 \cdot 10^3$ | S-M | $31.5 \cdot 10^3$ |
| W-F | $109.7 \cdot 10^3$ | S-F | $125.6 \cdot 10^3$ |

**Table 4.1:** Numerical mesh characteristic for the grid convergence assessment.

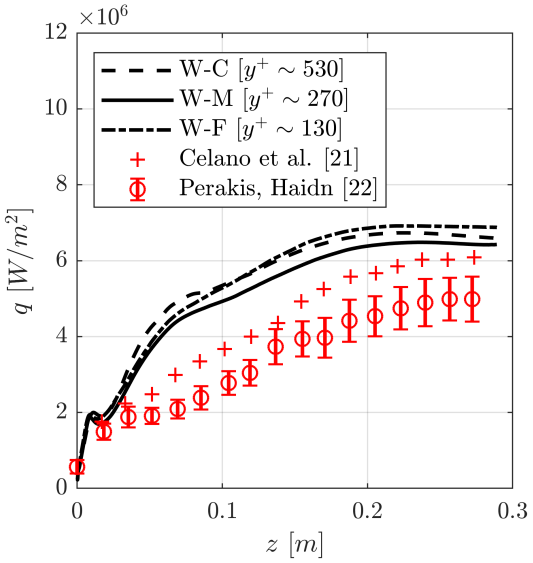


(**a**) Time-averaged wall heat flux on the chamber wall compared to experimental and literature data.

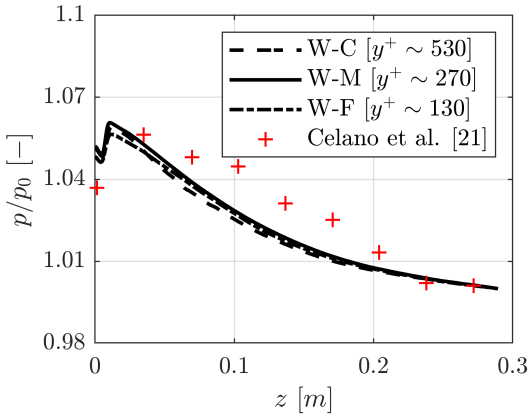


(**b**) Time-averaged normalized pressure on the chamber wall compared to experimental data.

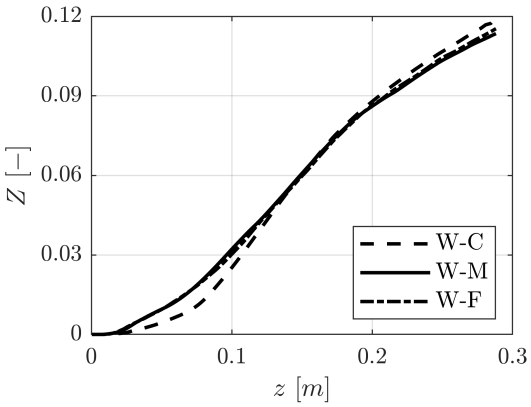


(**c**) Time-averaged mixture fraction on the chamber axis.

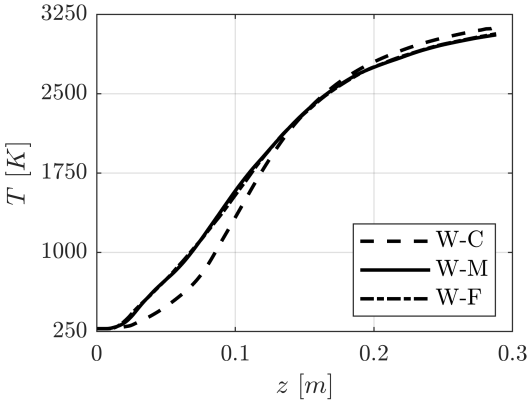


(**d**) Time-averaged temperature on the chamber axis.

**Figure 4.3:** Grid convergence assessment for the wall-bounded configuration.

Figures 4.3a and 4.3b report respectively the time-averaged heat flux and pressure normalized to the outlet value on the combustor lateral wall. The overall accordance with the experimental data is considered satisfactory in the limit of the two-dimensional approximation. The overestimation of the experimental results from $z > 0.04$ m on was already observed in [37] and is related to the wall function dependence on the turbulent wall-modeling of the skin friction velocity $u_\tau$. The results are observed to be satisfactorily independent from the numerical grid used, showing an offset between each grid result that is comparable to the experimental error reported.
Other quantities of interest (QoI) are presented in Fig. 4.3c and 4.3d, showing respectively the time-

averaged mixture fraction and temperature along the chamber axis, following a similar approach to Zips et al. in [128] for a similar unsteady setting.

The intermediate grid W-M is then chosen as the reference baseline mesh for the wall-bounded simulations, providing a satisfactory trade-off between accuracy and computational cost.

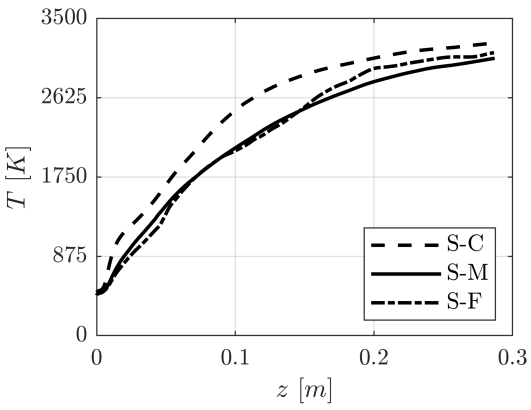


(**a**) Time-averaged temperature on the symmetry surface.

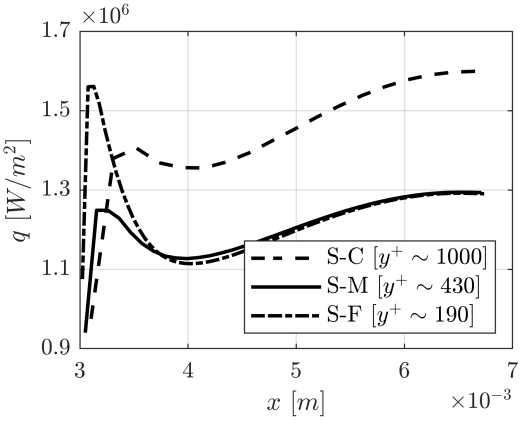


(**b**) Time-averaged wall heat flux on the injection plate.

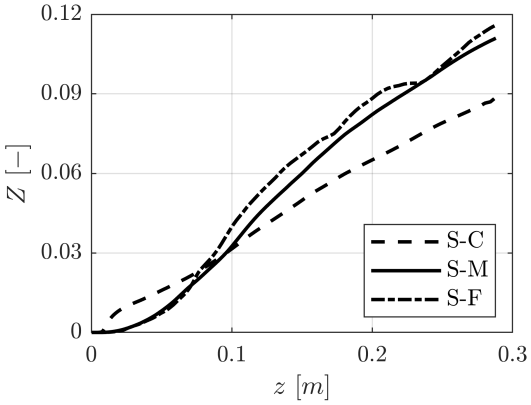


(**c**) Time-averaged mixture fraction on the chamber axis.

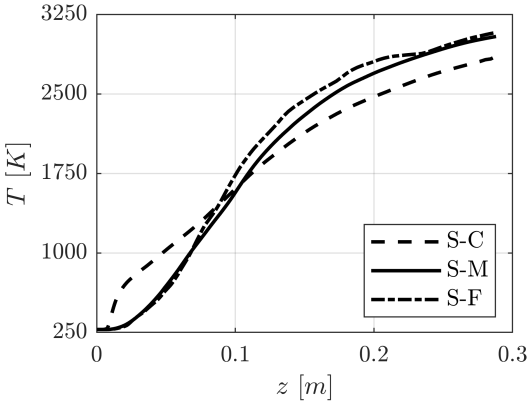


(**d**) Time-averaged temperature on the chamber axis.

**Figure 4.4:** Grid convergence assessment for the symmetric configuration.

For the symmetric configuration, Fig. 4.4a and 4.4b show respectively the temperature profile obtained along the symmetry surface and the heat flux obtained on the injection plate for the three numerical grids under analysis. Note that, differently from the results of the wall-bounded configuration shown in Fig. 4.3 where lateral wall heat flux exists, in this case only the wall heat flux along the injection plate can be considered. A good agreement between the solutions obtained with the medium and fine grids is observed. Figure 4.4b shows that the profiles obtained using the medium and the fine grids, S-M and S-F, are very close for $x > 4 \cdot 10^{-3}$ m, while the peak value located between $3 \cdot 10^{-3}$ m and $4 \cdot 10^{-3}$ m is poorly resolved with the medium grid. However, this does not affect significantly the surface-averaged value which will be of interest for the investigation of its trends with the injector lateral confinement. In fact, such surface-averaged values are respectively $1.22$ MW/m$^2$ using the S-M grid and $1.26$ MW/m$^2$ for the S-F, resulting in a discrepancy of less than $3.4\%$.

Following the same strategy of the wall-bounded case, in Fig. 4.4c-4.4d are shown, respectively, the mixture fraction and temperature along the chamber axis. All the results show a good agree-

ment between the intermediate and fine computational grids, indicating therefore that the intermediate mesh S-M can be chosen as the baseline grid for the symmetric configurations.

In order to complete this numerical grid analysis, the independence of the mean flame position from the resolution employed is also assessed. Figure 4.5 displays, for both the configurations, the stoichiometric mixture fraction isolines for each numerical grid considered. It can be observed that the average position of the flame inside the combustor is scarcely influenced by the resolution of the computational mesh.

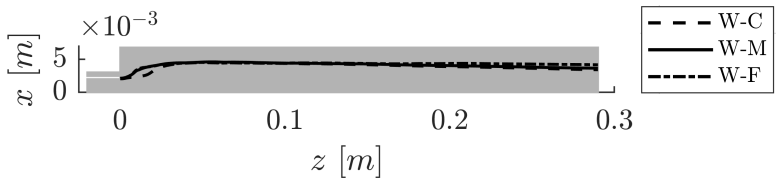


(**a**) Wall-bounded configuration.

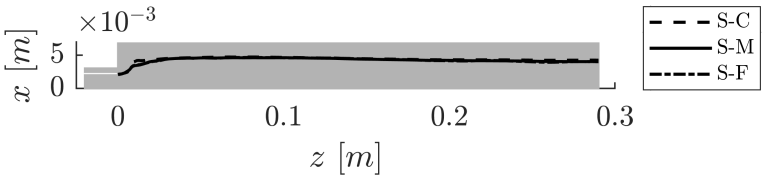


(**b**) Symmetry-bounded configuration.

**Figure 4.5:** Stoichiometric mixture fraction isoline $Z_{st} = 0.2$ obtained with different numerical grids. Axes not to scale.

## 4.2 Thermal modeling effect

In order to assess the effect of the thermal boundary condition on the flow fields in the two configurations, several combinations of boundary conditions have been tested, as reported in Tab. 4.2. In particular, on the injection plate and the lateral chamber wall, where present, all possible combinations of adiabatic and isothermal conditions have been simulated. In the case of isothermal lateral chamber wall, a temperature profile $T_{exp}$ has been imposed (linear from 320 K to 420 K), matching the experimental data from the thermocouples as reported in [15]. For the injection plate, on the other hand, there are no available data in the literature, due to the difficulty of accessing the wall with experimental thermocouples. For this reason, a fixed temperature value equal to the fuel inlet temperature $T_F = 269$ K has been used, representing the lowest possible fluid temperature to which the surface is subjected. This choice implies that the wall is always colder than the impinging reacting mixture, thus allowing the use of the non-adiabatic flamelet model without any further modification. Moreover, maximising the difference between the imposed temperature $T_F$ and the adiabatic wall temperature $T_{ad}$ will prevent approximation errors in the following calculation of the heat transfer coefficient.

With reference to the boundary conditions shown in Tab. 4.2, the effect of isothermal wall are

| Name | Injection plate b.c. | Imposed T | Chamber wall b.c. | Imposed T |
|---|---|---|---|---|
| W-AI | Adiabatic | - | Isothermal | $T_{exp}$ |
| W-AA | Adiabatic | - | Adiabatic | - |
| W-II | Isothermal | $T_F$ | Isothermal | $T_{exp}$ |
| W-IA | Isothermal | $T_F$ | Adiabatic | - |
| S-A | Adiabatic | - | Symmetry plane | - |
| S-I | Isothermal | $T_F$ | Symmetry plane | - |

**Table 4.2:** Thermal boundary conditions

analyzed in terms of the resulting wall heat flux while adiabatic and symmetric conditions in terms of the resulting boundary temperature. Results on the chamber wall are shown by assessing the effect of the injection plate boundary and vice versa.

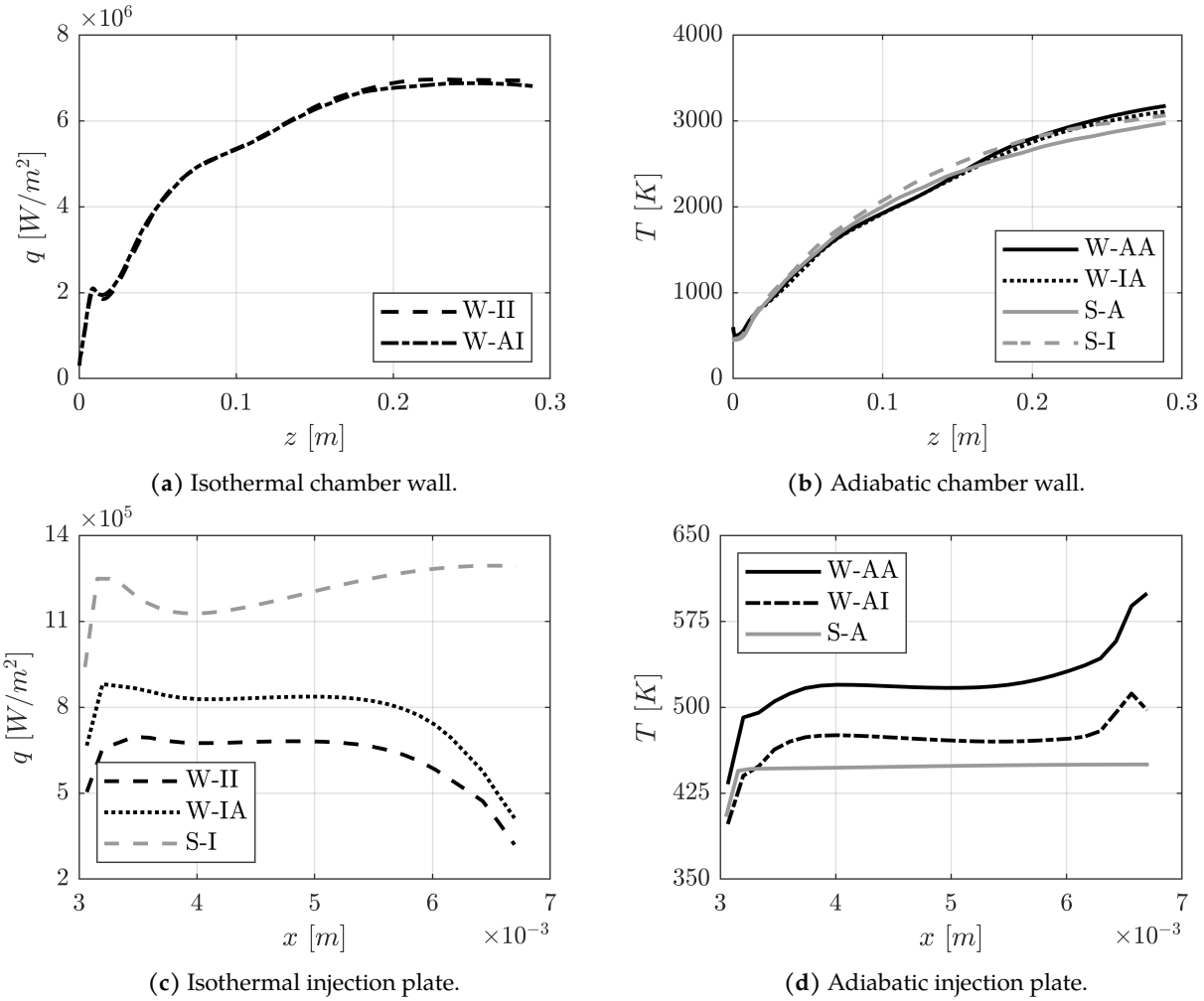


(**a**) Isothermal chamber wall.

(**b**) Adiabatic chamber wall.

(**c**) Isothermal injection plate.

(**d**) Adiabatic injection plate.

**Figure 4.6:** Boundary condition effect. Results are compared fixing a condition on one wall and varying the other. Both wall-bounded (black) and symmetric configurations (grey) are compared.

Figures 4.6a and 4.6b show, respectively, that the heat flux and temperature obtained on the combustion chamber lateral wall are almost unaffected by the condition used for the injection plate, suggesting that the injection plate modeling has its major effect on the recirculation region rather than on the fully developed flow. Figure 4.6c shows instead the difference between the heat flux on the injection plate obtained in the wall-bounded case and in the symmetric configuration. The

profiles shown for W-II and W-IA are characterized by a minimum of heat flux at the chamber corner ($x > 6 \cdot 10^{-3}$), where the flow presents a stagnation point. Conversely, the symmetric configuration S-I has a maximum at the same corner. Comparing the two wall-bounded cases, the effect of the lateral wall boundary condition is clearly visible: in the fully isothermal case W-II the fluid exchanges heat with the lateral wall before approaching the injection plate, producing on the latter a lower $q$ compared to the W-IA case. Figure 4.6d shows finally the temperature obtained on the adiabatic injection plate for different boundary conditions. The difference between the wall-bounded cases W-AA, W-AI and the symmetric case S-A is caused by the difference in the recirculating flow near the wall. Observing the wall-bounded results it is possible to see the limiting effect of the isothermal lateral wall, that causes a lower injection plate temperature compared to the W-AA case.

Configurations W-II and S-I are compared in Fig. 4.7 to give an overview on the effect of the bounding condition on the overall flow field. Time-averaged temperature, velocity magnitude and turbulent kinetic energy are displayed to represent the thermal, kinematic and turbulence fields. An isoline corresponding to the stoichiometric mixture fraction $Z = 0.2$ averaged over time is displayed in each plot, representing the location of the average flame. Both configurations are characterized by a recirculation region at the injection plate, this region has been highlighted for clarity in Fig. 4.2. The presence of the lateral isothermal wall induces a narrow colder layer in the near wall temperature field, and combined with the effect of the viscous wall causes a slight downward deflection of the flame towards the end of the combustion chamber for the wall-bounded case. The wall-bounded kinematic field is characterized by a more elongated recirculation bubble and a tighter opening angle of the flame, while the time-averaged kinetic energy field shows a higher turbulence level in the first section of the symmetric configuration, due to the mixing with the recirculation bubble of the neighbouring flame.

## 4.3 Assessment of the selected configurations

Although not being fully representative of the actual multi-injector configuration, the two single-injector, two-dimensional, axis-symmetric configurations selected allow for the simplest representation of the flame-wall and flame-flame interactions.

In order to assess the soundness of the two-dimensional approximation employed, a three-dimensional multi-injector combustion chamber has been simulated. The test-case, shown in Fig. 4.8, features 37 injector elements with the same dimensions as those used for the database collection, and a geometry of the firing plate characterized by a $15^\circ$ symmetry, as typically encountered in real firing plates [113, 115, 116]. Such a geometry is based on the layout of the 7-injectors subscale experimental combustor developed at the Technical University of Munich [109], with the addition of two more injectors rings. The latter have been added respecting the symmetry criteria and injectors' spacing of the original subscale combustor in order to be representative of real-existing multi-injector geometries. The injection conditions employed are retained from the single-injector test-case used as a reference for the database, and both the firing plate and lateral chamber wall have been considered isothermal, with temperature imposed equal to those indicated in Tab. 4.2. The numerical grid employed, featuring $\sim 10^6$ finite volumes, is truncated at the nozzle inlet consistently with the low-Mach number approximation used.

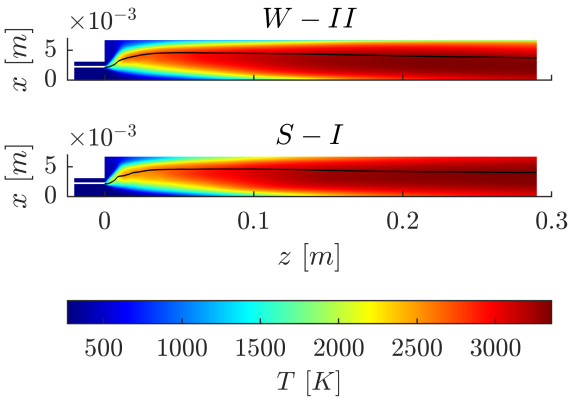


(**a**) Temperature

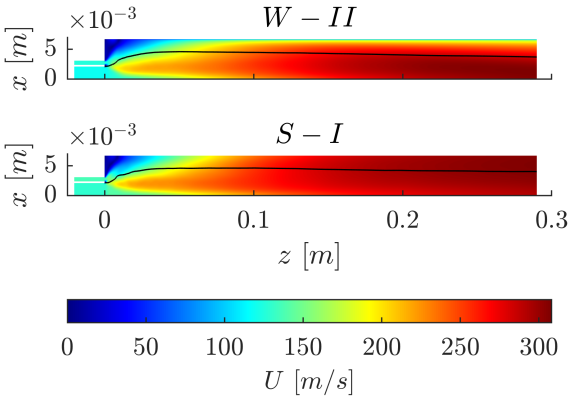


(**b**) Velocity magnitude

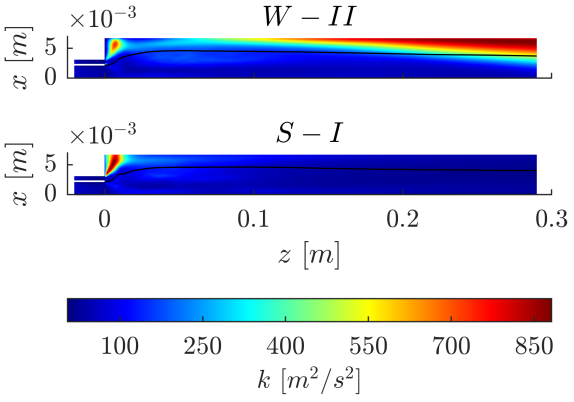


(**c**) Kinetic energy

**Figure 4.7:** Comparison between W-II and S-I time-averaged flow fields with superimposed mixture fraction isoline $Z_{st} = 0.2$. Axes not to scale.

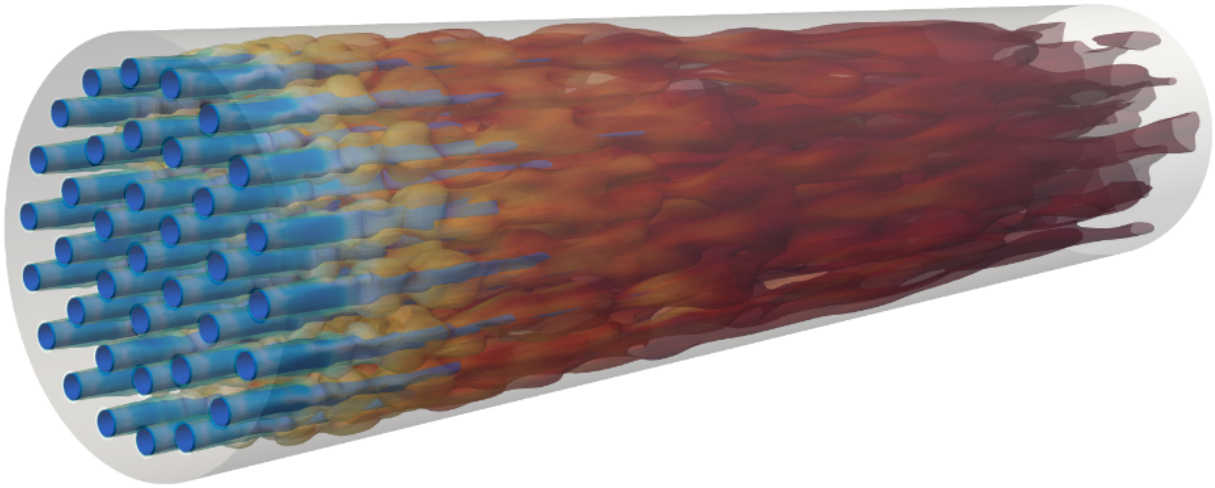

**Figure 4.8:** 3D simulation used as a test bench for the database.

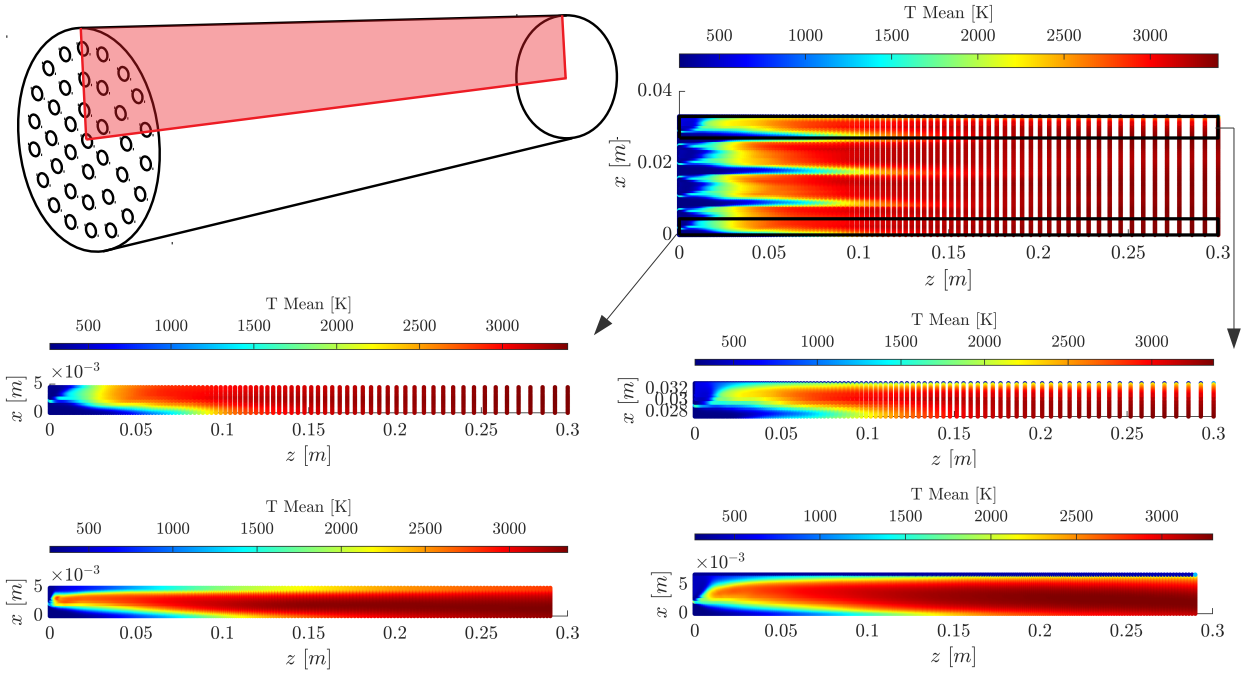


**Figure 4.9:** Comparison between 2D and 3D fields. Slice of the 3D field (upper panels) and comparison of 2D symmetric (left) and wall-bounded (right) fields to the corresponding section of the 3D simulation (lower panels).

Figure 4.9 shows a comparison between the two dimensional fields collected in the database and slices of the three-dimensional multi-injector simulation. The central injector of the three-dimensional configuration has been chosen as reference case for the two-dimensional symmetric injector. In a similar way, the external injector, nearest to the combustor chamber wall, has been compared with the two-dimensional wall-bounded case featuring the most similar confinement length. In both cases, the length of the central oxygen core is well captured, albeit the initial section of the flame is slightly colder in the three-dimensional field. The length of the recirculation region is quite well reproduced in the wall-bounded case, while the symmetric two-dimensional configuration shows a more confined flame with a longer recirculation. It must be noted, however,

that the refinement of the three-dimensional simulation is much smaller than what employed in the two-dimensional configurations, with a longitudinal resolution equal to half the resolution of the 2D cases.

## 4.4 Confinement effect

In order to investigate the confinement effects on the flame, flow field and on the ensuing thermal loads, the confinement length $L_C$ has been varied between $0.5$ and $2.5$ times its nominal value $C = 3.77 \cdot 10^{-3}$ m. The parametric analysis has been conducted for both the wall-bounded and symmetric configurations, and for each of them the fully-adiabatic and fully-isothermal sets of boundary conditions have been simulated, namely W-AA, S-A, W-II, S-I according to the nomenclature used in Tab. 4.2. Table 4.3 reports all the simulations performed, along with their label: the first letter refers to the configuration used, either wall W or symmetry S conditions for the lateral boundary. Then an indication of the b.c. imposed is given, following the previous nomenclature of Tab. 4.2, and finally the confinement length normalized to the nominal case is specified with the XpXX numbers (e.g. $L_C = 2.5C$ is labelled as 2p50).

| $L_C/C$ | W - Isothermal b.c. | W - Adiabatic b.c. | S - Isothermal b.c. | S - Adiabatic b.c. |
|---|---|---|---|---|
| 0.5 | W-II-0p50 | W-AA-0p50 | S-I-0p50 | S-A-0p50 |
| 0.75 | W-II-0p75 | W-AA-0p75 | S-I-0p75 | S-A-0p75 |
| 1 | W-II-1p00 | W-AA-1p00 | S-I-1p00 | S-A-1p00 |
| 1.25 | W-II-1p25 | W-AA-1p25 | S-I-1p25 | S-A-1p25 |
| 1.5 | W-II-1p50 | W-AA-1p50 | S-I-1p50 | S-A-1p50 |
| 1.75 | W-II-1p75 | W-AA-1p75 | S-I-1p75 | S-A-1p75 |
| 2 | W-II-2p00 | W-AA-2p00 | S-I-2p00 | S-A-2p00 |
| 2.25 | W-II-2p25 | W-AA-2p25 | S-I-2p25 | S-A-2p25 |
| 2.5 | W-II-2p50 | W-AA-2p50 | S-I-2p50 | S-A-2p50 |

**Table 4.3:** Labels of the simulations carried out for the parametric analysis. W stands for wall-bounded and S for symmetry-bounded.

The parametric analysis is performed only through the variation of the injection plate confinement length $L_C$, while the injector geometry is kept fixed. For each case, a numerical grid has been defined by modifying the number of computational grid points on the transverse direction so as to consistently maintain the radial grid spacing constant. All injection conditions, namely the chamber pressure as well as the temperature and mass fluxes of both the fuel and the oxidizer, are also kept fixed.

For each value of $L_C$, the resulting wall heat flux $q$ is calculated from the isothermal configuration, together with the near-wall mixture fraction $Z$ representing the local composition. The adiabatic simulation, on the other hand, provides insight on the adiabatic wall temperature $T_{ad}$, while the convective heat transfer coefficient $h_C$ is calculated for each location on the walls as:

$$h_C = \frac{q}{T_{ad} - T_W} \tag{4.1}$$

with $T_W$ the temperature imposed at the wall.

### 4.4.1 Lateral chamber wall

First, the effect of the confinement variation is investigated on the combustion chamber lateral wall, therefore only the results corresponding to the wall-bounded configuration are reported.

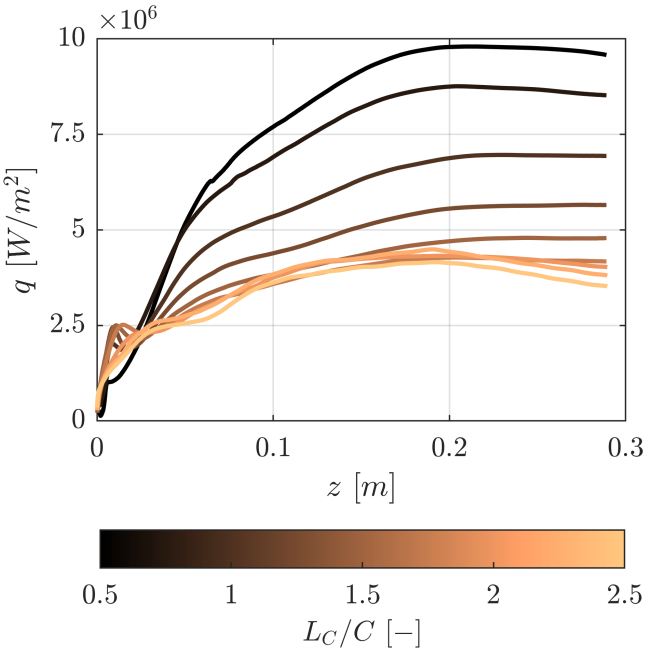


(**a**) Time-averaged wall heat flux.

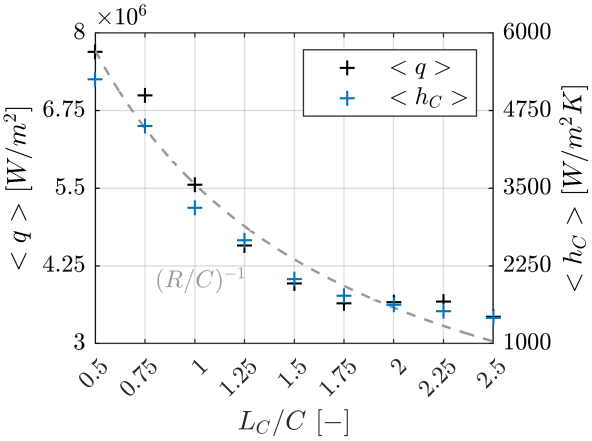


(**b**) Surface-averaged values of wall heat flux $q$ and heat transfer coefficient $h_C$.

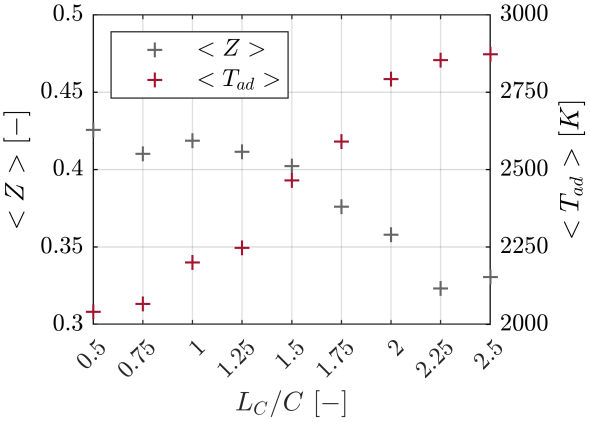


(**c**) Surface-averaged values of mixture fraction $Z$ and adiabatic temperature $T_{ad}$.

**Figure 4.10:** Confinement effects on chamber wall heat transfer for the wall-bounded configuration.

Figure 4.10a shows the time-averaged heat flux over the combustion chamber lateral wall for the different cases in the dataset. The heat flux is found to be decreasing with increasing confinement lengths. In this context, the variation of the confinement length can be considered akin to the variation of the radius of a cylindrical cavity. According to this analogy, the diffusive flame placed within the cavity exchanges heat towards an increasing surface, thus the wall heat flux is expected to be inversely proportional to the cylinder lateral surface, as reported in Fig. 4.10b. The profiles display some scatter in the first section of the combustor, suggesting that geometry variations mostly affect the recirculation region, as expected from our parametric analysis.

In Fig. 4.10b surface-averaged values of heat flux and heat transfer coefficient are reported as functions of $L_C/C$. The two quantities present similar decreasing trends, indicating that for this wall, the driving phenomenon is the heat flux variation. In order to help the reader, Fig. 4.10b shows also the functional trend $1/R$, where $R$ is the combustion chamber radius, i.e. the sum of the injector radius and the confinement length. The adiabatic wall temperature trend is reported in Fig. 4.10c also as a function of $L_C/C$. Although a variation of $\langle T_{ad} \rangle$ is indeed observed, this is rather limited and it can be considered negligible with respect to variation of the same variable on the injection plate that will be shown in the following subsection. In fact, it is shown that within the considered confinement range, $\langle T_{ad} \rangle$ reaches $\sim 1.3$ times its minimum value, i.e. the value obtained for the smallest confinement $L_C/C = 0.5$. The mixture fraction trend along the chamber wall is also reported, showing as expected a negligible variation between $\sim 0.45$ and $\sim 0.35$.

### 4.4.2 Injection plate

The analysis is now shifted to the injection plate. The dominating phenomena on this wall and in the entire injection region are related to the presence of the recirculating flow pattern and are therefore expected to be intrinsically different from what previously observed for the developed flow on the lateral wall.

Figures 4.11a and 4.12a show the time-averaged heat flux for each confinement length for the two configurations considered: in both cases an overall increasing heat flux trend with increasing $L_C$ is found, while the profiles shape along the $x$ axis remain similar for each configuration. Despite the increasing heat flux, it can be observed from Fig. 4.11b and 4.12b that the heat transfer coefficient is decreasing, implying that in Eq. 4.1 the primary effect is an increase of the denominator $T_{ad} - T_w$. In addition, observing Fig. 4.11c and 4.12c it is indeed possible to note a steep increase of $\langle T_{ad} \rangle$, that triples over the confinements range. Moreover, conversely to the results presented for the lateral chamber wall in Subsec. 4.4.1, a significant variation in the mixture fraction is observed with $L_C/C$, with the smallest confinement lengths being characterized by near-wall composition of almost pure methane $\langle Z \rangle \sim 1$ for both the considered configurations.

The effect of the confinement length on the near-plate temperature field can be further observed in Fig. 4.13, where three representative cases are taken from each configuration. In particular, the extremal confinement lengths $L_C = 0.5C$ and $L_C = 2.5C$ are considered, together with the nominal case $L_C = C$. For each selected case, time-averaged temperature, velocity and mixture fraction fields are reported, respectively by means of color-code, streamlines and isolines. As it can be observed, when a small confinement is considered, e.g. in W-II-0p50 and S-I-0p50, the flame develops parallel to the longitudinal direction, having therefore little or no interaction with the recirculation bubble, which remains mainly composed of cold fuel-rich mixture $Z > 0.5$. As a result, the ensuing heat flux is low. On the other hand, for a large confinement length, as in W-II-2p50 and S-I-2p50, the instantaneous flame interacts with the recirculation bubble, occasionally intersecting with it and causing the average flame to impinge on the lateral boundary closer to the injection plate. The recirculating flow pattern brings the hot flame products from the flame region toward the injection plate, increasing the near-wall temperature and, as a consequence, the heat flux.

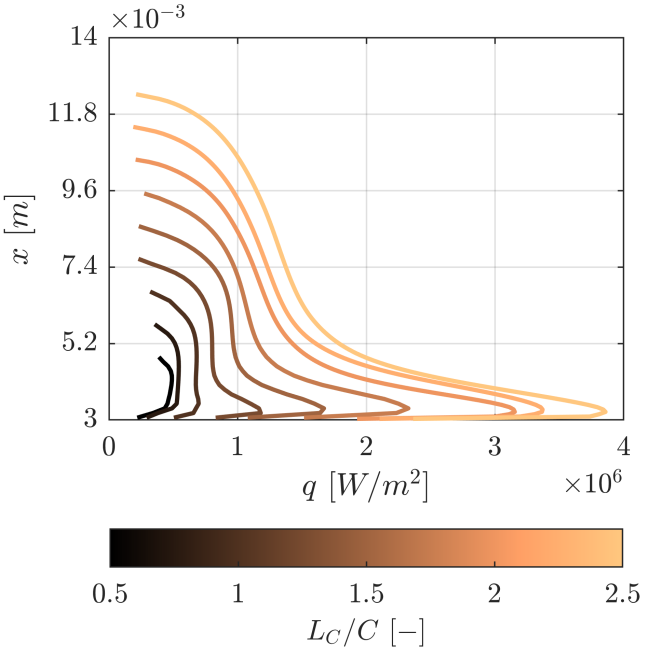


(**a**) Time-averaged wall heat flux.

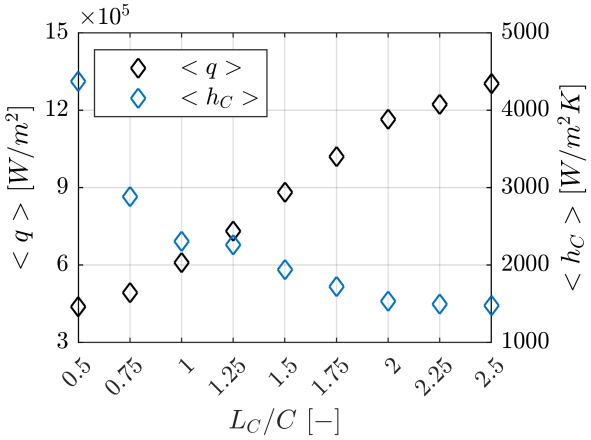


(**b**) Surface-averaged values of wall heat flux $q$ and heat transfer coefficient $h_C$.

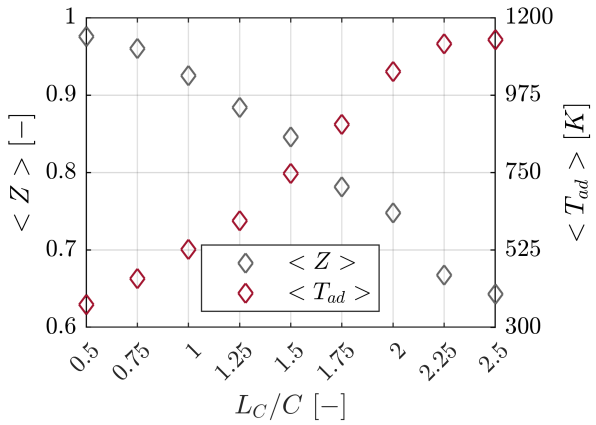


(**c**) Surface-averaged values of mixture fraction $Z$ and adiabatic temperature $T_{ad}$.

**Figure 4.11:** Confinement effects on injection plate heat transfer for the wall-bounded configuration.

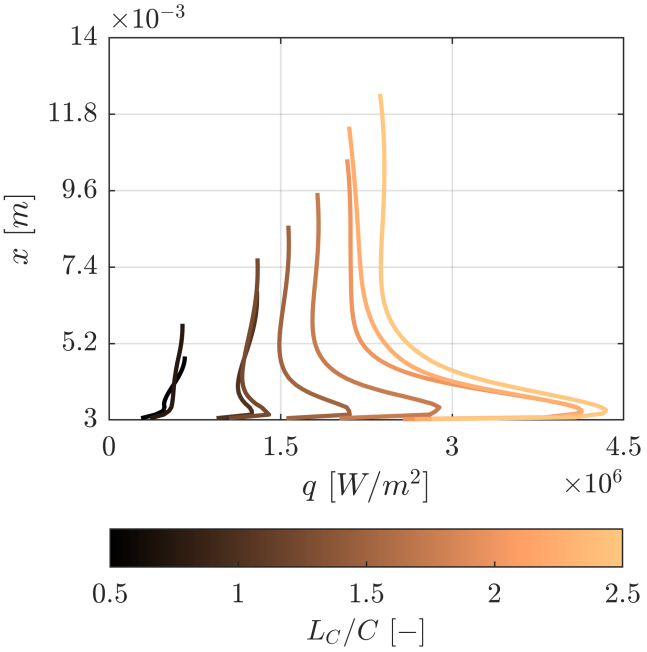


(**a**) Time-averaged wall heat flux.

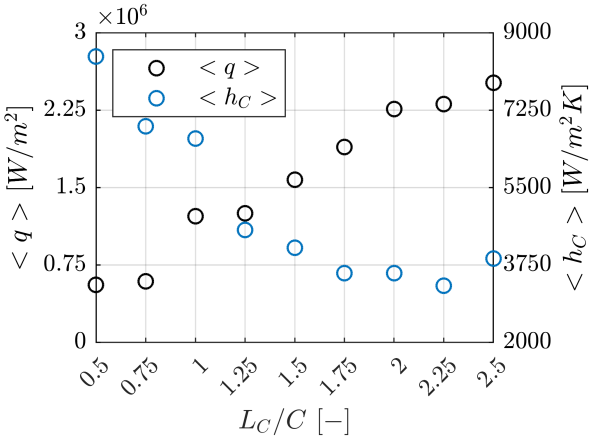


(**b**) Surface-averaged values of wall heat flux $q$ and heat transfer coefficient $h_C$.

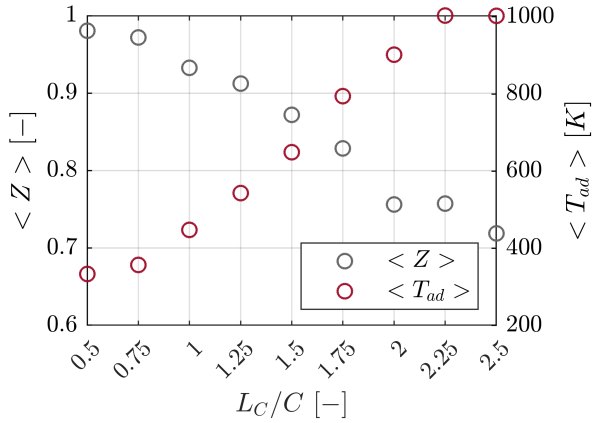


(**c**) Surface-averaged values of mixture fraction $Z$ and adiabatic temperature $T_{ad}$.

**Figure 4.12:** Confinement effects on injection plate heat transfer for the symmetric configuration.

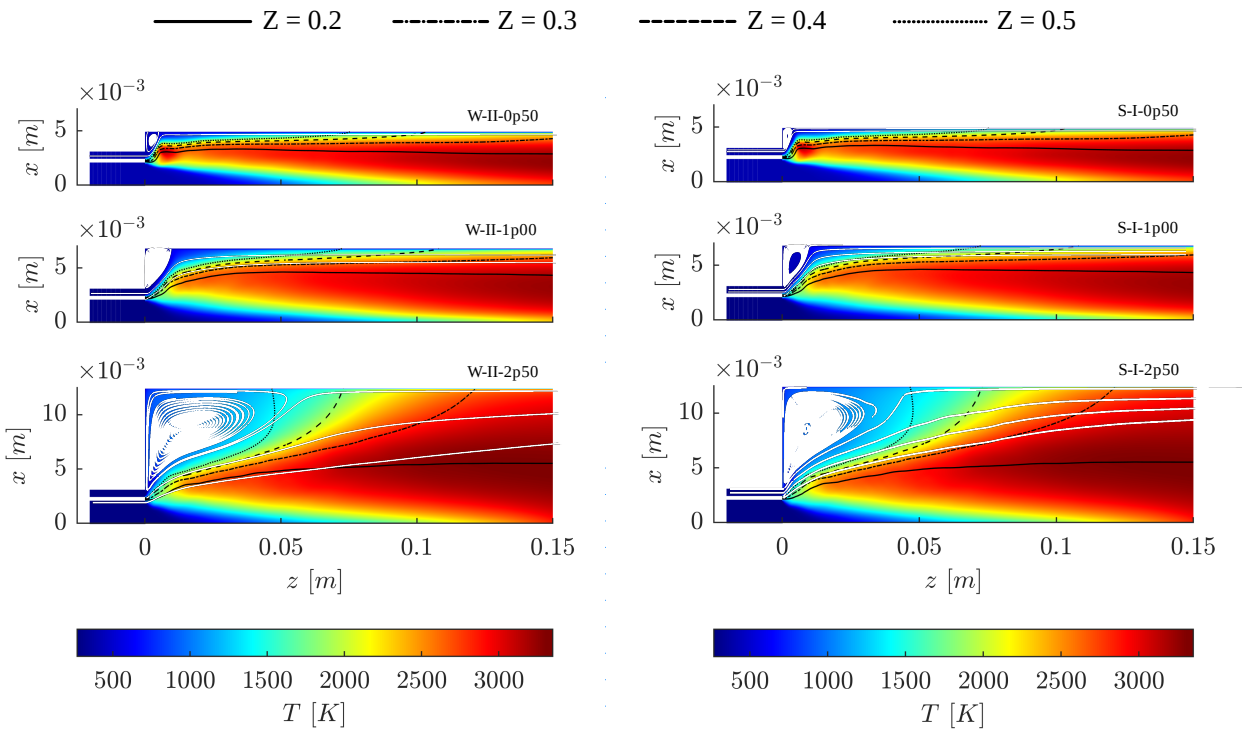


(**a**) Wall-bounded database.

(**b**) Symmetric database.

**Figure 4.13:** Flame-flow interaction. Representation of time-averaged temperature field (colored), velocity streamlines (white) and mixture fraction isolines (black, legend on top). Axes not to scale.

### 4.4.3 Comparison between configurations

The trends obtained for the two configurations are now compared with each other. Figure 4.14 shows the surface-averaged quantities over the injection plates of both the symmetry-bounded and wall-bounded configurations. Heat flux $\langle q \rangle$, heat transfer coefficient $\langle h_C \rangle$, mixture fraction $\langle Z \rangle$ and adiabatic wall temperature $\langle T_{ad} \rangle$ for each configuration were fitted with a power law as a function of the normalized confinement length, i.e. $f(L_C/C) = a + b * (L_C/C)^c$. The coefficients $c$ are discussed in the following.

| Quantity | Wall-bounded plate | Symmetry-bounded plate |
|---|---|---|
| $\langle q \rangle$ | 0.74 | 1.03 |
| $\langle h_C \rangle$ | -0.61 | -0.66 |
| $\langle Z \rangle$ | -0.2 | -0.26 |
| $\langle T_{ad} \rangle$ | 0.79 | 0.77 |

**Table 4.4:** Scaling coefficient for the injection plates of the two considered configuration.

Similar functional trends can be observed when comparing the two configurations. In particular, $\langle q \rangle$ is found to scale almost linearly with the confinement length, similarly to $\langle T_{ad} \rangle$, while $\langle h_C \rangle$ and $\langle Z \rangle$ decrease with the confinement. The scaling coefficients are reported in Fig. 4.14 as well as in Tab. 4.4 to ease the comparison. The similarity of the coefficients for each analyzed quantity shows that both injection plate can be well characterized with the same scaling laws. Observing Fig. 4.14c and 4.14d it can be noted that $\langle Z \rangle$ and $\langle T_{ad} \rangle$ are also characterized by similar quantitative

values. This suggests that the temperature and composition near the injection plate are almost the same, regardless of the lateral bounding condition, especially when small confinements $L_C/C < 2$ are considered. Despite this, quantitative heat flux values are significantly different for the two configurations, as reported in Fig. 4.14a, owing to the intrinsic differences between the kinematic fields already discussed.

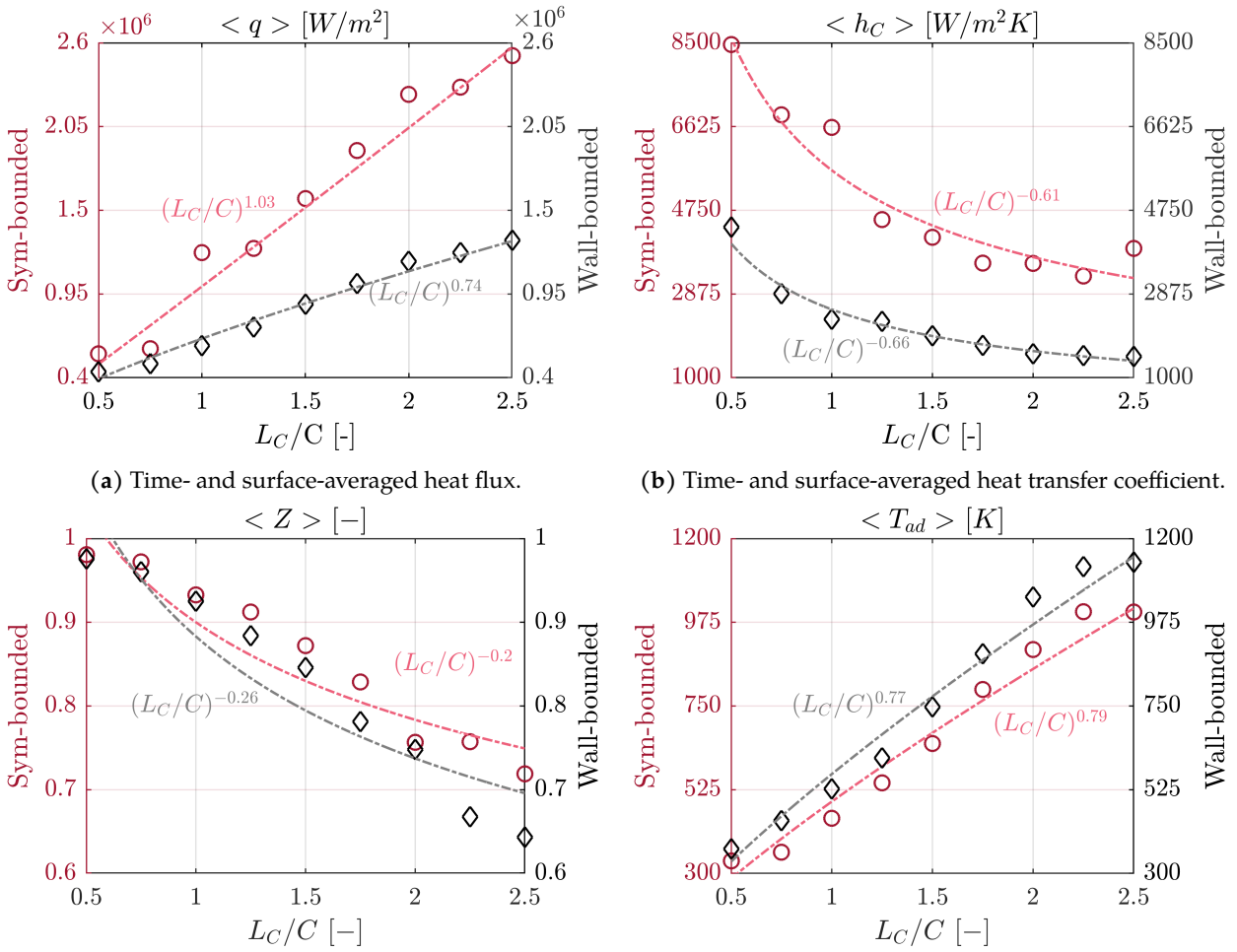


**(a)** Time- and surface-averaged heat flux.

**(b)** Time- and surface-averaged heat transfer coefficient.

**(c)** Time- and surface-averaged mixture fraction.

**(d)** Time- and surface-averaged adiabatic temperature.

**Figure 4.14:** Comparison between scaling trend obtained through linear regression on the injection plates of the two configurations.

Based on the foregoing analysis, the geometry variation mainly affects the recirculation region. The analysis is therefore now focused on this section of the wall-bounded configuration. In particular, quantities are sampled on the first segment of the chamber lateral wall, indicated in Fig. 4.15 by the blue arrow, and compared to those sampled from the injection plate. The label "lateral wall" in Fig. 4.16 will therefore refer to the wall section ahead of the stagnation point instead that the entire lateral wall. In particular, the stagnation point has been defined for each run as the location of the null time-averaged axial velocity, as indicated in Fig. 4.15.

It is found that the trends seen in Fig. 4.10 for the entire lateral wall are not confirmed when considering only the wall section impinged by the recirculation bubble. On the contrary, the observed trends are in agreement with those found on the injection plate. The surface-averaged heat transfer coefficient $\langle h_C \rangle$ shown in Fig 4.16b decreases with confinement length $L_C/C$ suggesting that the driving phenomenon on the initial section of lateral wall is the flame-velocity interaction

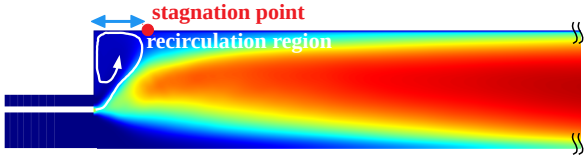


**Figure 4.15:** Zoomed view on the recirculation region, highlighted in white.

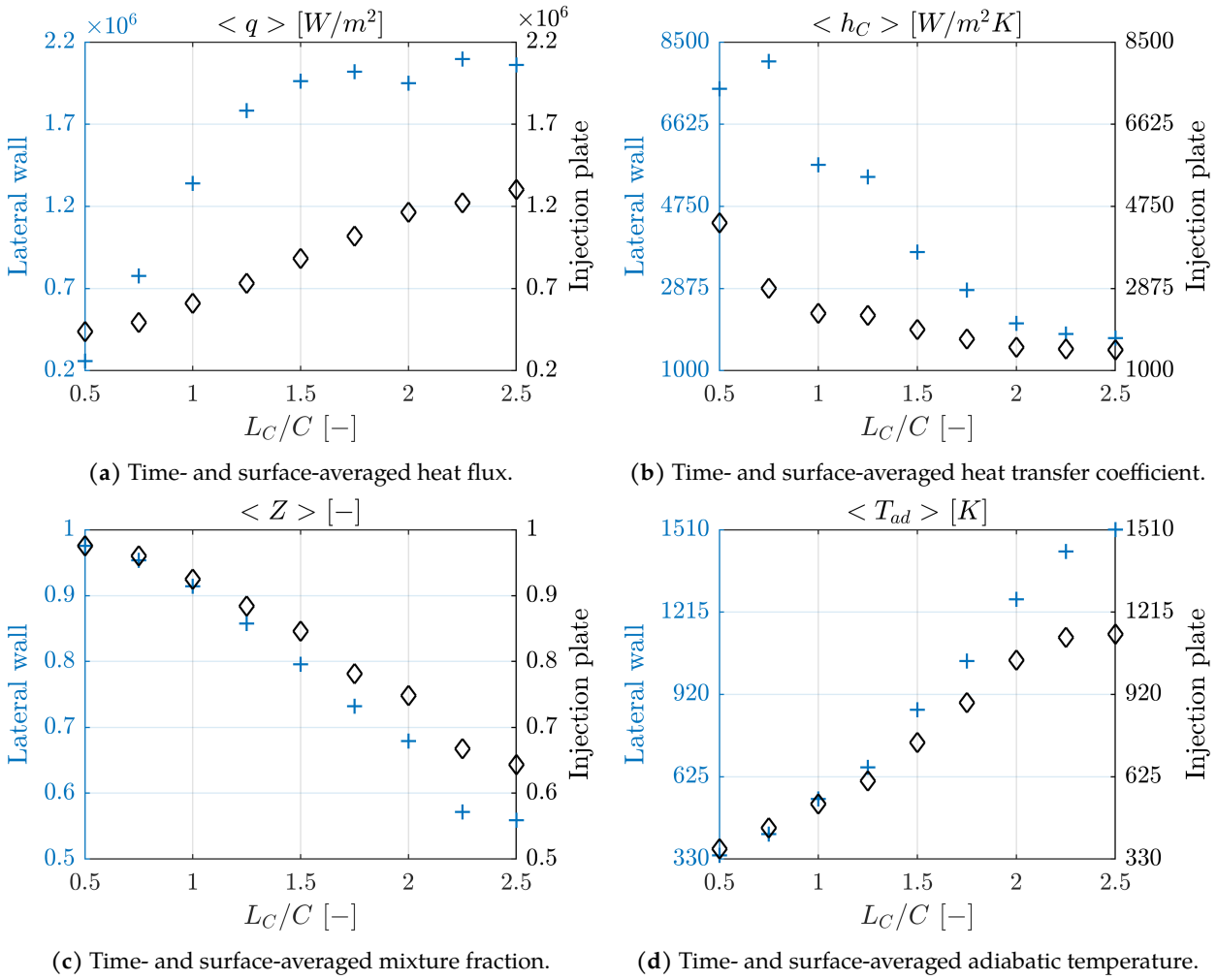


**(a)** Time- and surface-averaged heat flux.

**(b)** Time- and surface-averaged heat transfer coefficient.

**(c)** Time- and surface-averaged mixture fraction.

**(d)** Time- and surface-averaged adiabatic temperature.

**Figure 4.16:** Comparison between trend observed on the wall-bounded injection plate and on the section of chamber lateral wall corresponding to the recirculation bubble.

characterizing the injection region as already discussed in Fig. 4.13. It can indeed be observed that also the functional trends presented by heat flux $\langle q \rangle$, mixture fraction $\langle Z \rangle$ and adiabatic temperature $\langle T_{ad} \rangle$ are in agreement with those observed on the injection plate. In addition, $\langle Z \rangle$ (Fig. 4.16c) and $\langle T_{ad} \rangle$ (Fig. 4.16d) show similar quantitative values especially for $L_C/C < 1.5$, indicating that the two walls experience similar recirculating flow temperature and composition. Owing to the differences in the temperature values imposed at the walls, it is not possible to perform a quantitative comparison on the heat flux values and on the subsequent heat transfer coefficient values. Nevertheless, this analysis indicates that the first section of the lateral wall can be assumed as representative, in terms of functional trends, of the injection plate region, confirming the considerations

on previously mentioned works [105, 120].

## 4.5 Towards a data-driven model for multi-injector combustion chambers

The correlation between heat flux and geometry gleaned from the database collection can be used to develop a data-driven model for the thermal load estimation in the design stage of a multi-injector combustion chamber once the injector layout is known. The development of such a model is still in a preliminary stage, the results discussed in this section must be therefore considered as less mature than the rest of the work.

The main idea at the basis of the data-driven model is that for each injector on the firing plate it is possible to define an equivalent confinement depending on the mutual placement of the surrounding injectors and on the distance from the chamber wall. Such an algorithm would be comprised of three steps, it will be here discussed with reference to the heat flux and the thermal characterization, but it could be similarly used with any quantity collected on the walls. In order to ease the discussion, each of the steps constituting the algorithm will be illustrated through its application to the injection plate of the 37 injectors combustor presented in Sec. 4.3. Figure 4.17 shows the time-averaged heat flux and mixture fraction fields on the injection plate, the former will be taken as reference field for the reconstruction model. The reader is referred to the pseudo-code reported in App. A to further support the discussion.

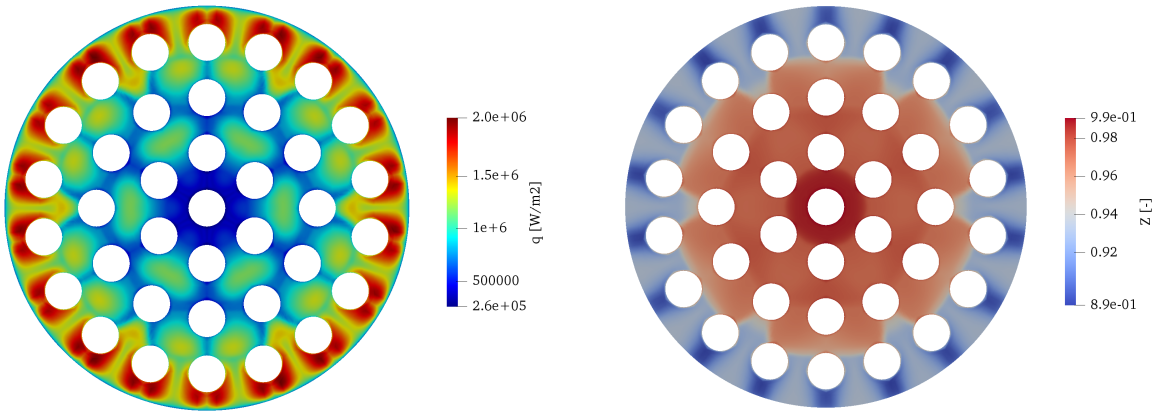


**Figure 4.17:** Injection plate fields from the 3D simulation: time-averaged heat flux (left) and mixture fraction (right) fields.

### Tiling

First the multi-injector plate is topologically tiled into cells on the basis of the injector mutual placement. Each cell is built following geometrical criteria based on the plate symmetry axes. A representation of the tiled injection plate is given in Fig. 4.18, from a visual comparison with Fig. 4.17 it is possible to observe that the cells trace the flux stagnation lines with the edges, so that the overall tiling is well representative of the characteristic flow pattern. It must be highlighted that the tiling process is solely based on the plate layout and that it does not require the prior knowledge of the

flow pattern. The correspondence between the tiles' edges and the stagnation lines is an important byproduct of the model.

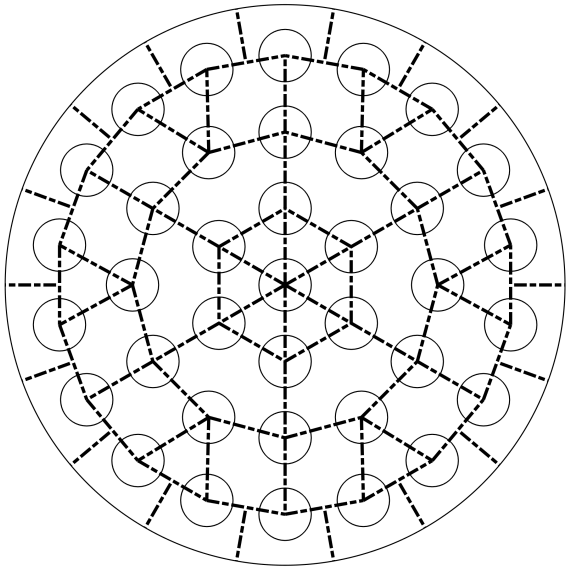

**Figure 4.18:** Topological tiling.

### Mapping

Secondly, equivalent confinements are defined over the cells, and for each of those a value of heat flux is taken from the database and mapped over the geometry, as schematically represented in Fig. 4.19, where different colors have been used for the different sources of the data. The wall-bounded database (represented in blue) will be used to model the external injector ring confining with the combustor wall, while the symmetric database (red) will be used among the internal injectors, both on the conjunction lines between neighbouring injectors and over the diagonals within each topological shape. In the former case, in particular, data are taken from the database and straightforwardly mapped on the plate in accordance with the symmetry condition definition. In the latter case, instead, a representative confinement of the cell is defined as the average distance between the cell's vertices and the centroid. The heat flux value corresponding to such an average distance is then taken from the database and shrunk or stretched over the length of the inner diagonals in the topological tile.

### Reconstructing

Finally the heat flux mapped values are interpolated over the plate surface in order to reconstruct the heat flux field, as shown in Fig. 4.20. The natural neighbor interpolation method is used, which finds the closest subset of input samples to a query point and applies weights to them based on proportionate areas in order to interpolate a value [108]. Compared to the linear interpolation, such a method provides a smoother approximation of the objective function, with $C^1$ continuous results except at the sample points.

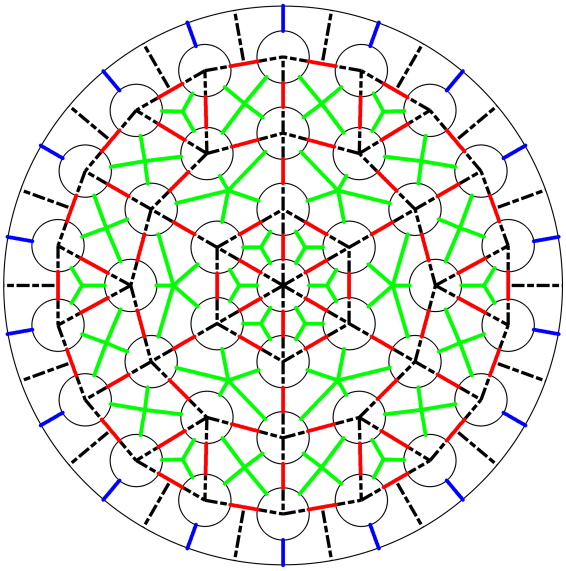

**Figure 4.19:** Definition of equivalent confinements and enforcement of conditions from the databases. Blue and red lines represent respectively data taken from the wall-bounded and the symmetric databases, while the green lines represent the data taken from the symmetric databases and interpolated over each cell's average diagonal.

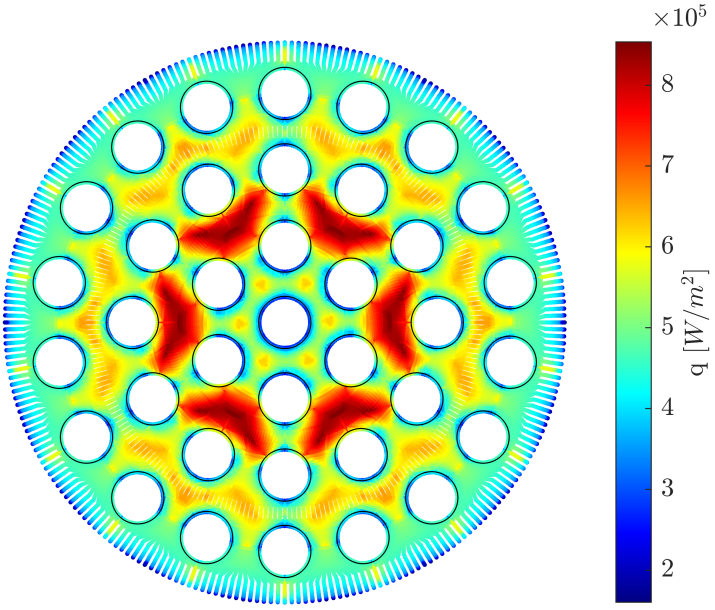


**Figure 4.20:** Reconstructed heat flux field.

### Outcomes

Although not showing correspondence between the heat flux values, it can be observed a good approximation of the field pattern, characterized by higher thermal loads were the injector are less dense, also confirming the trends seen in the previous Sections. A possible source of the dis-

crepancies can be addressed to the reference 37 injectors configuration, which has been inspired by a laboratory scale combustor and presents a much more dense injector distribution compared to the standard rocket geometries and prevents therefore the formation of standard recirculation patterns. This model has already shown promising results in a previous preliminary work [102], where it has been applied to an real-scale rocket combustion chamber. Figure 4.21 shows the heat flux values from the corresponding simulations normalized to the peak value and represented as a function of the normalized radial distance from the injector plate centre. In particular the black dots represent the results of the three-dimensional simulation while the green markers are those reconstructed with the data-driven model, it is possible to see that the heat flux distribution is well reproduced.

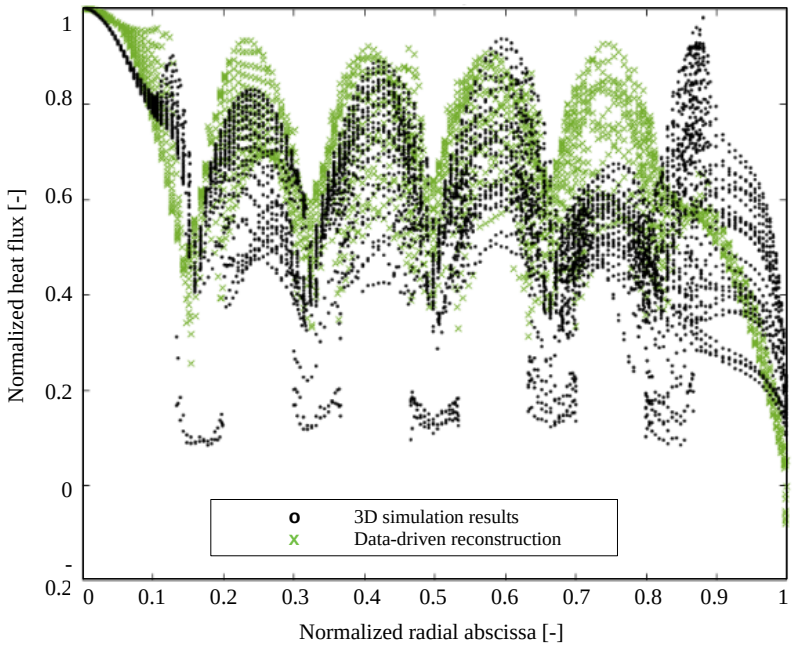


**Figure 4.21:** Comparison between the heat flux obtained with a three-dimensional simulation (black) and the heat flux reconstructed with the data-driven model (green) on an industrial-scale configuration. The heat flux values are normalized to the peak values while the data are represented in terms of normalized radial abscissa.

The results presented in this Section are nevertheless preliminary and unripe, and will be therefore deepened in future studies.

# Chapter 5

# Multi-region analysis of coupled combustion chambers

## Contents



## Nomenclature

**Latin letters**

| | |
|---|---|
| $h_C$ | = Heat transfer coefficient |
| $k$ | = Solid-fluid thermal conductivity ratio |
| $O/F$ | = Oxidizer-to-fuel ratio |
| $t$ | = Time |
| $t_F$ | = Flow-through time |
| $T$ | = Temperature |
| $x$ | = Radial coordinate |
| $y$ | = Width coordinate |
| $z$ | = Longitudinal coordinate |

**Greek letters**

| | |
|---|---|
| $\Theta$ | = Non-dimensional temperature |
| $\lambda$ | = Thermal conductivity |

**Subscripts and superscripts**

| | |
|---|---|
| $\square_{\mathrm{F}}$ | = Fluid-side value |
| $\square_{\mathrm{int}}$ | = Interface value |
| $\square_{\mathrm{S}}$ | = Solid-side value |

In this Chapter the multi-region solver presented in Chapter 3 is validated against some preliminary cases and then used to characterize two experimental single and multi-injector combustors. First the coupling solution is validated against the well-known analytical solution of a multi-layer solid plate, then a backward facing step from the literature [100] is taken as a reference benchmark for a fluid-to-solid interface in a single-species and laminar setting. The solver is then applied to two experimental combustors: the single-injector TUM-rig combustor, simulated in both a 2D and 3D setting, and the TUM five-injector combustor, simulated only in a 3D setting.

## 5.1 Code validation

### 5.1.1 Analytical solution of the coupled interface

The implementation of the CHT boundary condition 2.15 presented in 2.3.1 has been in a first instance validated by comparison with the analytical solution of a multi-layer plate with different temperature imposed at the boundaries.

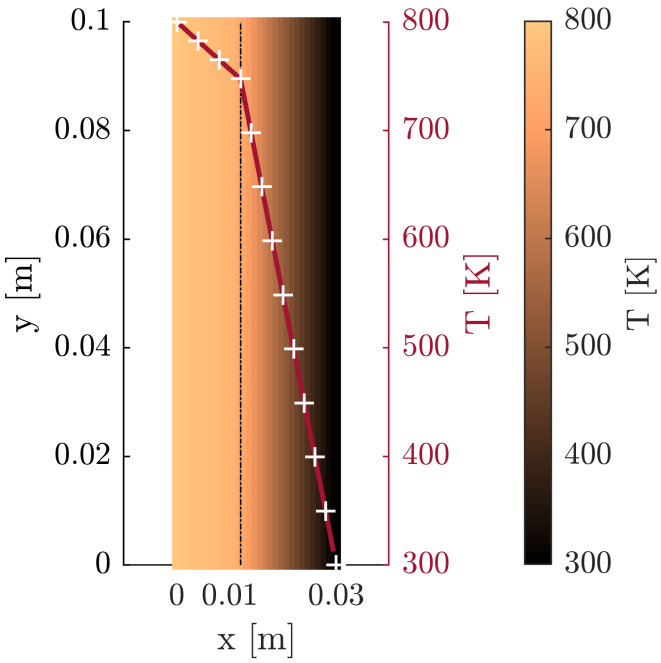


**Figure 5.1:** Multi-layer wall. The heat map and the solid red line represent the temperature field resulting from the coupled simulation, compared to the analytical solution (white markers).

The color-coded field in Fig. 5.1 shows the temperature field in a section of the multi-layer plate when the steady state condition has been reached. The temperature profile along the plate centerline is reported by the solid red line, while the white crosses represent the analytical solution. It is found perfect correspondence between the two, both in terms of interface value and behaviour across the plate width. This testcase also proves that the solver is amenable to the simulation of multiple domains of the same kind.

### 5.1.2 Single-species laminar testcase

The solver is then validated in a two-dimensional, laminar and single-species setting, reproducing the results of a Backward Facing Step (BFS) from the literature [100], also used as benchmark testcase by other groups [25, 30]. The testcase consists in a cold air laminar stream flowing over a heated slab, the geometry and boundary condition of the BFS configuration are retained from the works of Ramsak [100] and of Kanna and Das [45]. Figure 5.2 shows the configuration, coloured by the steady-state temperature field in both the solid and fluid domains. The problem is treated in [100] in a non-dimensional fashion, and has been made dimensional in the present work. The fluid dynamic field is initialized with the fluid at rest, at the equilibrium temperature of $T_F = 273.15K$, and with a parabolic velocity profile imposed at the inlet. The solid domain has an initial

temperature of $T_S = 373.15K$, the same temperature is imposed at the slab bottom wall, while all the other walls of the test case, excluding the interface, are considered adiabatic. On the interface wall the CHT condition reported in Eq. 2.15 is enforced. Among the various solid-fluid thermal conductivity ratios $\overline{k} = \lambda_S/\lambda_F$ analyzed by Ramsak, the present testcase refers to $\overline{k} = 1000$.

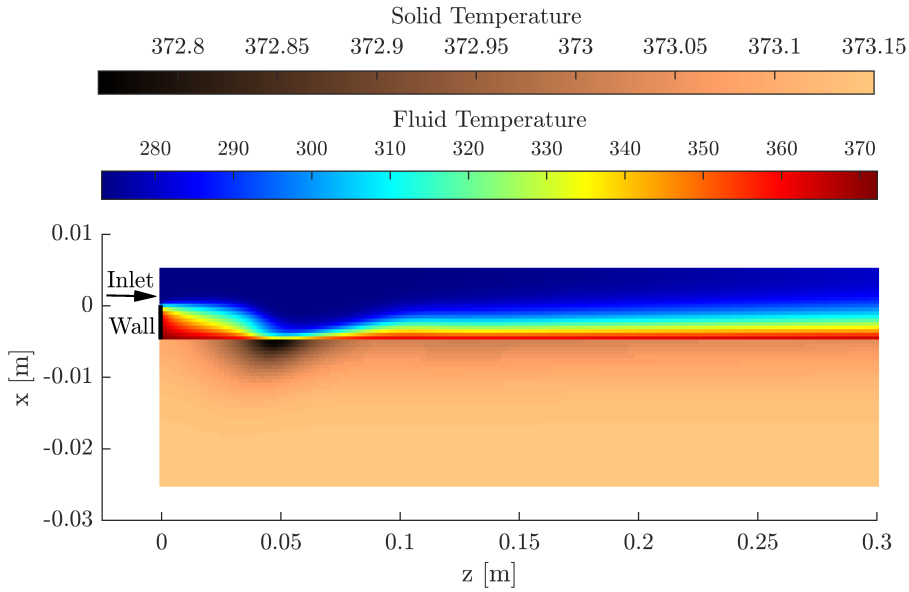


**Figure 5.2:** Backward facing step configuration.

### Grid assessment study

An extensive grid-convergence analysis has been performed comparing the results calculated on four meshes, obtained one from each other doubling the number of computational points in each direction. Table 5.1 reports the main grid characteristics, while Fig. 5.3 shows the non-dimensional interface temperature $\Theta_{\text{int}}$ obtained on the several grids. Each grid is named BFS-X with X a number in increasing order of refinement. It is possible to see that the finest grids BFS-3 and BFS-4 produce overlapping results, therefore the grid convergence is attained. Moreover, a time convergence study has been performed, in order to assess the minimum simulation time that guarantees the attainment of the steady state condition.

| | No. Fluid finite volumes | No. Solid finite volumes |
|---|---|---|
| BFS-1 | 3000 | 6000 |
| BFS-2 | 12000 | 24000 |
| BFS-3 | 48000 | 96000 |
| BFS-4 | 192000 | 384000 |

**Table 5.1:** Numerical grids used for the convergence analysis of the BFS testcase.

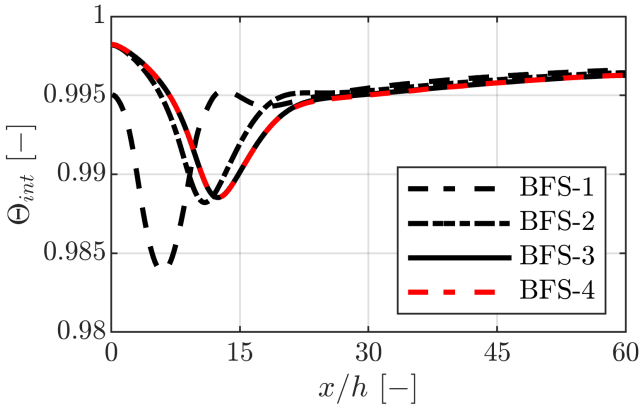


**Figure 5.3:** Interface normalized temperature $\Theta_{\text{int}}$ obtained with four different numerical grids for the BFS testcase. Comparison performed after the attainment of a steady-state.

### Results

Figure 5.4 shows the non-dimensional interface temperature $\Theta_{\text{int}}$ and Nusselt number $Nu_{\text{int}}$ compared with the literature data and with the results obtained with *chtMultiRegionFoam*, a native OpenFOAM solver for Conjugate Heat Transfer, enforcing the same interface condition and embedding the same solver for the solid domain. Following what done in [100], the non-dimensional Nusselt number is defined as:

$$\text{Nu}(x) = -\frac{\partial \Theta}{\partial n}\bigg|_{\text{wall}} \tag{5.1}$$

with $n$ the direction normal to the interface.
Results show good agreement with the literature data, providing even an improvement of the accuracy in the near-peak region with respect to the native OpenFOAM solver.

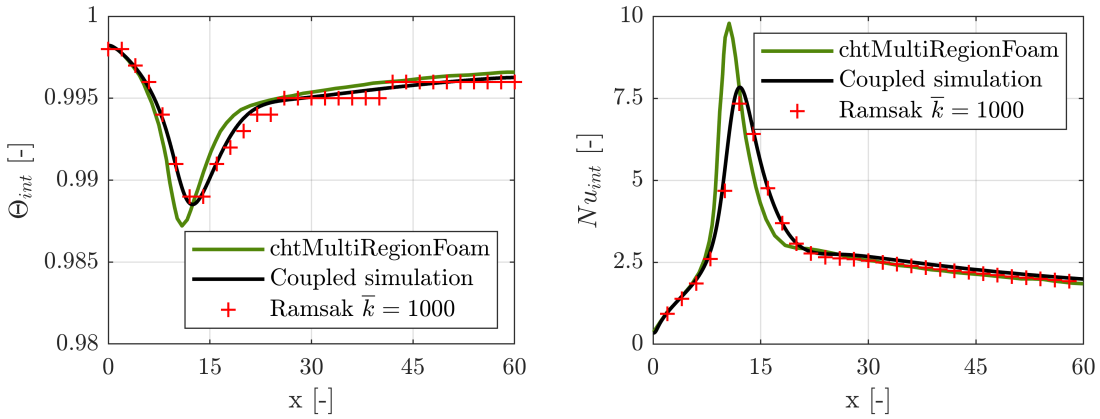


**Figure 5.4:** Non-dimensionalized temperature and Nusselt number at the interface, obtained with the developed solver and with a *chtMultiRegionFoam*, compared to literature data.

## 5.2 2D single-injector combustion chamber

The complete multi-region formulation, featuring the alternation between CHT and Newton boundary conditions (cfr. Eq. 2.15 and Eq. 2.16) is now applied to the experimental TUMrig combustor developed at the Technical University of Munich. The facility is capacitively cooled by means of oxygen-free copper (Cu-HCP) walls, and has been simulated in a first instance adopting a two-dimensional axis-symmetric approximation, prior the definition of proper equivalent radii. More specifically, for the fluid domain the radius of the equivalent cylinder has been calculated in order to maintain the mass-flow rate as done in Sec. 4.1, while for the solid domain the rectangular section has been transformed in an equivalent annulus maintaining the total mass. The entire duration of the experimental run, consisting in 3 seconds of burning time, has been simulated resorting to the alternation of the interface conditions Eq. 2.15 and Eq. 2.16. Figure 5.5 shows the boundary condition setup employed in this and in the following two sections. The interface condition (Eq. 2.15 and Eq. 2.16) is enforced on the chamber lateral wall and injection plate, while on the solid external wall is enforced a natural convection boundary condition with external air at $T_{\text{air}} = 290$ K and convective heat transfer coefficient $h_{C_{\text{air}}} = 10$ W/$m^2$K, enforcing a continuity constraint for temperature and heat flux formally equivalent to Eq. 2.16. All the other walls are considered adiabatic, following what done by Perakis and Haidn in [83]. The solid domain is initializated in equilibrium with the external ambient, therefore with an initial uniform temperature $T_{\text{Solid}} = 290$ K. The fluid domain is truncated in correspondence of the nozzle inlet, according to the employed low-Mach hypothesis, while the solid domain length covers both injector and nozzle, this choice allowing to avoid the heat confining in the ending portion of the wall. A zero fluid-to-solid heat flux in correspondence of the interface patches has been used for the two-dimensional simulation in order to model the chamber quenching. The load point here considered corresponds to a pressure of 20 bar and an $O/F = 2.6$, the complete set of injection conditions can be found in [15].

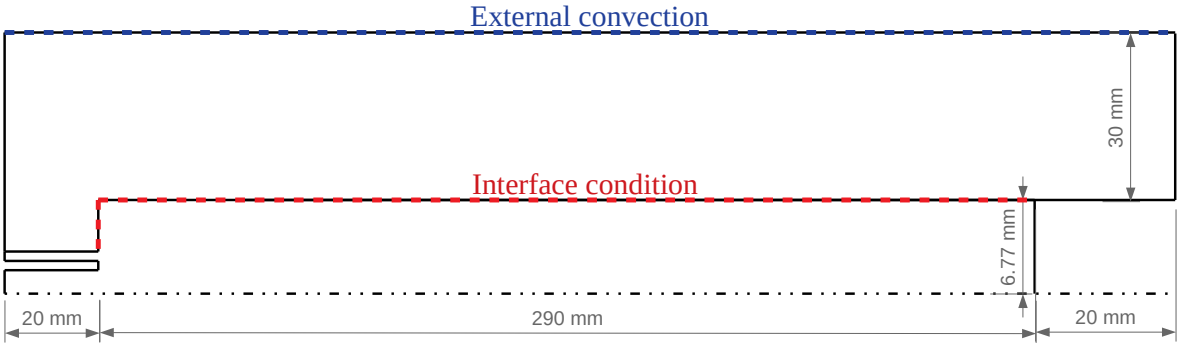


**Figure 5.5:** Boundary conditions settings. The dimensions refer to the 2D axis-symmetric configuration.

### Grid assessment study

Following what done in the previous subsection, a grid assessment study has been performed comparing the results obtained with four meshes, one originated from each other by doubling the number of points in each direction. Table 5.2 reports the main grid characteristics, the labels are numbered also in this case in increasing order of refinement.

| | No. Fluid finite volumes | No. Solid finite volumes |
|---|---|---|
| TUMrig 2D-1 | 1699 | 1786 |
| TUMrig 2D-2 | 6796 | 7146 |
| TUMrig 2D-3 | 27184 | 28584 |
| TUMrig 2D-4 | 108736 | 114336 |

**Table 5.2:** Numerical grids used for the convergence analysis of the 2D TUMrig testcase.

The comparison is performed in terms of interface temperature, since the wall heating is an intrinsically transient phenomena, results are shown both in terms of profile at a given time instant (upper left panel of Fig. 5.6 and 5.7) and as function of time at several control stations along the surface. Results in time are expressed in unit of flow-through time. Figure 5.6 shows the results for the combustor chamber lateral wall, the three control abscissas have been chosen in order to coincide with the locations of three experimental thermocouples. Figures 5.7 shows instead the results obtained on the injection wall, in this case three generic equispaced points have been chosen given the absence of experimental probes. In both cases it is possible to see that the finest grid TUMrig 2D-4 has not been started from t = 0 due to its elevated computational cost, but has been initialized from a later time instant mapped from the TUMrig 2D-3 simulation.
Figures 5.6 and 5.7 demonstrate the achievement of asymptotic convergence, the TUMrig 2D-3 grid has been therefore chosen as baseline grid, providing a trade-off solution between accuracy and cost.

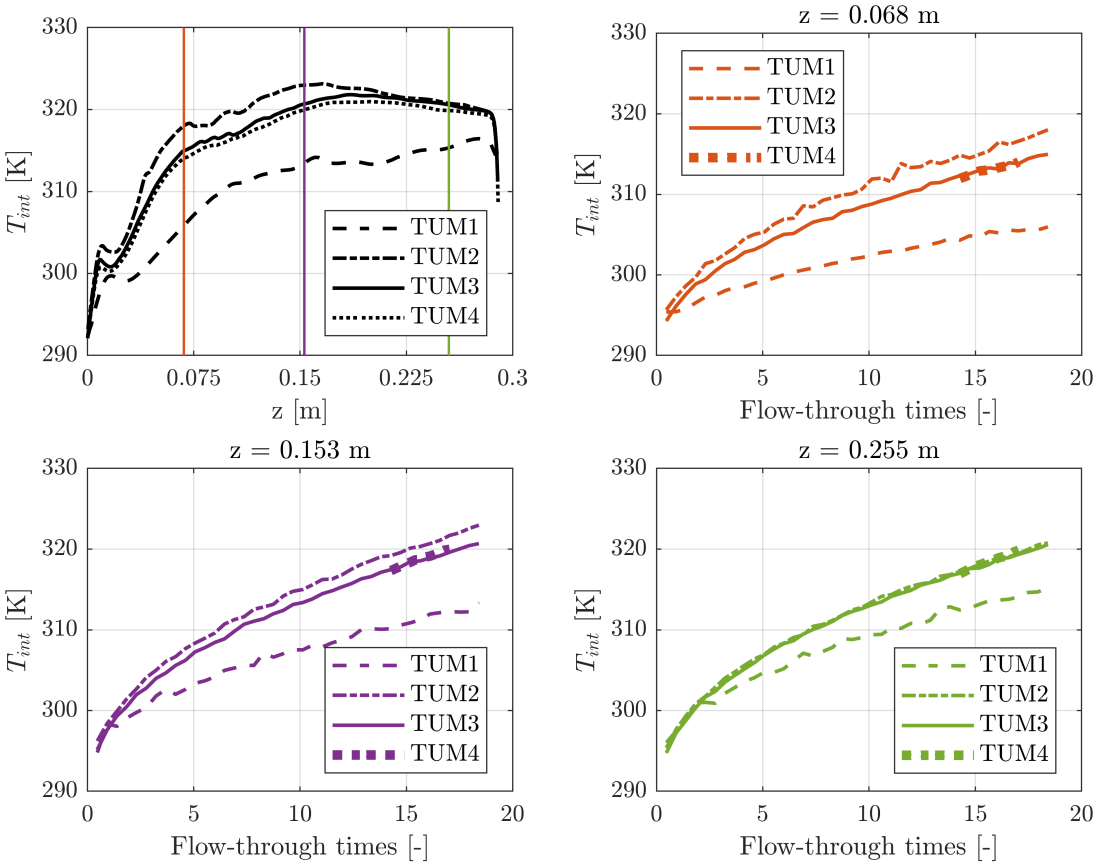


**Figure 5.6:** Grid convergence: chamber wall interface temperature at given time (upper left panel) and temperature evolution in time for several grids.

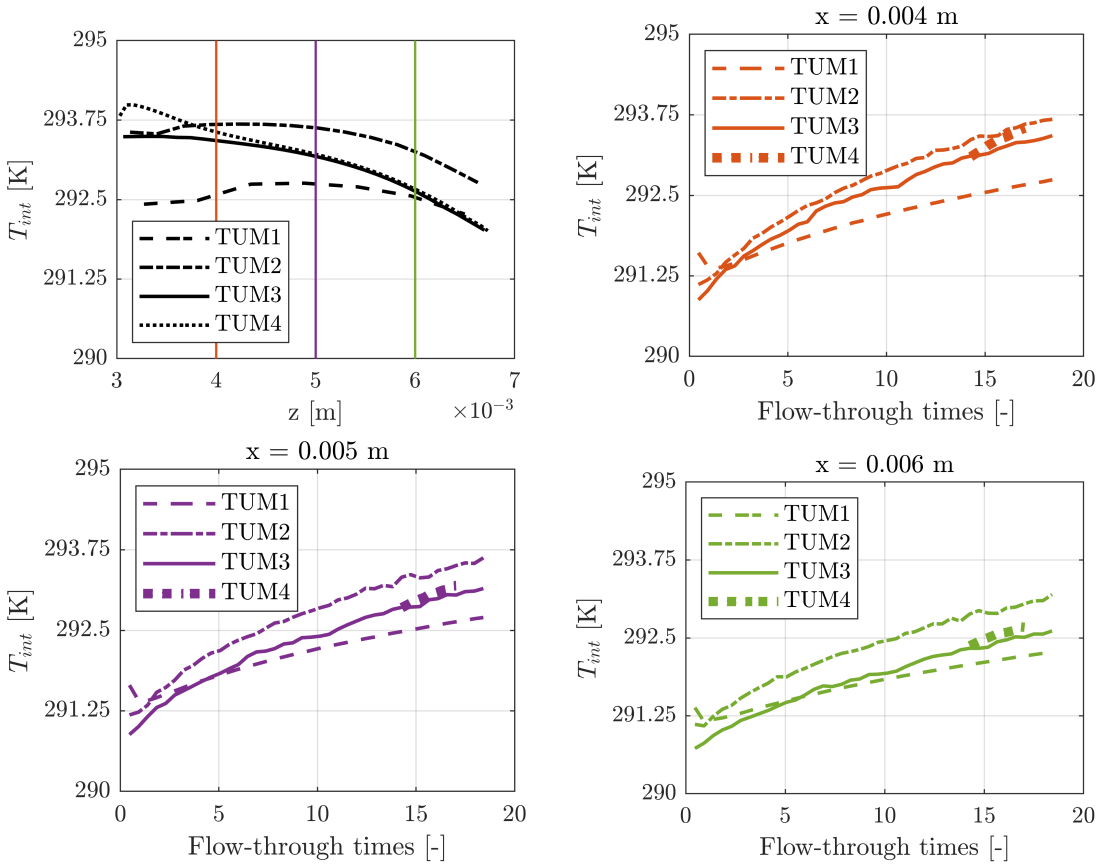


**Figure 5.7:** Grid convergence: injection plate interface temperature at given time (upper left panel) and temperature evolution in time for several grids.

### Results

In order to apply the coupling strategy presented in Sec. 2.3, it must be verified that the heat transfer coefficient $h_C$ defined in Eq. 4.1 attains a steady state value, and that can therefore be fed into the Newton interface condition of Eq. 2.16 as a constant parameter. This has been done monitoring the $h_C$ coefficient evolution over approximately 20 flow-through times. The left panels of Fig. 5.8 show the time-averaged heat transfer coefficient calculated on the chamber lateral wall and injection plate at several time instants, it is possible to see how the profiles progressively collapse on a constant value after an initial transient. On the right panels instead, instantaneous and time-averaged $h_C$ values are reported, respectively with dashed and solid lines, as a function of flow-through time units for the three previously introduced control stations on each wall. A satisfactory statistical steady state was already obtained after $\sim 5$ flow-through times.

The continuity of the interface temperature after the variation of the interface modeling has been verified in Fig. 5.9, where the results of the fully coupled simulation performed with the CHT condition (Eq. 2.15) have been compared for overlapping time instants to those obtained with a simulation switched to the Newton boundary condition (Eq. 2.16). In particular Fig. 5.9 reports the instantaneous interface temperature in time for the aforementioned control points on both the lateral wall and injection plate, showing a satisfactory overlapping of the results calculated according with the two methods.

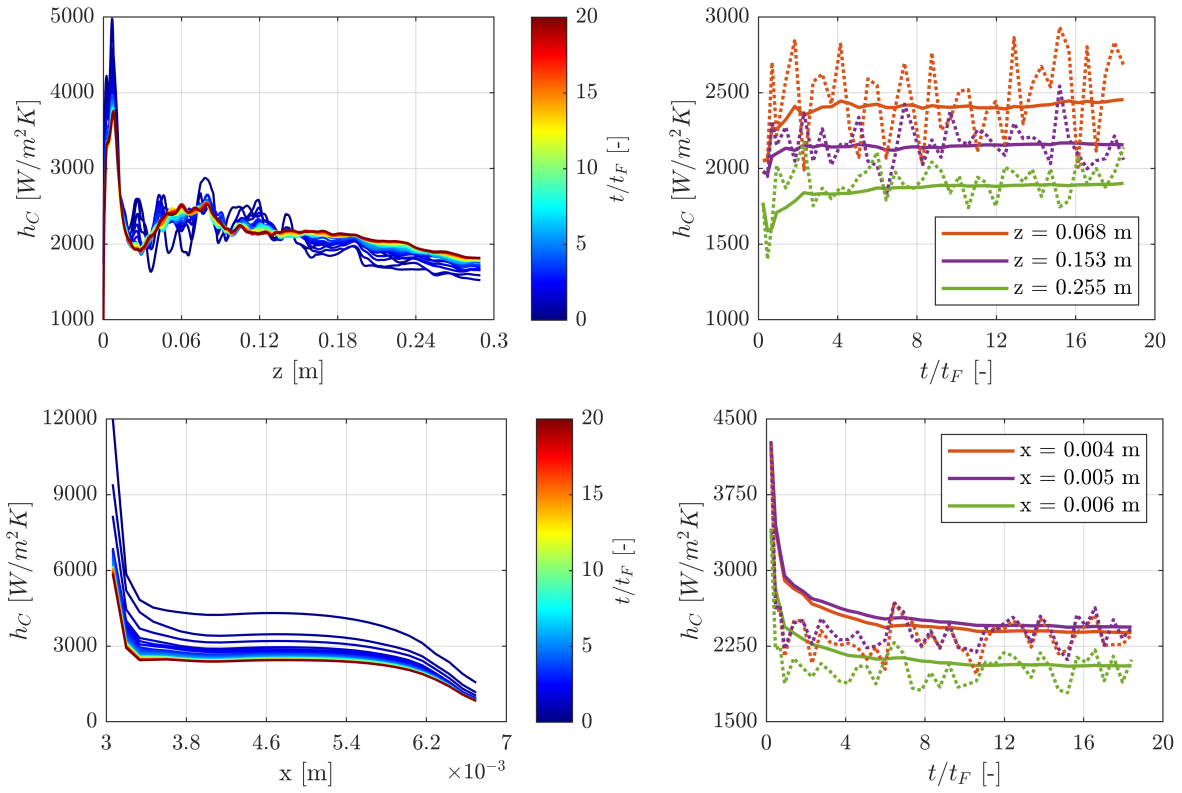


**Figure 5.8:** Convergence of the heat transfer coefficient to a steady value on the combustion chamber lateral wall (top) and injection plate wall (bottom). In the right panels, dashed lines represent instantaneous values, solid lines represent time-averaged values.

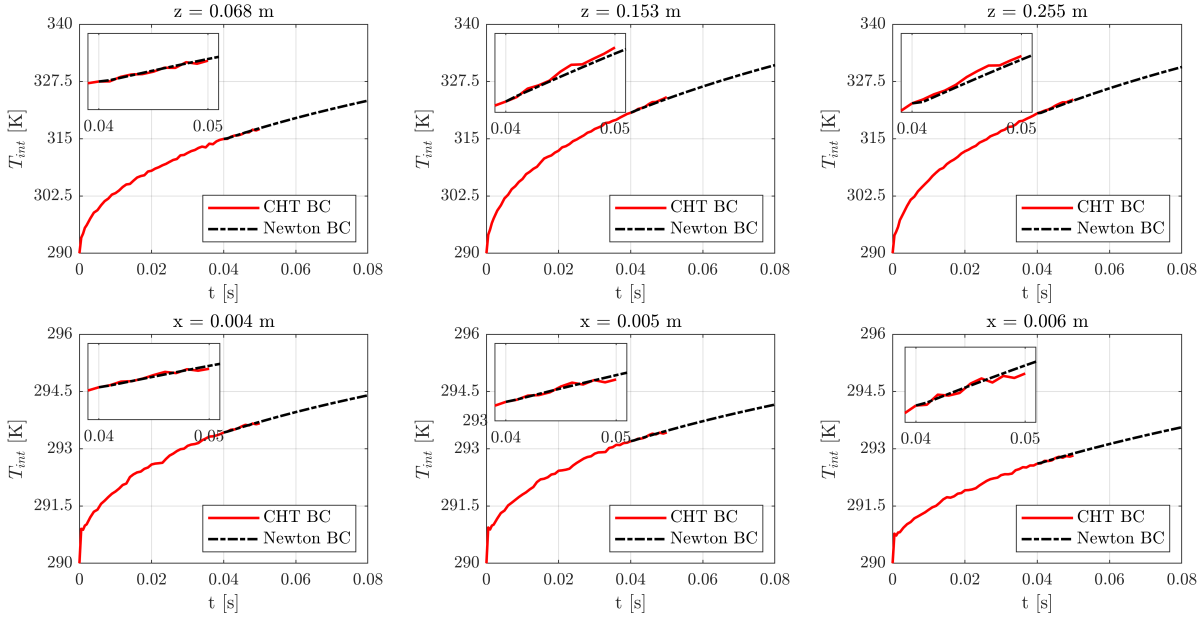


**Figure 5.9:** Continuity of the interface condition in terms of interface temperature evolution in time at several abscissas, for the lateral wall (upper panels) and injection plate (lower panels). Zoomed view on the time interval after the boundary condition switch, showing the equivalence of the interface temperature calculated according to the two methods.

The remaining duration of the experimental run has been simulated solving the heat conduction problem in the solid domain bounded with the Newton interface condition (Eq. 2.16), Fig. 5.10

shows the temperature field in the domains at the end of 3 seconds of burning time.

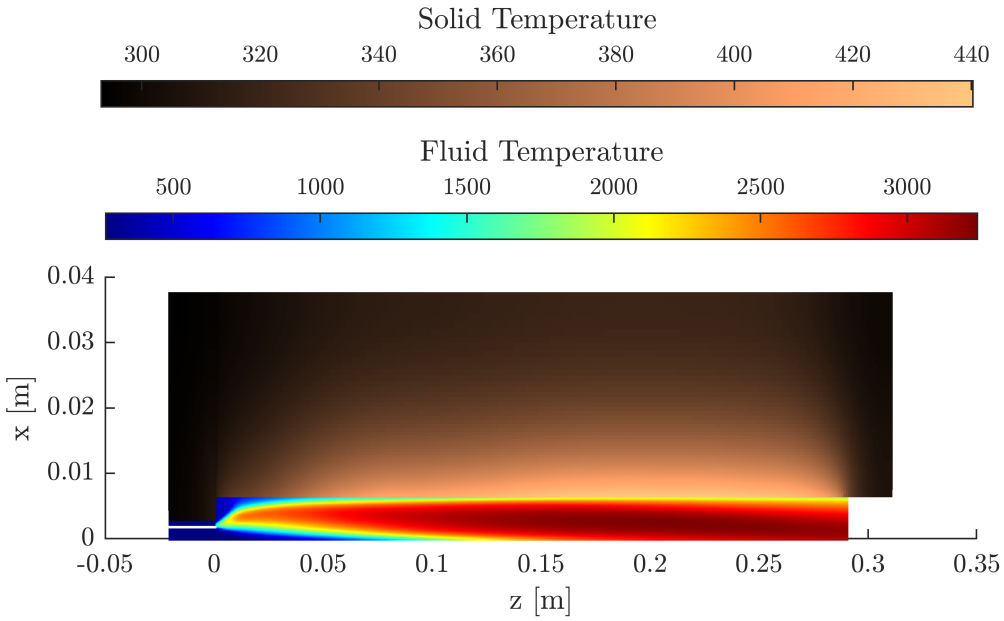


**Figure 5.10:** TUMrig combustion chamber configuration. Axes not to scale.

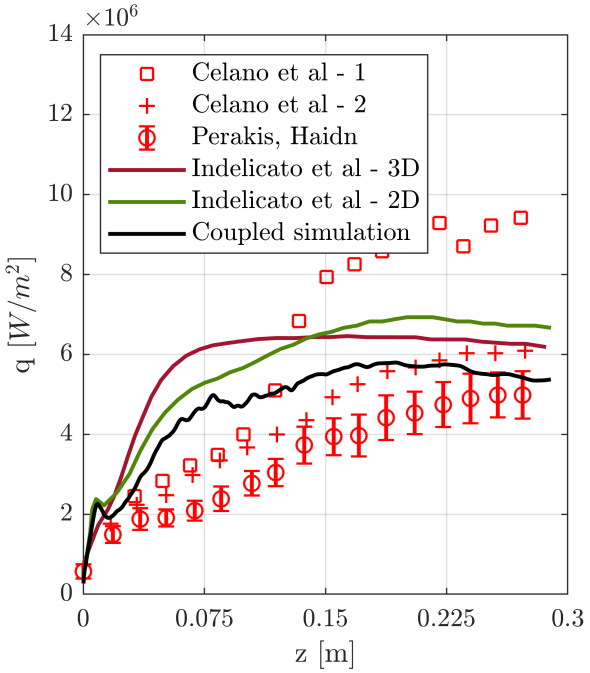


**Figure 5.11:** Heat flux at the interface compared to experimental and literature data.

Figure 5.11 shows the interface heat flux calculated on the combustor lateral wall at the end of the burning time, compared with experimental and literature results [15, 37, 83]. It is found an overall good agreement between the coupled simulation and the reference data, with a slight overestimation in the central section of the chamber, already observed in [37] and commented in Sec. 4.1.1. Among the comparative data, the red and green lines represent respectively the results of

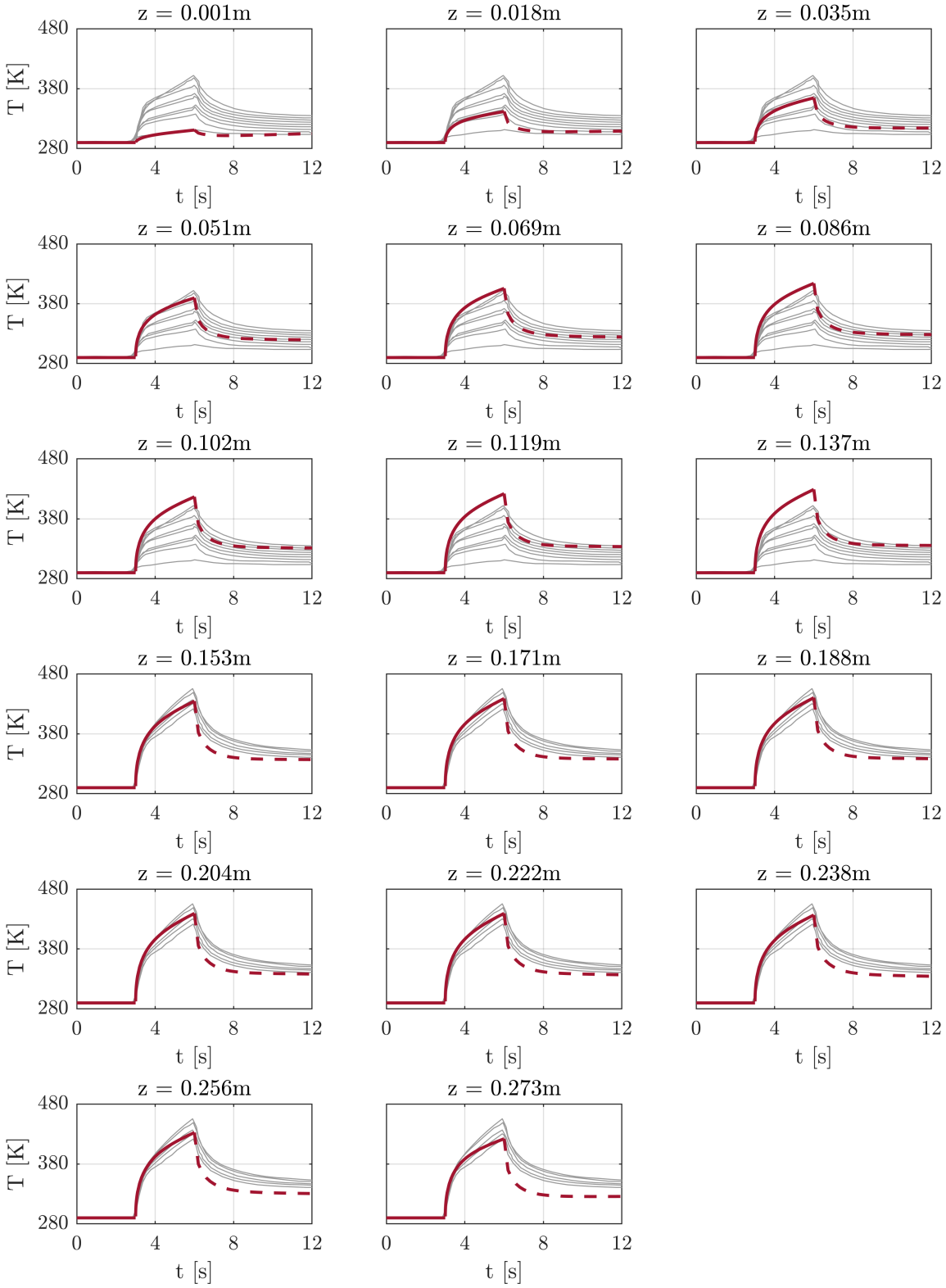


**Figure 5.12:** Temperature signal in time for several abscissas. Results of the coupled simulation (red) compared with the experimental thermocouples readings (gray). Dashed lines represent the chamber quenching.

a 3D and 2D axis-symmetric single-region simulation performed under equal fluid-dynamic solver and injection condition but in a single-region setting and therefore bounded with an isothermal boundary condition [37]. It is noteworthy the comparison with the isothermal two-dimensional axis-symmetric simulation: even though the imposed temperature is retained from the experimental data, it is possible to see that the predicted heat flux is higher with respect to the coupled simulation case. This is due to the fact that the isothermal condition neglects by definition the transient heating of the patch surface, which is instead described by the coupled simulation.

The capability of describing transient phenomena is highlighted in Fig. 5.12, where the temporal evolution of temperature is shown for several abscissas corresponding to the experimental thermocouples. Two groups of comparative data are taken from [15], respectively related to the experimental probes located in the first and second half of the combustion chamber. For this testcase, the chamber quenching has been simulated imposing a zero heat flux condition in correspondence to the interface walls, and letting the solid to cool down consequently. An overall good agreement is observed, but also in this case the sampling points in the central chamber section are affected by an overestimation of the peak value. With respect to the chamber shutoff phase, represented in the figure by the dashed lines, it is observed that the temperature drops with a steeper slope compared to the experimental data. This is due to the significant approximation introduced imposing a zero heat flux condition, that neglects the residual heat exchanged with the hot burnt gases flowing out of the combustion chamber.

## 5.3 3D single-injector combustion chamber

The numerical framework presented is now employed in a three dimensional setting. The TUMrig combustor is still investigated, selecting a chamber pressure of $20$ bar and $O/F = 3.0$, in order to match the load point indicated by Perakis and Haidn in their reference work [83] and by Winter et al. in [122].

### Grid assessment study

The numerical grid used for the fluid-domain of the present testcase has been inherited from a previous single-region simulation [37]. The grid used in the solid domain has instead been built in order to have correspondence between faces of the finite volumes on the fluid-solid interface boundary, with a cell spacing across the width defined in order to have an average distance between neighbouring computational nodes of $\sim 0.5$ mm, following what done in the reference work by Perakis and Haidn [83]. In order to assess the grid independence two numerical grids have been tested, whose labelling and main characteristics are reported in Tab 5.3. Figure 5.13 shows the evolution in time of the interface temperature obtained with the two grids for four control abscissas along the longitudinal direction. Overlapping signals are found, demonstrating the grid independence of the results. The finest grid TUMrig 3D-2 is therefore taken as baseline numerical grid.

| | No. Fluid finite volumes | No. Solid finite volumes |
|---|---|---|
| TUMrig 3D-1 | 131472 | 835000 |
| TUMrig 3D-2 | 1051776 | 6680000 |

**Table 5.3:** Numerical grids used for the convergence analysis of the 3D TUMrig single-injector testcase.

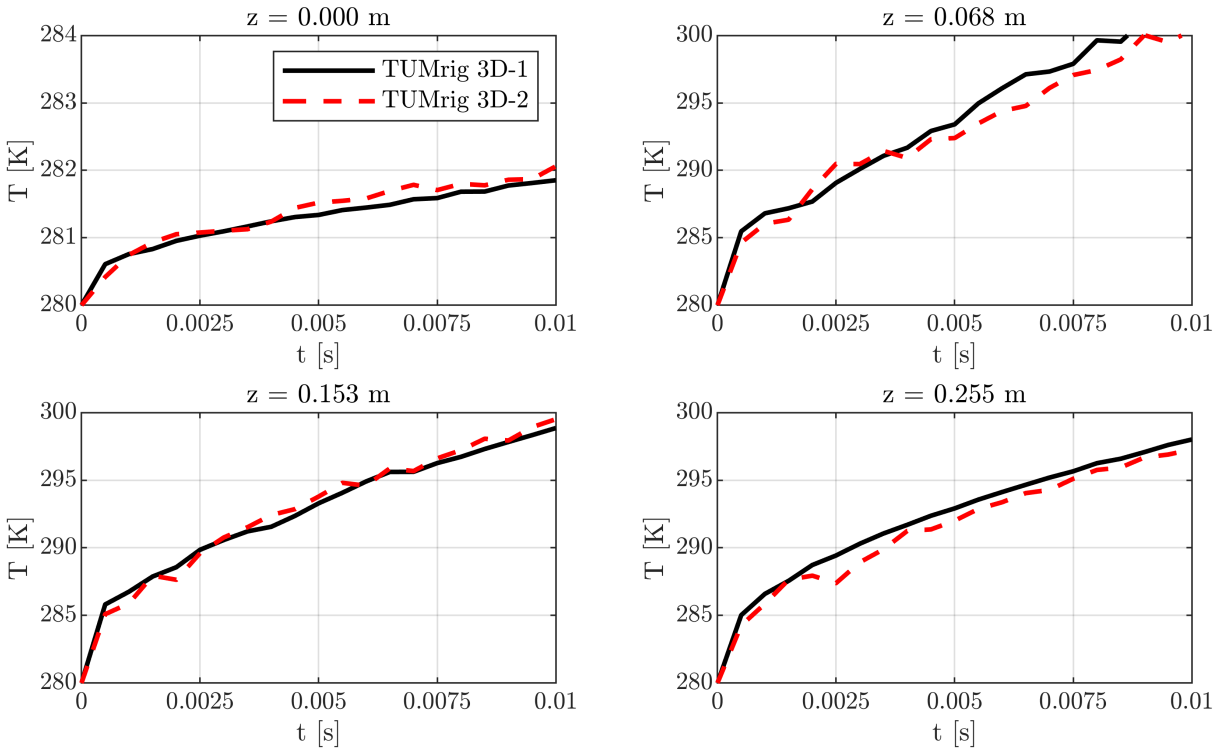


**Figure 5.13:** Interface temperature in time at several abscissas on the chamber upper wall for two different numerical grids in the 3D TUMrig testcase.

### Results

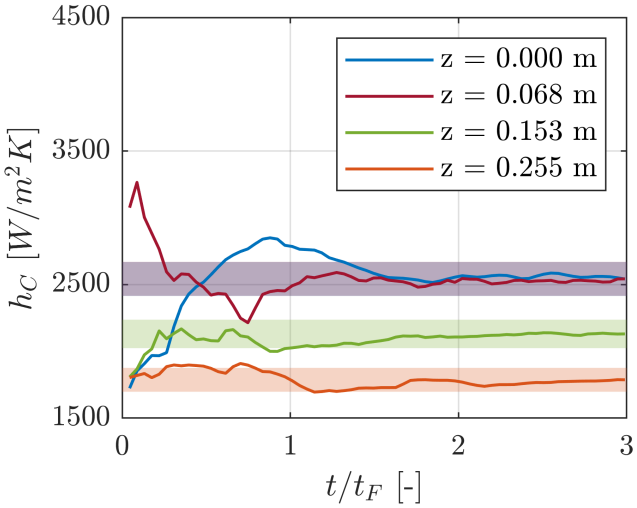


**Figure 5.14:** Attainment of a steady state value of $h_C$ in the 3D single-injector configuration. Colored bands represent a 10% variation on the final $h_C$ value.

Following what done in the previous Section, the time convergence of the heat transfer coefficient $h_C$ has been verified, as shown in Fig. 5.14 for four locations along the longitudinal direction. Those locations corresponds to four experimental thermocouples, and are respectively representative of the injection region ($z = 0.0$ m), the mixing region ($z = 0.068$ m), the mean flame impingement zone over the chamber wall ($z = 0.153$ m) and the final chamber section experiencing

the fully developed flow of burnt gases ($z = 0.255$ m). It is shown that the statistical steady state value is obtained after $\sim 3$ flow-through times. Figure 5.14 highlights in particular a 10% variation on the final $h_C$ value, demonstrating that the steady state value is maintained for the duration of an entire flow-through time. The fully coupled simulation was also continued beyond $t/t_F = 3$ to provide a reference for the interface temperatures obtained switching to the Newton condition, as shown in Fig. 5.15.

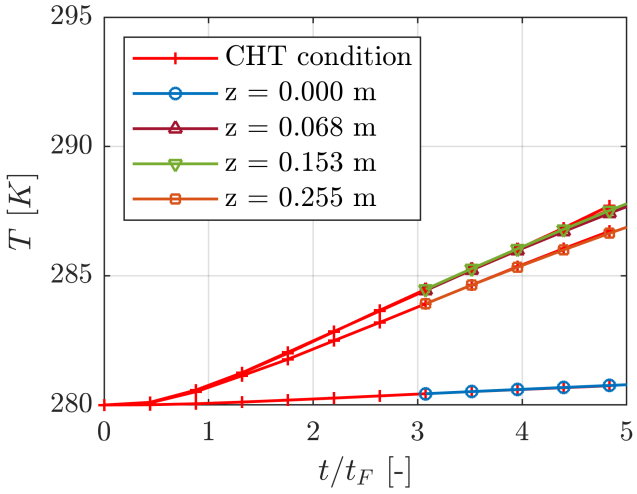


**Figure 5.15:** Continuity of the interface condition in terms of interface temperature evolution in time at several abscissas.

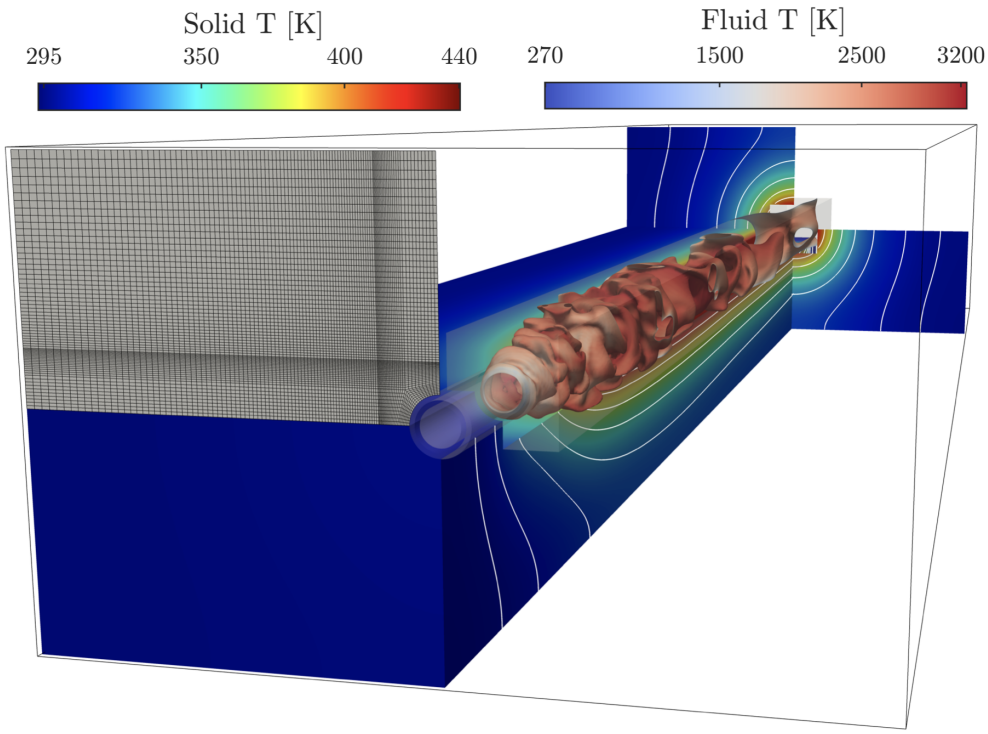


**Figure 5.16:** 3D single injector with instantaneous isosurface of stoichiometric mixture fraction colored by temperature.

The attainment of a steady state $h_C$ allows for the application of the coupling strategy described in Sec. 2.4, starting from $t/t_F = 3$ where a constant $h_C$ was assumed. Figure 5.16 shows the TUMrig combustor coloured with the temperature field in the solid domain at the end of 3 seconds of burning time and with instantaneous isosurfaces of mixture fraction coloured with temperature in the fluid domain.
The temperature evolution in time over the duration of the experimental run is reported in Fig. 5.17, where it is compared to the results obtained by Perakis and Haidn in [83].

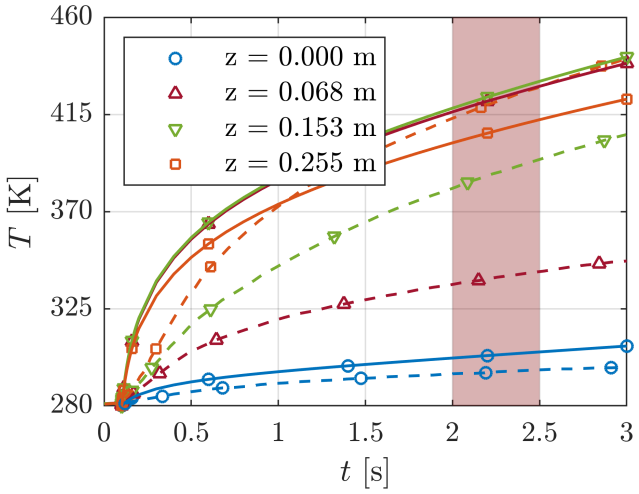


**Figure 5.17:** Temperature evolution in time for several thermocouples. Results of the coupled simulation (solid lines) compared to results form [83] (dashed). The vertical band highlights the evaluation time.

The temperature profiles at the injection region and at the terminating portion of the chamber show satisfactory agreement with the reference data, while an overestimation is found in the central section of the combustor, as already observed in the previous section for the two-dimensional case. The slight underestimation of the temperature data for the thermocouple location nearest to the outlet section can be attributed to the enforcement of the adiabatic condition over the solid surfaces in correspondence of the nozzle area. In the reference work of Maestro et al [72] it is in fact observed that the sections in proximity of the chamber outlet are highly affected by the thermal modeling of the nozzle segment and that the enforcement of an adiabatic condition, in particular, leads to an underestimation of the temperatures signals obtained in proximity of the chamber outlet compared to those obtained by means of an isothermal wall modeling. The time interval between 2 s and 2.5 s, highlighted in Fig. (5.17), is taken as a reference evaluation time window, and used to obtain time-averaged values of the temperature field in the solid domain. A slice of the latter is shown in Fig. (5.18) compared alongside the temperature field presented in [83], highlighting an overall good agreement of the thermal fields inside the solid region.

The key characteristic of the proposed coupling strategy is that it allows to avoid any initial thermal assumption on the wall modeling, and that it is therefore fully predictive on the temperature evolution. For these reason, this test case represents an ideal test bench to further verify the assumption of lateral wall representative of the injection plate suggested by [105, 120] and already discussed in Sec 4.4.3. Figure 5.19 shows the temperature at the end of the experimental run, sampled over the injection plate and the initial section of the lateral wall. In particular, the latter is considered up to the stagnation point, $\sim 14$ mm, chosen as representative length of the recircula-

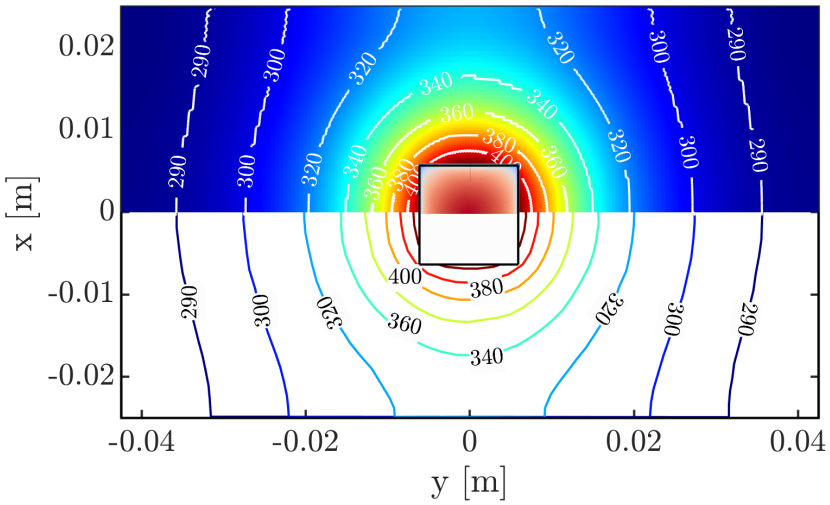


**Figure 5.18:** Temperature field in the solid domain at z = 0.255 m averaged over the evaluation time (top) and compared to [83] (bottom). Fluid domain is colored with the mean Favre-averaged temperature field. Color bars from Fig. 5.16.

tion region. It is possible to see that the temperature on the injection plate is almost constant, with a variation of $< 2\%$ between the maximum and minimum value, and that is of the same order of magnitude of the temperature on the lateral wall. The maximum temperature value in the recirculation region, in particular, shows a variation of $< 7\%$ with respect to the lowest temperature sampled in the chamber corner.

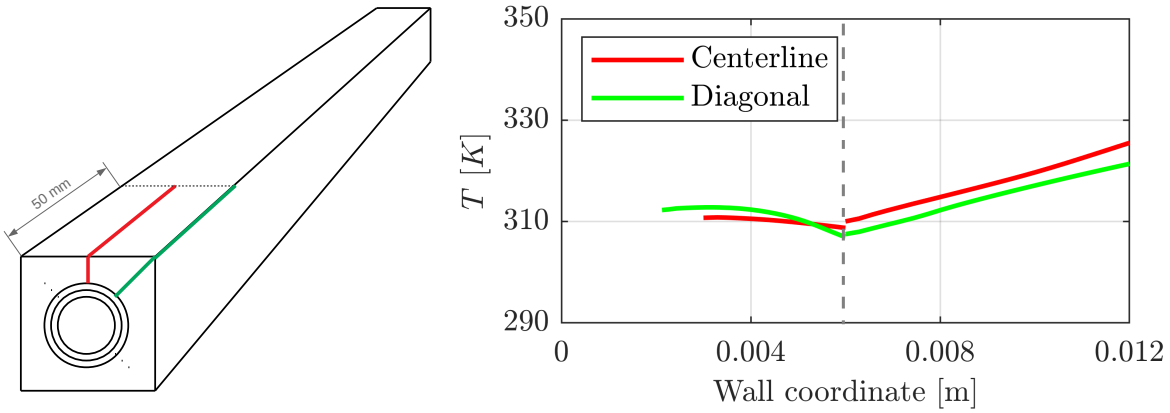


**Figure 5.19:** Temperature obtained on the injection plate and on the initial section of the lateral chamber wall. The wall coordinate used as abscissa is not aligned with any of the chamber axis but follows the directions highlighted in the left panel, the dashed line in the right panels divides the data collected on the plate (left side) from those collected on the combustor lateral wall (right side).

## 5.4 3D multi-injector combustion chamber

The numerical framework is finally applied to a multi-injector testcase, an experimental combustor developed at the Technical University of Munich featuring five aligned injection elements geometrically equal to the single-injector case seen before, and cooled also in this case with oxygen-free copper (Cu-HCP) walls. The load point considered is of 20 bar and $O/F = 3.4$, as indicated in the reference work by Perakis et al [83]. An initial solid temperature of 290 K is considered, consistently with what used for the single injector test case, but no data on the actual experimental case were found in the reference work [83]. The combustor is equipped with thermocouples located at several planes along the longitudinal direction, with a maximum of seven thermocouples per plane. Following the span-wise direction, the thermocouples are named 1C, 2C, 3L, 3C, 3R, 4C, 5C, with C indicating the sampling points above an injector element and L and R respectively the position on the left and on the right of the central injector.

### Grid choice

Being the combustor composed by five aligned injectors, identical to the previous single-element chamber, the employed numerical grid is derives from the already validated single-injector grid, replicated modularly for five times. The same solutions previously employed to have correspondence between faces of the finite volumes on the fluid-solid interface boundary and an average distance between neighbouring computational nodes of $\sim 0.5$ mm are employed in the solid domain. In this case the fluid domain is truncated at $z = 277$ mm, corresponding to the nozzle inlet of the reference experimental facility. The characteristics of the resulting grid are reported in Tab. 5.4.

| | No. Fluid finite volumes | No. Solid finite volumes |
|---|---|---|
| TUMrig 5-Inj | 4437760 | 9781440 |

**Table 5.4:** Characteristics of the numerical grid used for the 3D TUMrig multi-injector testcase.

### Results

Figure 5.20 shows $h_C$ converging to a steady state value after an initial transient for several control points at the thermocouples' location. By symmetry and for brevity, only half of the available points are displayed. Also in this case, $h_C$ is found to attain a statistical steady state value after $\sim 3$ flow-through times, the coupling strategy employing the Newton condition can thus be employed, allowing for the simulation of the complete experiment.
Figure 5.21 shows the temperature field in the solid domain at the end of 3 seconds of experimental run, the fluid domain is represented instead by instantaneous isosurfaces of mixture fraction coloured with temperature in the fluid domain. The temperature obtained at the interfaces are compared to the reference data from [83] in Fig. 5.22. The first thermocouple, located at $z = 0.0515$ m, is affected by the same overestimation already seen in the previous subsection, owing to the enforcement of the wall modeling. The farthest thermocouple reading, on the other hand, is significantly underestimated, on account of the proximity to the outlet section and to the adiabatic solid wall. The agreement between the reference data and the sampled results along

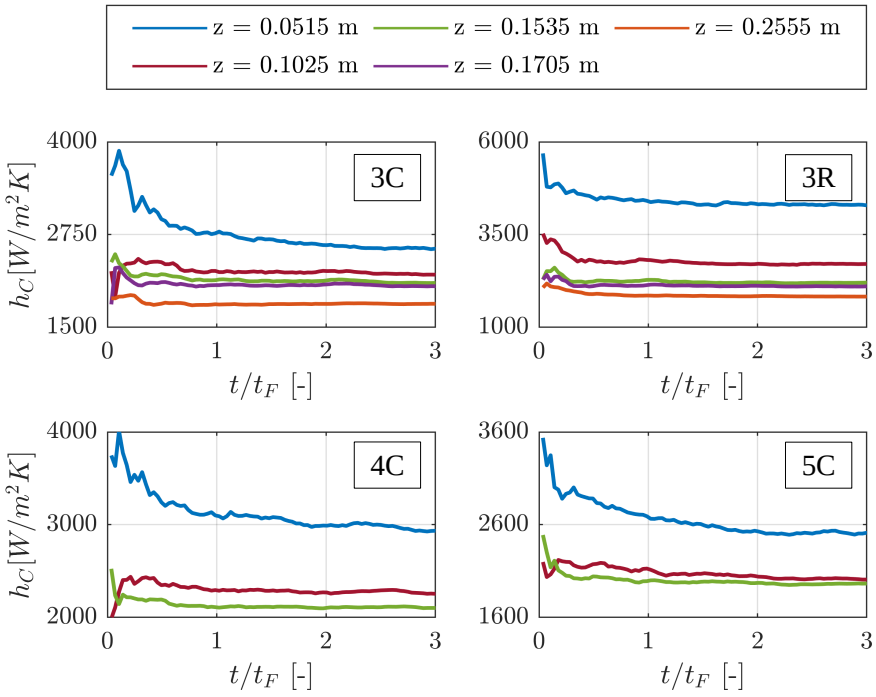


**Figure 5.20:** Attainment of a steady state value of the heat transfer coefficient $h_C$ in the multi-injector configuration.

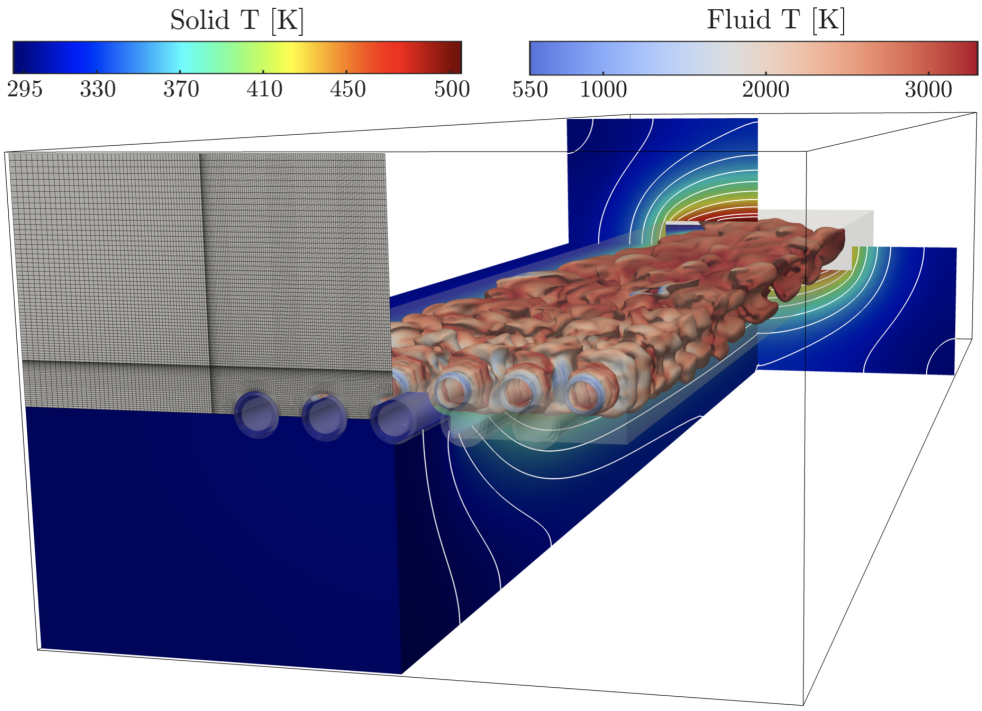


**Figure 5.21:** 3D multi injector with instantaneous isosurface of stoichiometric mixture fraction colored by temperature

the central combustor section is considered satisfactory, and within the uncertainties of the initial experimental conditions.

The temperature field averaged over the evaluation time (between 2 and 2.5 s) in the solid domain is shown in Fig. 5.23, together with a qualitative comparison with the data presented in [83].

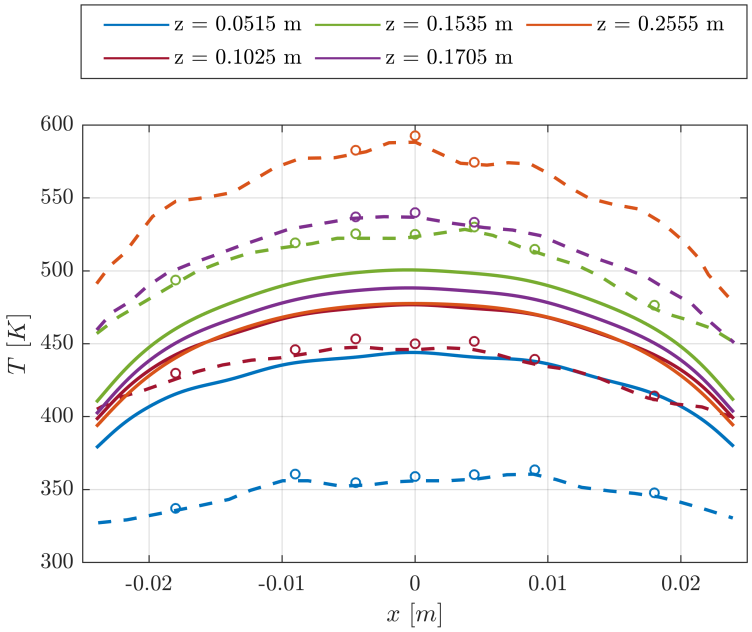


**Figure 5.22:** Interface temperature for several abscissa at the evaluation time, compared to Perakis inverse method and experimental data [83].

The section sampled at $z = 0.2725$ m in [83] has been compared here to a section sampled at $z = 0.230$ m, since a comparison performed on the same abscissa would have been excessively affected by the underestimation observed in proximity of the outlet. The main field features are well reproduced, any further difference in the presented results can be ascribed to a difference in the solid initial temperature leading to a comparison that should be therefore limited to the temperature field pattern. In the present case, in particular, an initial solid temperature of 290 K is considered, consistently with what used for the single injector test case, but no data on the actual experimental case were found in [83].

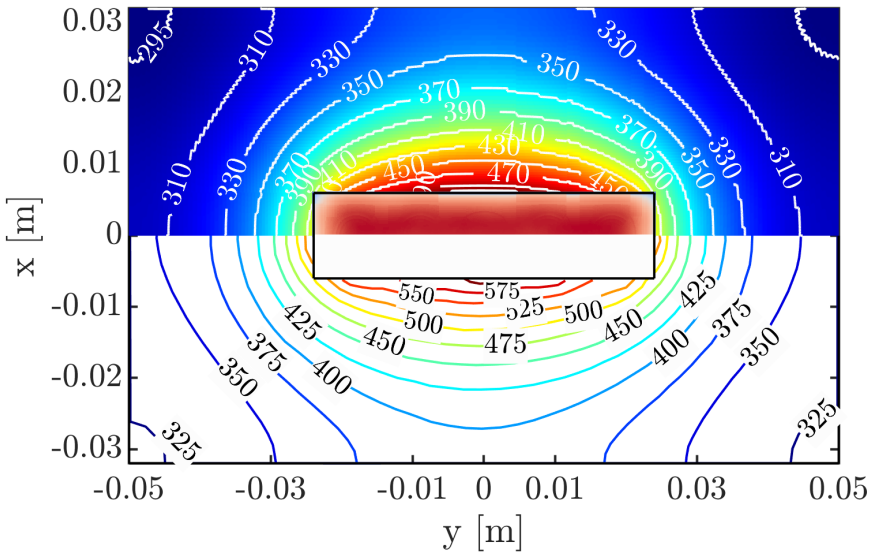


**Figure 5.23:** Temperature field in the solid domain averaged over the evaluation time (top) and qualitatively compared to [83] (bottom). Fluid domain is colored with the mean Favre-averaged temperature field. Color bars from Fig. (5.21).

# Chapter 6

# Single- and multi-region analysis of low-to-high Mach number flows

## Contents



## Nomenclature

**Latin letters**

| | |
|---|---|
| $h_C$ | = Heat transfer coefficient |
| $k$ | = Solid-fluid thermal conductivity ratio |
| $\dot{m}$ | = Inlet mass-flow |
| $\dot{m}_{\mathrm{nom}}$ | = Nominal inlet mass-flow |
| $O/F$ | = Oxidizer-to-fuel ratio |
| $p$ | = Pressure |
| $p_0$ | = Outlet pressure |
| $t$ | = Time |
| $t_F$ | = Flow-through time |
| $T$ | = Temperature |
| $u$ | = Velocity |
| $x$ | = Radial coordinate |
| $y$ | = Width coordinate |
| $z$ | = Longitudinal coordinate |

**Greek letters**

| | |
|---|---|
| $\Theta$ | = Non-dimensional temperature |
| $\lambda$ | = Thermal conductivity |
| $\rho$ | = Density |

**Subscripts and superscripts**

| | |
|---|---|
| $\square_{\mathrm{F}}$ | = Fuel value |
| $\square_{\mathrm{int}}$ | = Interface value |
| $\square_{\mathrm{Ox}}$ | = Oxidizer value |

The fidelity of the numerical framework, either single- or multi-region, seen in the previous Chapters, will be here increased accounting also for compressibility effects. The TUMrig experimental combustor [15] will be taken again as reference test case: in a first instance the analysis will be performed in a single-region setting, allowing for the validation of the solver and for the parametric investigation of the inlet mass-flow effect on the flow field and thermal load. Secondly the low-to-high Mach number flow will be coupled with the capacitively cooled system through the conjugate formulation in order to gain information on the thermal load in the nozzle region.

All the analyses are performed under a two-dimensional axis-symmetric approximation, resorting therefore to definitions of the equivalent radii used in the previous Chapters.

## 6.1 Introduction to the test case

The TUMrig combustor is in this Chapter simulated including the flow expansion in the nozzle. The latter is a converging-diverging nozzle with a contraction ratio of 2.5. It must be noted that the TUMrig facility is a square-section chamber, but the nozzle throat in the original configuration is rectangular. The equivalent throat radius used for the two-dimensional configuration has been defined maintaining the contraction ratio of the real test case, all the characteristic dimensions of the two-dimensional setup are given in Fig. 6.1. The load point considered corresponds to a pressure of 20 bar and an O/F = 2.6, as in the reference work by Celano et al. [15]. The flamelet tables for this testcase have been generated following the approach described in Sec. 2.1.3, covering a range of pressures from 0.2 to 25 bar. All the other tables parameters are consistent with the low-Mach tables used in the previous Chapters.

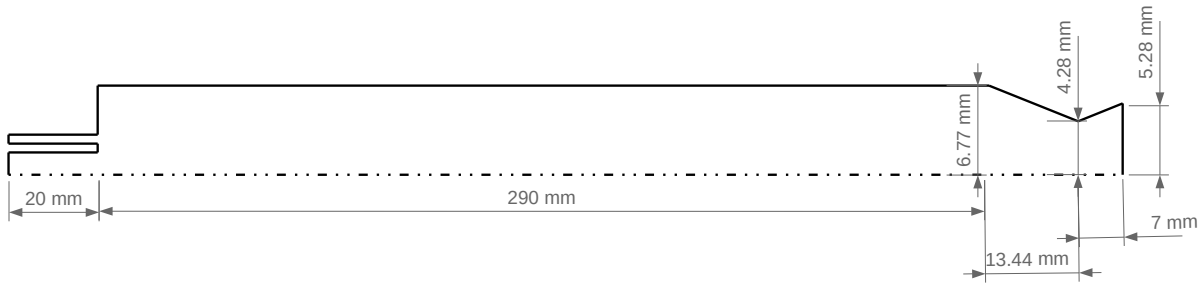


**Figure 6.1:** Geometry and configuration of the TUMrig 2D in a single-region setting with the compressible formulation.

### 6.1.1 Grid assessment study

An extensive grid convergence analysis has been performed comparing the results obtained on three different numerical meshes, the characteristics of which are reported in Tab. 6.1. The labels indicated in the Table will be used in the following Figures and are numbered in order of increasing refinement, the letter P refers to the pressure-dependent formulation used while SR stands for Single Region.

| | No. Finite volumes |
|---|---|
| TUMrig P-SR-1 | $6.3 \cdot 10^3$ |
| TUMrig P-SR-2 | $25.5 \cdot 10^3$ |
| TUMrig P-SR-3 | $101.8 \cdot 10^3$ |

**Table 6.1:** Numerical grids used for the grid convergence analysis of the 2D TUMrig combustor with the compressible formulation.

Following what done in Chap. 4, Fig. 6.2 shows the results obtained on the three mentioned grids in terms of wall heat flux and pressure on the lateral wall and density and mixture fraction along the longitudinal axis. Note that in the present case, mixture fraction and temperature data are

available also inside the nozzle, from Fig. 6.2d in particular, it is observable the temperature drop in the divergent section of the nozzle. The results obtained with the grids are considered satisfactorily close to each other, the intermediate mesh TUMrig P-SR-2 is therefore taken as reference numerical grid for the parametric analysis of the inlet mass-flow effect, guaranteeing accurate results with a limited computational costs as it is convenient in view of the database collection.

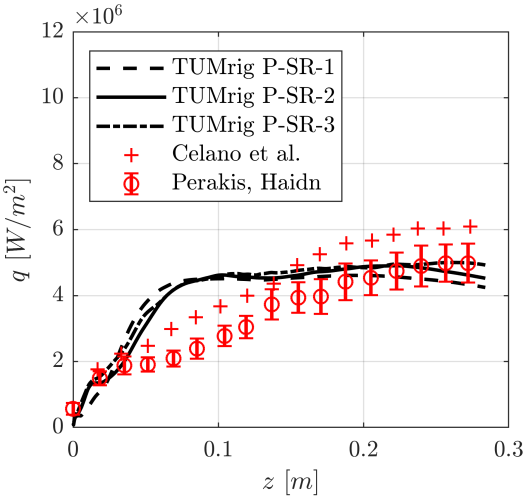


(**a**) Time-averaged wall heat flux on the chamber wall compared to experimental and literature data.

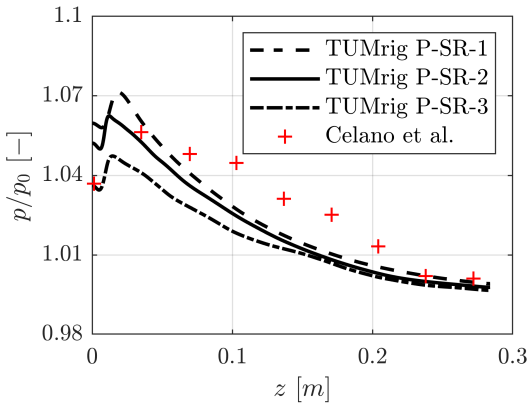


(**b**) Time-averaged normalized pressure on the chamber wall compared to experimental data.

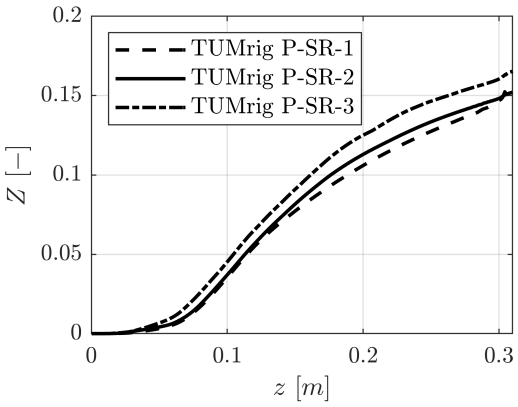


(**c**) Time-averaged mixture fraction on the chamber axis.

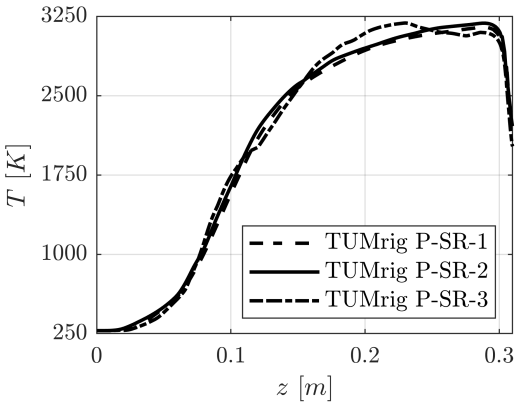


(**d**) Time-averaged temperature on the chamber axis.

**Figure 6.2:** Grid convergence assessment for the wall-bounded configuration analyzed resorting to the compressible formulation.

## 6.2 Mass-flow effect

Being the compressible solver completely predictive on the pressure field, it represent an ideal tool for the parametric analysis of the injection condition. The inlet mass-flow has been therefore varied within a range of interest, by a proportional variation of the propellants inlet velocities, aimed at maintaining the nominal O/F. All the geometrical dimensions of the configuration are kept fixed, likewise the other thermodynamic injection conditions. Since no experimental data are available on the nozzle region, the converging-diverging walls have been considered, in a first instance, adiabatic.

Table 6.2 reports all the simulations performed, along with their labels: M indicates the mass-flow, followed by some numbers representing the mass-flow normalized to the nominal case (e.g. M-0p80 stands for 0.80 times the nominal mass-flow). The same table also reports the corresponding velocities for fuel and oxidizer.

| | $\dot{m}/\dot{m}_{\mathrm{nom}}$ | $u_{\mathrm{F}}$ [m/s] | $u_{\mathrm{Ox}}$ [m/s] |
|---|---|---|---|
| M-0p80 | 0.80 | 109.73 | 103.47 |
| M-0p90 | 0.90 | 123.44 | 116.39 |
| M-1p00 | 1.00 | 137.16 | 129.32 |
| M-1p10 | 1.10 | 150.88 | 142.25 |
| M-1p20 | 1.20 | 164.59 | 155.18 |

**Table 6.2:** Labels of the simulations carried out for the parametric analysis and corresponding mass-flows and injection velocities.

As it can be expected, the mechanical load over the combustor walls increases with increasing inlet mass-flows, the effect is reported in Fig. 6.3 in terms of pressure.

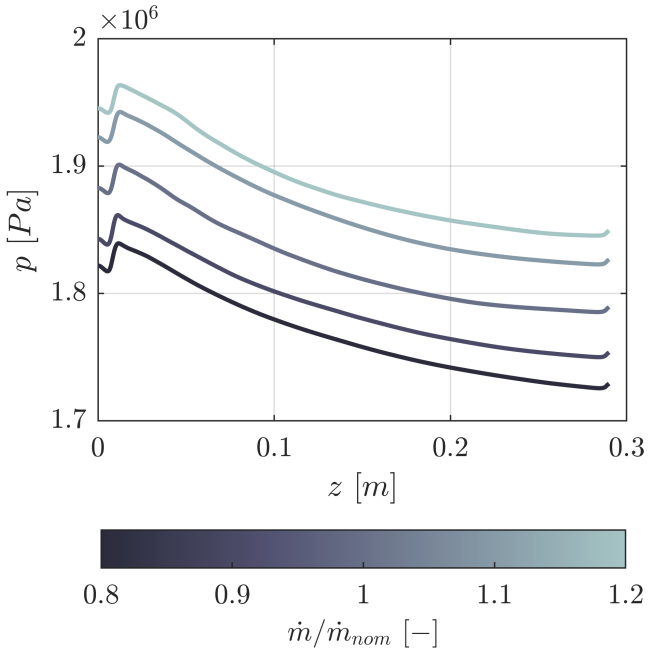


**Figure 6.3:** Inlet mass-flow effect on chamber wall pressure.

To the higher pressure follows an higher density of the reacting mixture, reported in Fig. 6.4 by means of the data extracted along the first third of the longitudinal axis, where the effect is more visible. The density increase is more prominent for the mass-flows higher than the nominal value, while for M-0p80 and M-0p90 the density evolution remains closer to the nominal case. The density fields are shown in Fig. 6.5, where it can be observed the higher density in correspondence of the higher inlet mass-flows (lower panels), with the subsequent more elongated dense central oxidizer core.

Also the heat flux over the chamber wall increases with increasing inlet mass-flows, as shown in Fig. 6.6. It is in fact known that the near-wall temperature increases with pressure (cfr. the effect of pressure in the flamelet libraries, Fig. 2.3 and [10]), leading therefore to higher thermal load.

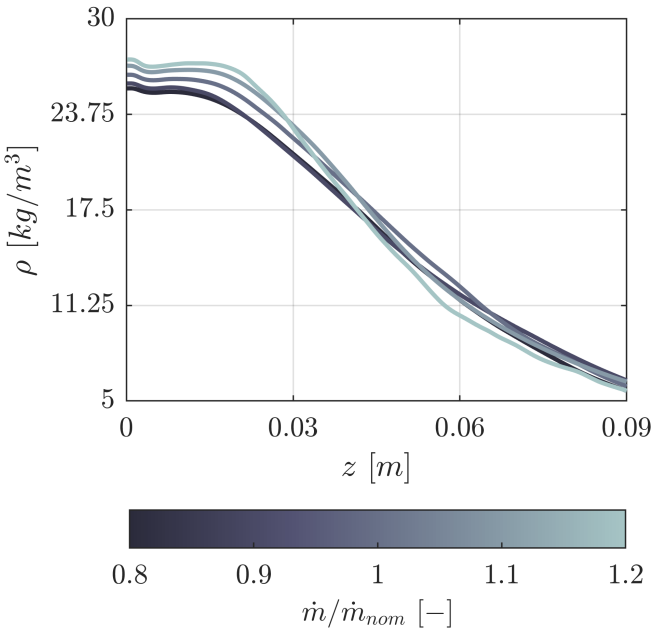


**Figure 6.4:** Inlet mass-flow effect on density along the chamber axis.

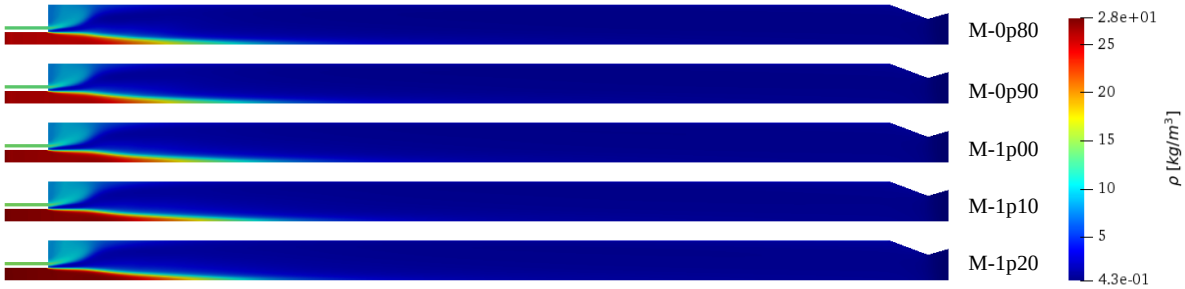


**Figure 6.5:** Density fields for several mass-flows. Axes not to scale.

Figure 6.7 shows the pressure and heat flux trends with the inlet mass-flows, together with the respective fitting power laws. Both the quantities are found to be increasing with the mass-flow, a similar trend for pressure was observed in [54], although with a steeper slope (mass-flow to the power of $\sim 0.9$) due to the different configuration and setting.

Figure 6.8 shows instead the surface-averaged heat flux value as function of the corresponding surface-averaged pressure on the chamber wall. It is found that the heat flux scales with a coefficient of the power law of $\sim 1.31$. Similar near-unity increasing trends were observed for different configurations in [119, 120], where the heat flux was found to scale with the chamber pressure to the power of $\sim 0.85$.

The temperature fields for the various cases in the dataset are shown in Fig. 6.9, with the superimposition of an isoline of stoichiometric mixture fraction $Z = 0.2$. It is possible to observe that for increasing mass-flows the flame is pushed towards the chamber lateral wall, resulting in the higher temperature field that motivates the higher heat flux already observed in Fig. 6.6. Moreover,

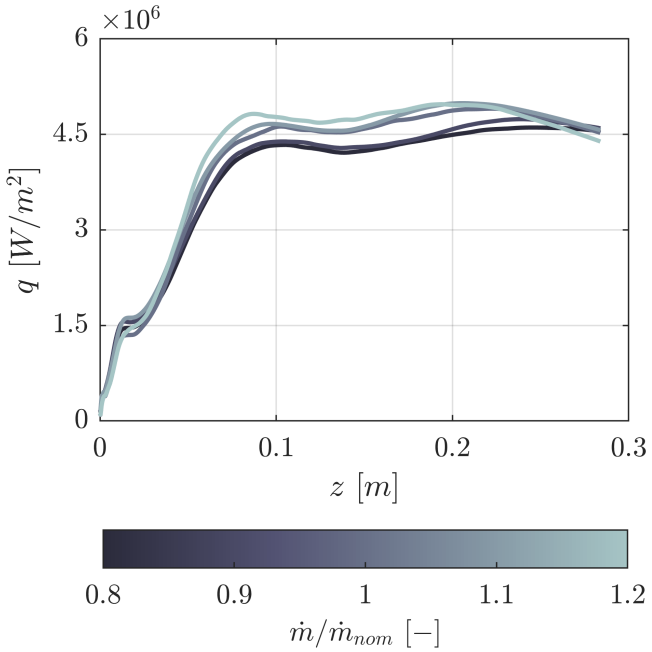


**Figure 6.6:** Inlet mass-flow effect on chamber wall heat flux.

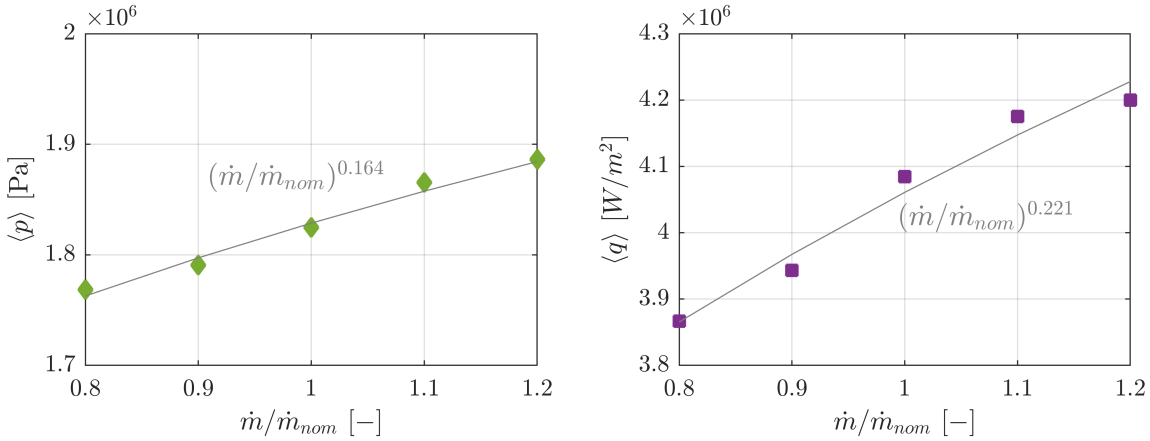


**Figure 6.7:** Surface-averaged values of pressure (left) and heat flux (right) for the varying mass-flows.

the higher velocities cause the flame to develop more smoothly for the higher mass-flows cases, while for lower mass-flows it is observed a more abrupt flame expansion in the initial section of the combustor. The same conclusions can be drawn for the recirculation regions, identifiable with the blue region in Fig. 6.9, which are more elongated for the configuration characterized by high mass-flows and vice-versa.

## 6.3 Coupled combustion chamber modeling

The compressible formulation has been then embedded in the multi-region solvers, aiming at the development of a comprehensive tool capable of modeling the combustion chamber from the injection to the nozzle expansion, together with the cooling system. The setup of the boundary condition for the coupled simulation retrace what done in Sec. 5.2, with the coupled interface condition

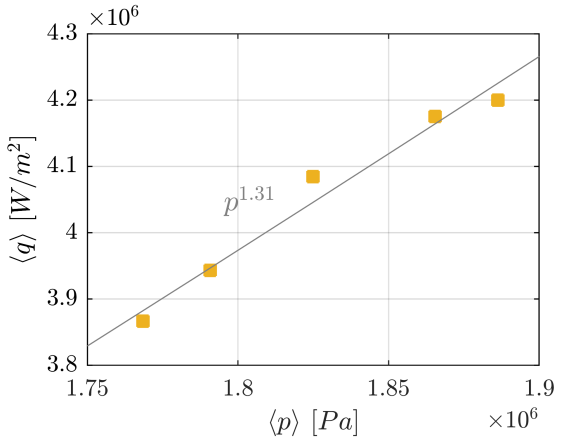


**Figure 6.8:** Surface-averaged values of heat flux as function of the corresponding surface-averaged pressure.

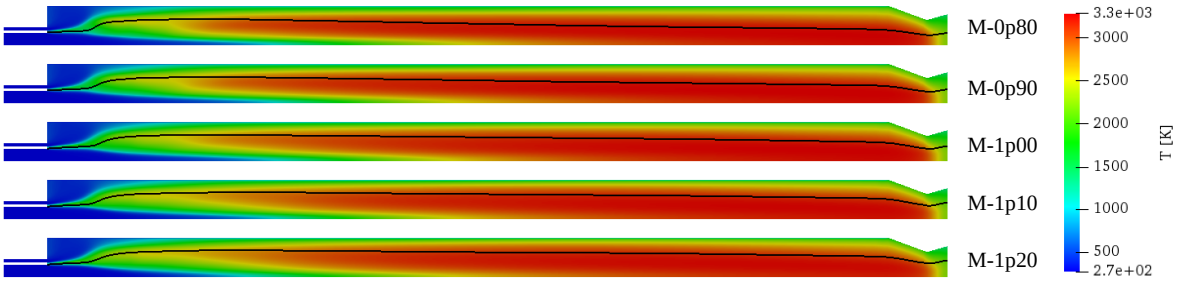


**Figure 6.9:** Temperature fields for several mass-flows, with superimposed isoline of stoichiometric mixture fraction $Z_{st} = 0.2$. Axes not to scale.

applied to the firing plate, the nozzle and the combustor lateral wall, the natural convection condition enforced over the solid external wall and all the other wall considered adiabatic. The initial temperature in the solid domain is also in this case equal to $T_{\text{solid}} = 290$ K. The entire duration of the experimental run has been modeled.

### Grid assessment study

The grid independence of the results has been assessed comparing the temperatures obtained on three different grids, obtained recursively doubling the number of points in each direction. Table 6.3 reports the main grid characteristics, following the nomenclature of the previous Section, the letter P in the labels refers to the compressible formulation, MR stands for Multi-Region, while the numbers are given in increasing order of refinement.

| | No. Fluid finite volumes | No. Solid finite volumes |
|---|---|---|
| TUMrig P-MR-1 | 6365 | 6757 |
| TUMrig P-MR-2 | 25460 | 27028 |
| TUMrig P-MR-3 | 101840 | 108112 |

**Table 6.3:** Numerical grids used for the convergence analysis of the coupled 2D TUMrig testcase with the compressible formulation.

Figure 6.10 shows the interface temperature obtained on the lateral wall at a given time instant

(upper-left panel), together with the temperature evolution in time for three abscissas respectively representing the injection region, the central section of the chamber and the area close to the nozzle. In particular, the temporal coordinate has been normalized with respect to the flow-through time of the configuration. Note that, due to the elevated computational cost of the finest grid TUMrig P-3, the corresponding simulation has been initialized from a later time instant with a field mapped from the TUMrig P-2 case. It can be observed the achievement of an asymptotic convergence of the results, therefore the intermediate grid TUMrig P-2 is chosen as reference.

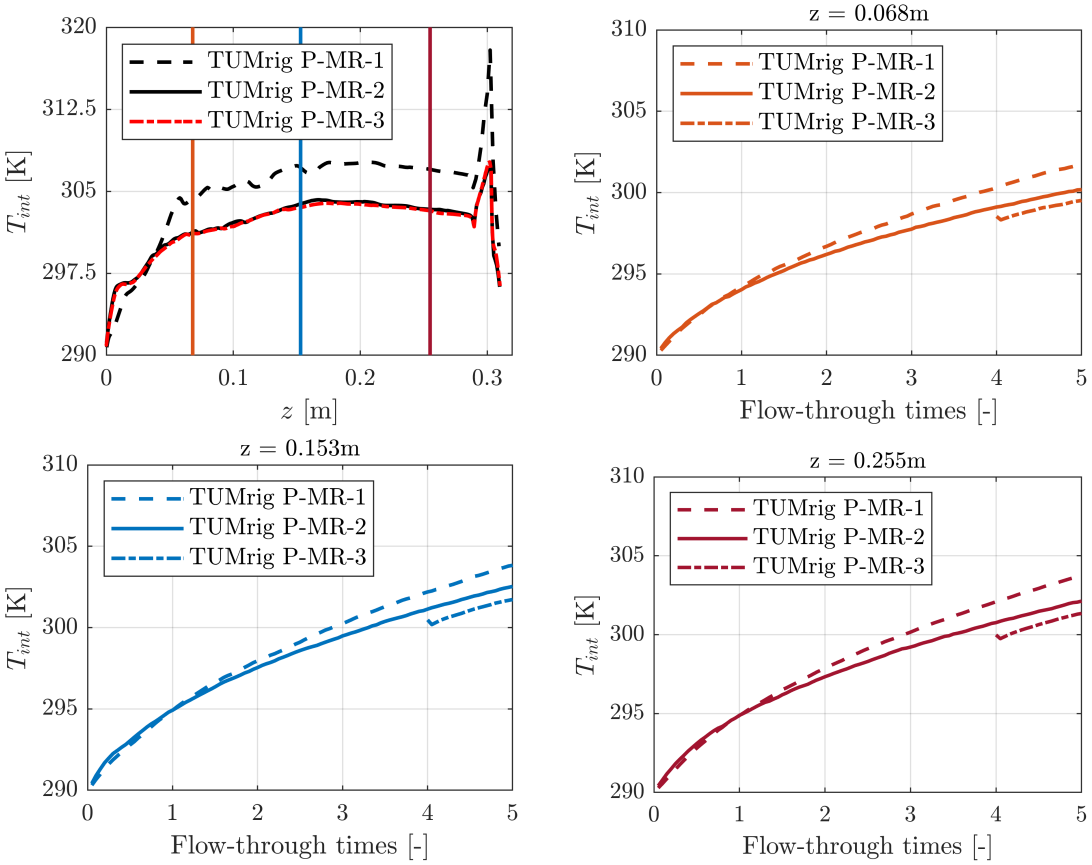


**Figure 6.10:** Grid convergence: chamber wall and nozzle interface temperature at given time (upper left panel) and temperature evolution in time for several grids.

### Results

The time convergence of the heat transfer coefficient $h_C$ is shown in Fig. 6.11 for the lateral wall and nozzle. The same analysis has been also performed for the injection plate. The right panel of Fig. 6.11 reports the temporal evolution of the coefficient, it is observed that a statistical steady state value of $h_C$ is attained after $\sim 3-5$ flow-through times, confirming what previously found for the same configuration under low-Mach number assumption in Chap. 5. The left panel of Fig. 6.11 reports instead the coefficient profile over the entire wall for different time instants, to highlight how the coefficient values progressively collapse on the statistical steady state profile. Such profile will be then fed into the Newton boundary condition in order to proceed the simulation with the solution of the solid conduction problem.

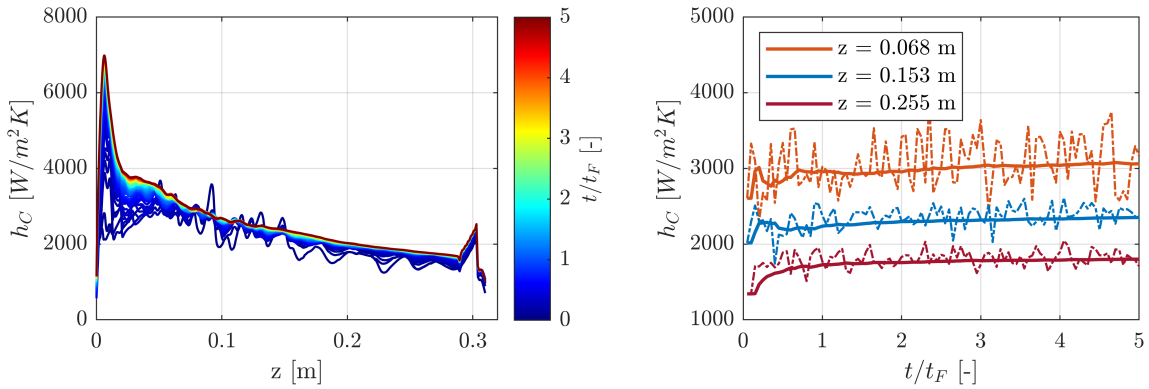


**Figure 6.11:** Convergence of the heat transfer coefficient to a steady value on the combustion chamber lateral wall and nozzle. In the right panel dashed lines represent instantaneous values, solid lines represent time-averaged values.

The temperature fields in the coupled domains at the end of the experimental time are shown in Fig. 6.12, it is possible to note the solid heating in correspondence of the nozzle section, a phenomenon which was not captured by the low-Mach formulation discussed in the previous Chapter.

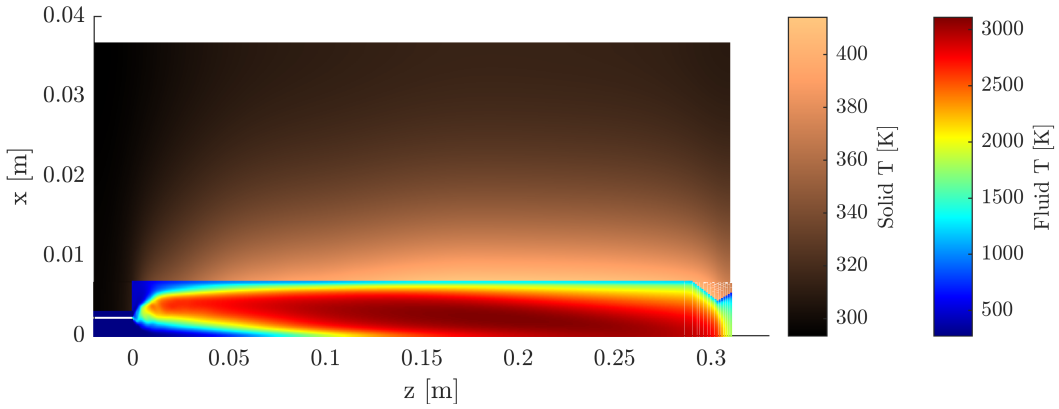


**Figure 6.12:** Temperature fields in the fluid and solid domains at the end of the experimental run. Axes not to scale.

The comparison with the experimental data is shown in Fig. 6.13 and 6.14 respectively in terms of pressure and heat flux over the combustor lateral wall and nozzle. Both the fields have been averaged over the evaluation time, i.e. the time-window comprised between 2 and 2.5 seconds. The pressure field has been compared to the experimental data and to the reference data provided by a number of groups in the Rocket community and collected by Roth et al. in [103]. The nomenclature used in [103] has been maintained in Fig. 6.13. Concerning the heat flux, the comparative experimental data are available only in correspondence of the lateral wall, since no experimental probes are present in the nozzle region. The agreement with the reference data is considered satisfactory.

In addition to the experimental data, Fig. 6.14 shows the comparison between all the wall heat fluxes obtained on the two-dimensional TUMrig configuration with the several approaches discussed throughout this work, under equal load point considered and resorting to numerical grids of comparable sizes. SR and MR in the legend refer respectively to the single-region or multi-region approaches, while the second part of the label refers to the presence or absence of the low-Mach

number hypothesis. A summary of the nomenclature and of the modeling assumptions enforced is provided in Tab. 6.4. The comparison between SR-low Mach and MR-low Mach has been already commented in Sec. 5.2, it is now noteworthy the fidelity improvement brought by both the simulations featuring the compressible formulation. The results of the coupled simulation are quite close to those of the single-region setting, but present a better approximation of the experimental data in the first half of the chamber.

| Label | Coupled interface | Compressibility effects |
|---|---|---|
| SR - low Mach | - | - |
| MR - low Mach | ✓ | - |
| SR - compressible | - | ✓ |
| MR - compressible | ✓ | ✓ |

**Table 6.4:** Summary of the modeling approaches applied to the TUMrig combustor throughout the thesis, under equal two-dimensional approximation and reference load point.

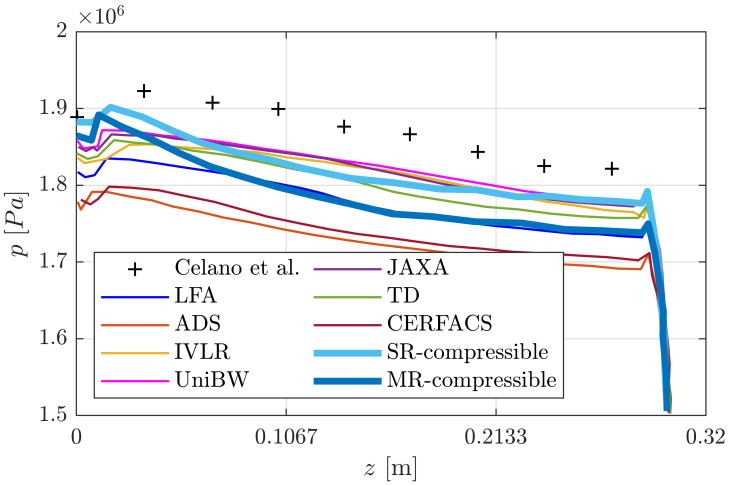


**Figure 6.13:** Pressure over the combustor lateral wall and nozzle converging-diverging walls averaged in the evaluation time and compared to the experimental data.

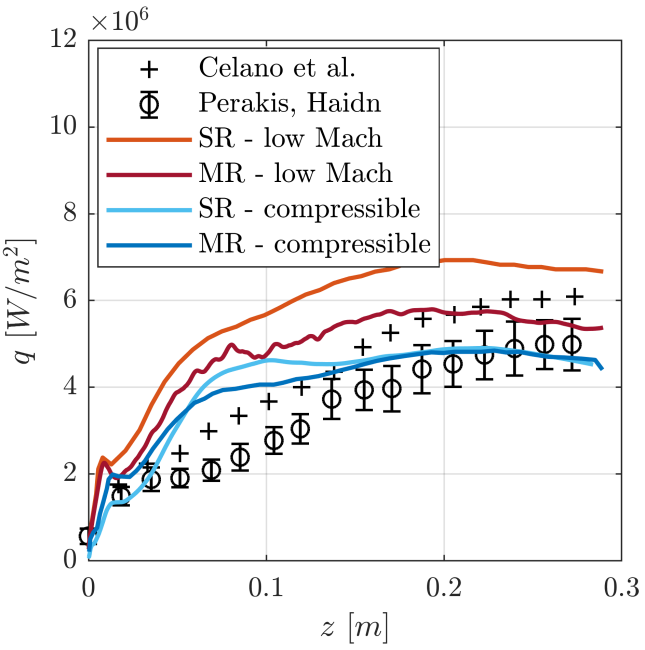


**Figure 6.14:** Heat flux over the combustor lateral wall averaged in the evaluation time and compared to the experimental data (markers) and to the results obtained on the same configuration with different modeling approaches (solid lines). Cfr. Tab. 6.4 for the full nomenclature.

# Chapter 7

# Towards the modeling of premixed hydrogen-air injection

## Contents



## Nomenclature

**Latin letters**

| | |
|---|---|
| $C$ | = Progress variable |
| $D$ | = Diffusivity |
| $\ell_T$ | = Laminar flame thickness |
| $L_x$ | = Cross-wise dimension |
| $L_y$ | = Stream-wise dimension |
| $p$ | = Pressure |
| $S_c$ | = Consumption speed |
| $S_L$ | = Laminar flame speed |
| $t$ | = Time |
| $T$ | = Temperature |
| $u$ | = Velocity |
| $Y$ | = Mass fraction |
| $Z$ | = Mixture fraction |

**Greek letters**

| | |
|---|---|
| $\Delta$ | = Filter size |
| $\Theta$ | = Non-dimensional temperature |
| $\rho$ | = Density |
| $\phi$ | = Equivalence ratio |
| $\psi$ | = Generic quantity |
| $\dot{\omega}$ | = Production term |

**Operators**

| | |
|---|---|
| $\widetilde{\cdot}$ | = Spatial filter |
| $\overline{\cdot}$ | = Density-weighted filter |

**Subscripts and superscripts**

| | |
|---|---|
| $\square_{ad}$ | = Adiabatic value |
| $\square_u$ | = Unburned value |

This Chapter is devoted to the numerical modeling of premixed hydrogen-air combustion. Among the plethora of high energy density devices, hydrogen premixed combustion will find its major applications in gas turbines for electricity production and in industrial or household burners, as well as in aeronautical applications. The numerical modeling of high pressure hydrogen

premixed combustion is indeed not lacking in challenges, and can be efficiently tackled with some stiffness-reduction techniques akin to those discussed in the previous Chapters. More specifically the application of a tabulated chemistry approach is discussed in the following, together with its a-priori validation.

## 7.1 Peculiarities of hydrogen combustion

Hydrogen combustion has recently regained attention due to its sustainability characteristics, but raises considerable challenges from both the experimental and numerical standpoints. Hydrogen operating conditions are usually leaner compared to the conventional fuels, thanks to the higher reactivity, but are, on the other hand, also characterized by higher flames temperatures and laminar flame speeds. Moreover, the high mobility of the hydrogen molecule causes the effective mixture Lewis number to decrease the sub-unity values.
The latter effect is particularly crucial for lean mixtures, which are prone to combustion instabilities when the Lewis number decreases below a sub-unity critical value [75]. Under these conditions a planar flame cannot exist since small-scale perturbation are amplified leading to the formation on self-wrinkled unstable cellular structures [74]. These are caused by the local perturbations of the flame speed as a consequence to the local unbalance between the thermal conductivity of the mixture and the molecular diffusivity of the controlling reactant, with a mechanism known as thermo-diffuisve instability. In addition, these corrugations are enhanced by the interaction with the hydrodynamic (or Darrieus-Landau) instabilities, which are active at all wavelengths and cause the further corrugation of the flame front as a consequence of the thermal expansion [8, 22, 56]. The interaction of these instabilities leads to an highly non-linear mechanisms, requiring dedicated modeling.
When approaching to large-scale computational domains, it is necessary to decrease the fidelity level of the numerical approach. In order to do so, it is usual to resort to models of the turbulence–chemistry interaction, which besides representing the main features of such interaction, must also retain information about the main physical characteristics of the phenomena falling at the subgrid level. The multi-scale self-wrinkling of thermal-diffusively unstable flames, for instance, are among these since for the smallest scales can be of the order of the flame thickness. Figure 7.1 shows the typical cellular structures of a thermal-diffusively unstable flame, the comparison with the superimposed paradigmatic LES grid with filter size $\Delta$ demonstrates how the small-scale wrinkles fall under the subgrid level.
The model discussed in this Chapter and deepened in the following Section is based on lower dimension manifold representation, by means of a tabulated approach.

## 7.2 Data-driven model

The interaction between the thermo-diffusive and hydrodynamic instabilities is intrinsically characteristic of the lean hydrogen mixtures, the proposed manifold representation aims at providing a lower-order modeling representative of these interactions and will therefore focus on the sole modeling of the laminar self-wrinkling flame neglecting in a first stage the contribution of turbulence. The approach stems from the F-TACLES [28] method, retaining from the latter the filtered tabu-

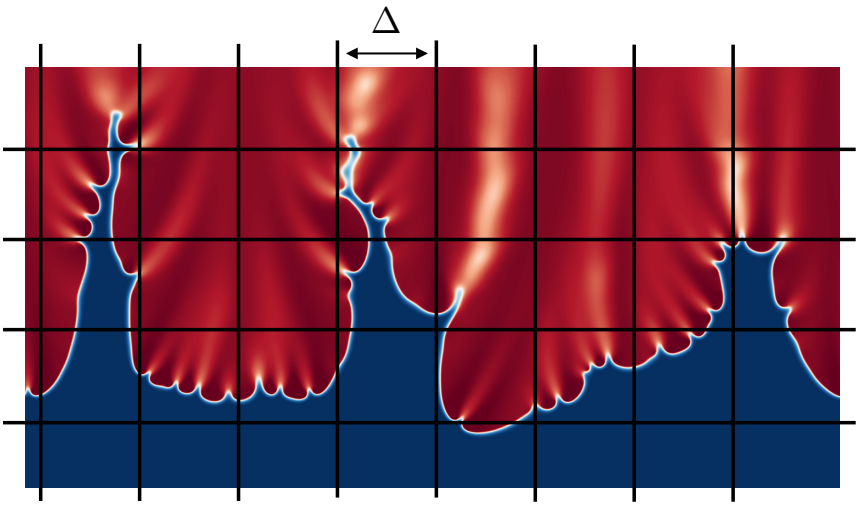


**Figure 7.1:** Self-wrinkled cellular structures in a hydrogen unstable flame with superimposed grid of a generic LES. Image taken from [57].

lated chemistry structure but utilizing a fully resolved, two-dimensional, unstable, self-wrinkling flame as source for the filtering procedure. When dealing with intrinsically unsteady flames it must be indeed considered a multi-dimensional paradigmatic structure, and the assumption that the flame structure can be assumed identical to the one-dimensional unstretched freely propagating premixed laminar flame fails [56]. In this case, a database two-dimensional flames has been chosen as blueprint of the model, since it has been shown that two-dimensional flames subject to hydrodynamic instabilities present most of the morphological features of the corresponding three-dimensional large-scale flames [64].

### 7.2.1 DNS dataset

The two-dimensional flames used in this work belongs to the DNS multi-step chemistry hydrogen/air dataset developed by Berger et al. [8], consisting in statistically planar premixed flames in rectangular computational domains periodic in the cross-wise direction. In particular, two DNS from the database will be considered in the following: a large-scale DNS, with a cross-wise dimension $L_x = 800\ell_T$, $\ell_T$ being the laminar flame thickness of a one-dimensional unstretched flame, and a small-scale flame with $L_x = 50\ell_T$. The stream-wise dimension of both the DNS is $L_y = 200\ell_T$, the unburned mixture features in both cases an equivalence ratio of $\phi = 0.4$, an uburned temperature of $T_u = 298$ K and a pressure of $p = 1$ bar. Two realizations of the mentioned DNS are shown in Fig. 7.2 and 7.3, respectively in terms of non-dimensional temperature $\Theta$ and production term of the controlling reactant $\dot{\omega}_{H2}$. The former in particular is defined as follows:

$$\Theta = \frac{T - T_u}{T_{\text{ad}} - T_u} \tag{7.1}$$

with $T_{\text{ad}} = 1536$ K the adiabatic flame temperature.
The flow is modeled solving the reacting Navier-Stokes equations in the low-Mach number limit [114] under the assumption of ideal gas. Species diffusivities are determined imposing spatially homogeneous, non-unity Lewis numbers, taken in the burnt gas region of one-dimensional unstretched premixed flames [8]. The Soret effect is included, being particularly relevant for hydro-

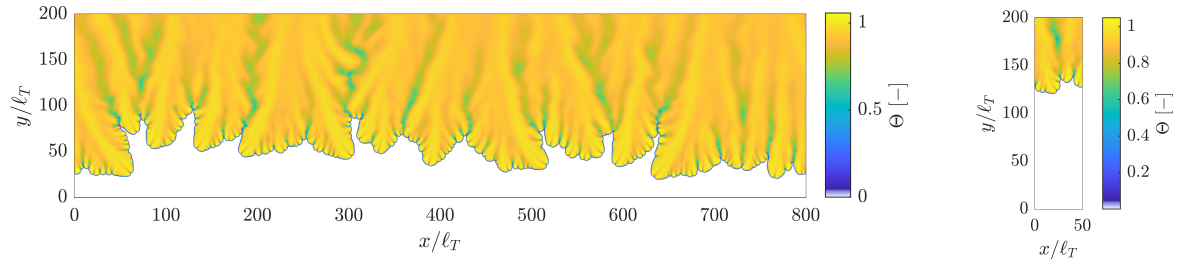


**Figure 7.2:** Non-dimensional temperature in the reference multi-step chemistry DNS. Left panel: large-scale DNS $L_x = 800l_D$, right panel: small-scale DNS $L_x = 50l_D$

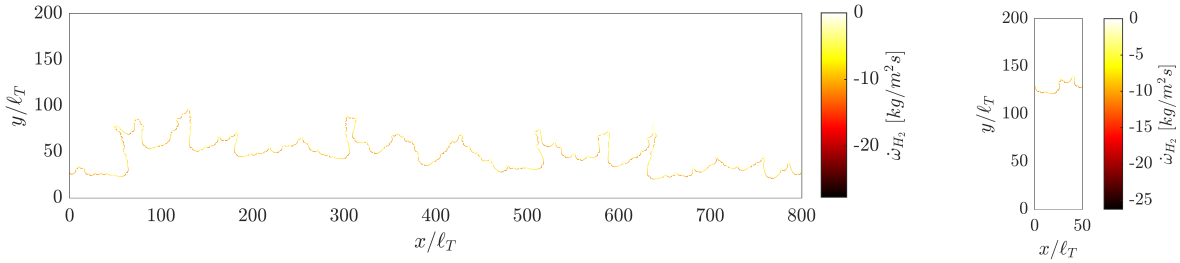


**Figure 7.3:** $H_2$ production term in the reference multi-step chemistry DNS. Left panel: large-scale DNS $L_x = 800l_D$, right panel: small-scale DNS $L_x = 50l_D$

gen flames [127]. The reaction mechanism of Burke [13] containing 9 species and 46 reaction is chosen for the chemical reactions modeling. A semi-implicit finite difference code based on the Crank–Nicolson time advancement scheme, an iterative predictor corrector scheme, and spatial and temporal staggering is employed [34]. Momentum equations are spatially discretised with a second-order scheme. Species and temperature equations are discretised with a third-order WENO scheme [42] and advanced by utilising Strang's operator splitting [112]. The mesh resolution and times-tep size are chosen such that the laminar flame speed, heat release, temperature, and species profiles of a one-dimensional premixed unstretched flame computed by FlameMaster [89] are recovered adequately yielding a time-step size of 6 $\mu s$ and a spatial resolution of ten grid points in the thermal flame thickness defined by the maximum gradient of temperature.
The objective of the model is to represent the characteristic pattern of the large-scale field utilizing tables obtained filtering the small-scale DNS. It has been demonstrated in [56] that in order for the filtered tabulated model to reproduce large-scale flames, the small-scale flame used for building the tables must feature at least one of the characteristic structure of the target flame. The small scale DNS chosen in this work is found to have the smallest domain width $L_x$ for which a finger-like structure is formed, as shown in [8].

### 7.2.2 Two-scalars manifold

It has been shown, by Regele et al [101] and Lapenna et al [56] among others, that lean premixed hydrogen flames are well approximated by manifolds not smaller than two-dimensional. More specifically, in the first work the two parameters chosen for the manifold parametrization are the non-dimensional temperature $\Theta$ and the mixture fraction $Z$, while in the latter is proposed a manifold function of the non-dimensional temperature and of the mass fraction of the deficient reactant

$Y_{H_2}$. Being lean premixed hydrogen flames prone to thermo-diffusive instabilities, strong fluctuations of the heat release rate are observed across the flame front, i.e. for constant values of the non-dimensional temperature, and an additional parameter is therefore needed to account for this effect. In this work, a manifold parametrization as function of two species mass fraction, namely $Y_{H_2}$ and $Y_{H_2O}$, is proposed.

## 7.3 Filtered tabulated chemistry

The set of governing equations comprises two transport equations for the mass fractions of the species chosen as manifold parameters, i.e. molecular hydrogen $H_2$ and water $H_2O$. The two concentrations can be normalized to the respective unburned value, obtaining the following equations:

$$\frac{\partial}{\partial t}\left(\rho C_{1,2}\right) + \nabla \cdot \left(\rho u C_{1,2}\right) = \nabla \cdot \left(\rho D_{1,2} \nabla C_{1,2}\right) + \dot{\omega}_{C_{1,2}} \tag{7.2}$$

where $C_1$ and $C_2$ are the progress variables based on the normalized concentrations of the chosen species. By filtering Eq. 7.2 it is obtained:

$$\frac{\partial}{\partial t}\left(\overline{\rho}\widetilde{C}_{1,2}\right) + \nabla \cdot \left(\overline{\rho}\widetilde{u}\widetilde{C}_{1,2}\right) = \nabla \cdot \left(\overline{\rho D_{1,2} \nabla C_{1,2}}\right) - \nabla \cdot \left(\widetilde{\overline{\rho u C_{1,2}}} - \overline{\rho}\widetilde{u}\widetilde{C}_{1,2}\right) + \overline{\dot{\omega}_{C_{1,2}}} \tag{7.3}$$

where $\bar{\cdot}$ and $\widetilde{\cdot}$ respectively represent the spatial filtering and the density-weighted filtering operation. Figure 7.4 shows the production term of the controlling reactant $H_2$ from the small-scale DNS spatially filtered with a Gaussian filter and variable filter sizes ranging from 1 to 20 $\ell_T$, representative of as many different LES grid sizes.

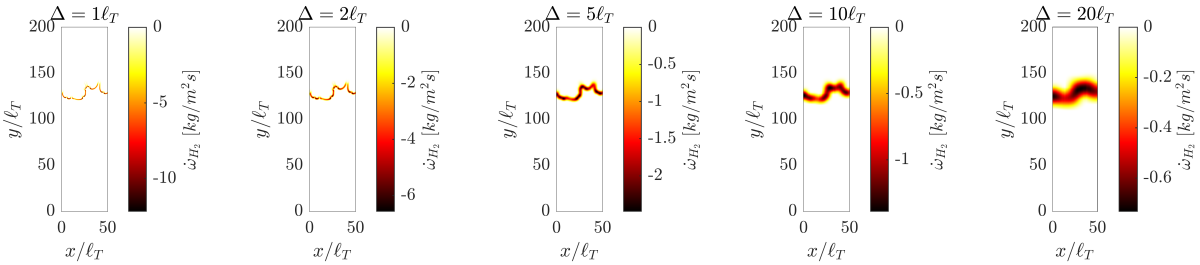


**Figure 7.4:** $H_2$ production term in the small scale filtered DNS for several filter sizes. Colormaps not uniform.

Note that the colormaps used in the subfigures are not uniformed with each other in order to ease the visibility. When increasing the filter size, in fact, the peak value of the corresponding production term decreases, and it wouldn't have been possible to appreciate the gradients across the filtered flame front using a unique colormap for all the filtered fields.
The tabulated manifold is obtained calculating for each thermochemical quantity and unclosed term in Eq. 7.3 the conditional average with respect to the two parameters from the filtered DNS database, that is, for the generic quantity $\psi$:

$$\psi = \langle \widetilde{\psi} | \widetilde{C_1}, \widetilde{C_2} \rangle \tag{7.4}$$

Figure 7.5 shows the tabulated manifold of the molecular hydrogen production rate, with the two scalars $\widetilde{C_1}$ and $\widetilde{C_2}$ as table coordinates for the several filter sizes considered. Also in this case, the

colormaps of the subfigures are not uniformed.

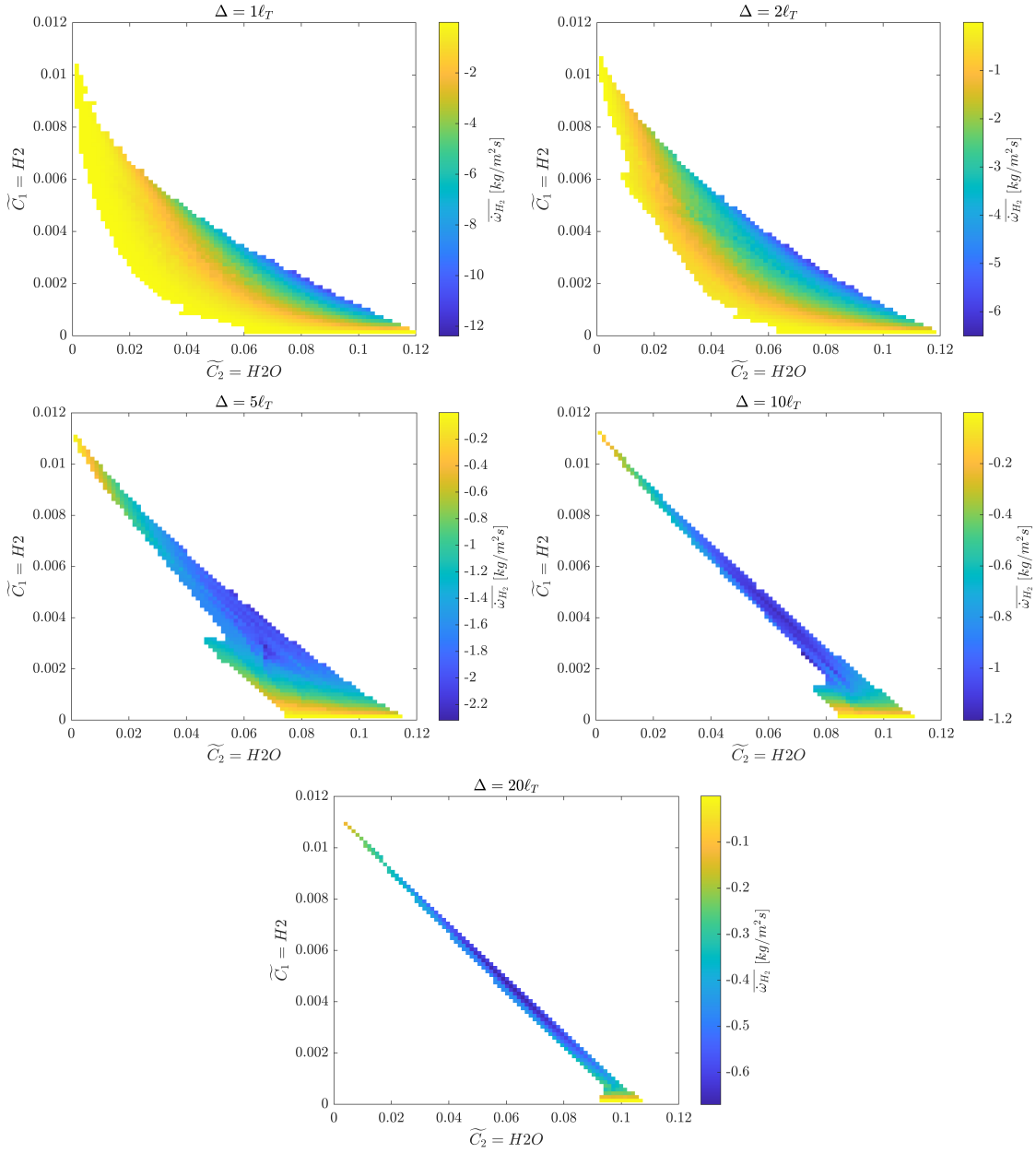


**Figure 7.5:** $H_2$ source term tabulated from the small-scale filtered DNS. Colormaps not uniform.

## 7.4 *A-priori* validation

The model is validated *a-priori* following the procedure presented in [56]. The large-scale DNS is filtered with the same filter sizes used for the manifolds definition, and compared to the filtered production rates constructed using the small-scale filtered and tabulated DNS, referred to as "a-priori LES" in the following. A visual comparison between the filtered and reconstructed fields is provided in Fig. 7.6-7.10 for the several filter size analyzed.
It can be observed that the model correctly reproduced the filtered large-scale DNS for all the filter sizes, with some minor difference in the peak values reconstruction only for the largest filter size. A slight overestimation of $\dot{\omega}_{H_2}$ is found at each filter size, increasing with the filter coarseness.

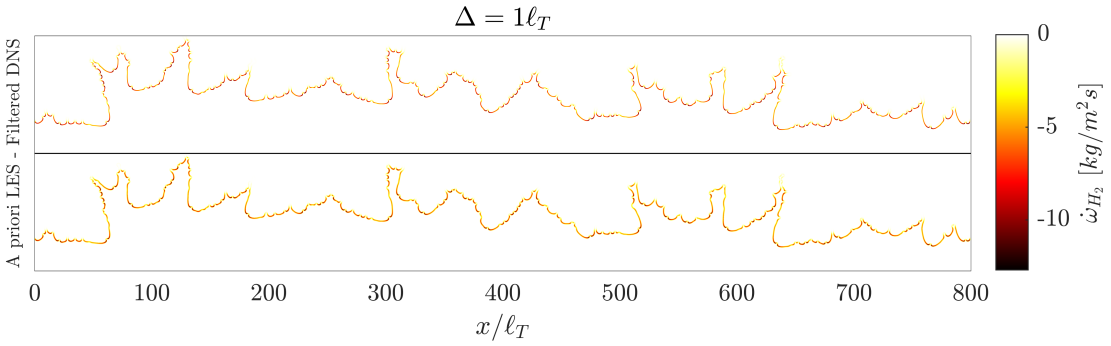


**Figure 7.6:** Comparison between the filtered DNS (top) and the *a priori* LES (bottom) for a filter size $\Delta = 1\ell_T$

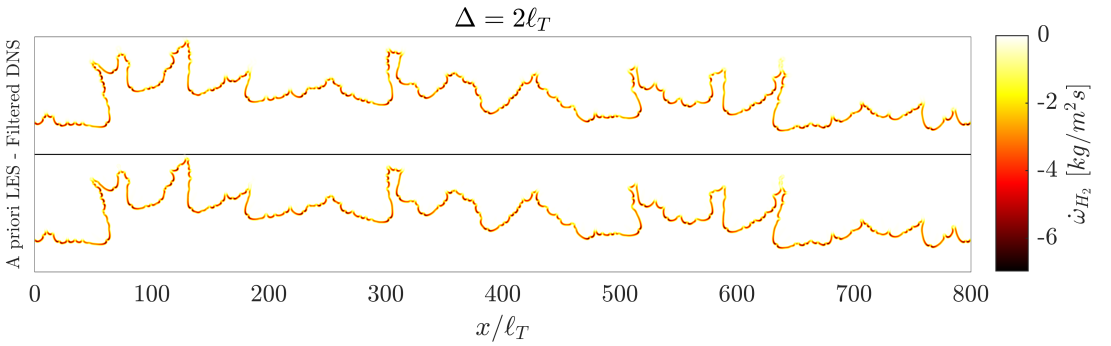


**Figure 7.7:** Comparison between the filtered DNS (top) and the *a priori* LES (bottom) for a filter size $\Delta = 2\ell_T$

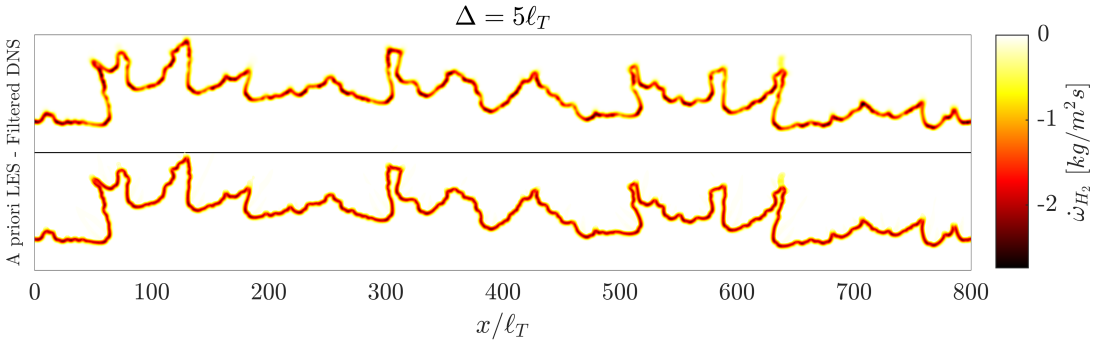


**Figure 7.8:** Comparison between the filtered DNS (top) and the *a priori* LES (bottom) for a filter size $\Delta = 5\ell_T$

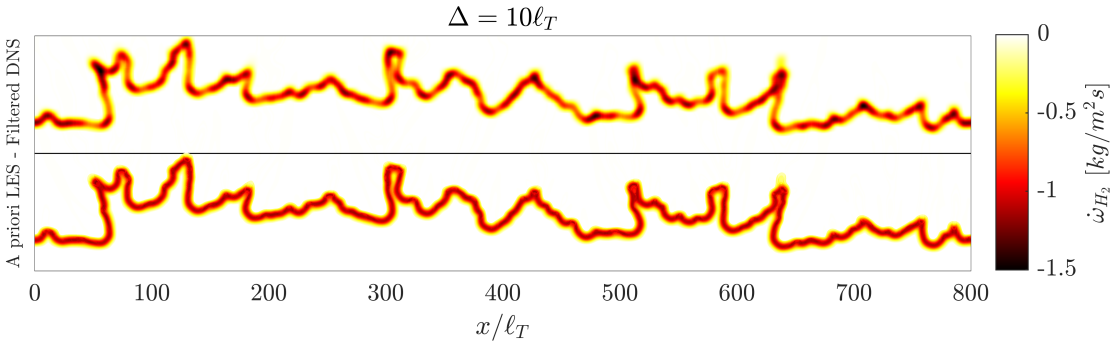


**Figure 7.9:** Comparison between the filtered DNS (top) and the *a priori* LES (bottom) for a filter size $\Delta = 10\ell_T$

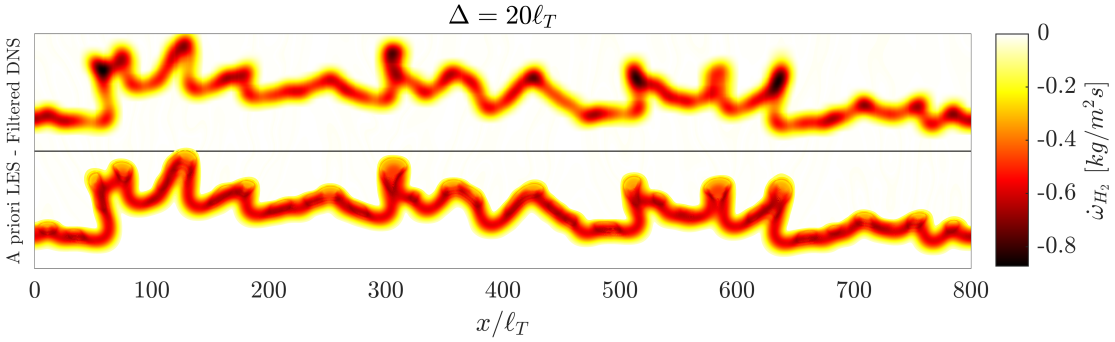


**Figure 7.10:** Comparison between the filtered DNS (top) and the *a priori* LES (bottom) for a filter size $\Delta = 20\ell_T$

In order to have a more quantitative evaluation of the model performance, the flame consumption speed has been calculated for each configuration, with the following definition:

$$S_c = -\frac{1}{L_x \rho_u Y_{H2,u}} \int \dot{\omega}_{H2} dxdy$$

with $L_x$ the domain width in the cross-wise direction, $\rho_u$ the density in the unburned mixture, $Y_{H2,u}$ the mass fraction of hydrogen in the unburned mixture and $\dot{\omega}_{H2}$ the consumption rate of molecular hydrogen [8]. Results are shown in Fig. 7.11 in terms of consumption speed normalized to the laminar flame speed. It is observed that the maximum error on the consumption speed prediction increases with the filter size, but is in any case lower than $\sim 15$ %.

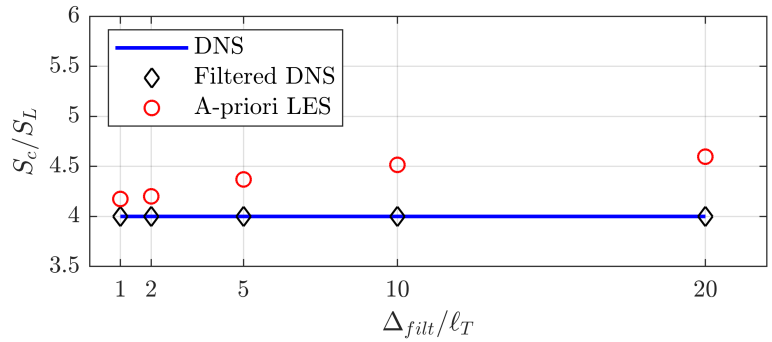


**Figure 7.11:** Comparison of the consumption speeds obtained for the several filter sizes.

## 7.5 Future perspectives

The modeling strategy validated a-priori in the previous Section is expected to contribute in the development of modeling framework for LES of lean hydrogen premixed flames. A single-scalar filtered tabulated model akin to the one presented is currently being used to validate an LES numerical framework for high pressure premixed combustion within the OpenFOAM environment. Some preliminary results are shown in Fig. 7.12, where the progress variable $C$ of the reference DNS is compared to the corresponding LES field. As said in the previous Sections, a single-scalar model is not sufficient for the description of unstable hydrogen flames, the testcase considered in Fig. 7.12 and chosen for the preliminary validation of the LES tool is therefore a methane/air premixed flame, in particular the R3 flame developed by S. Luca et al in [70].

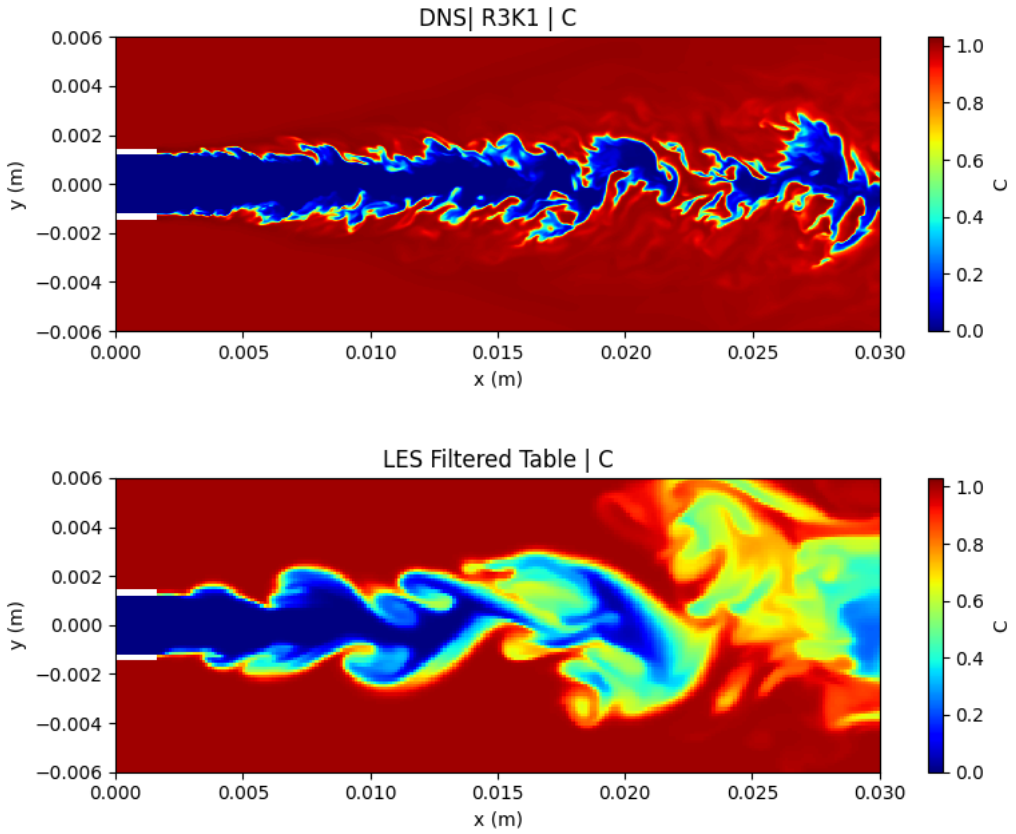


**Figure 7.12:** Preliminary results of the methane/air LES (bottom) compared to the reference R3 DNS flame [70]. Results are shown in terms of progress variable $C$.

A two-scalars filtered tabulated model for LES simulation of unstable premixed flames is being concurrently developed in OpenFOAM, with a twofold implementation in order to accommodate both the Regele model [101] and the data-driven model here validated in an *a-priori* fashion. Future work will be devoted to the *a-posteriori* validation of both the approaches against the DNS developed by L. Berger et al in. [7].

# Chapter 8

# Conclusions

The issue of the numerical modeling of high energy density devices based on high pressure turbulent combustion has been addressed in this work through the application of a number of modeling strategies and stiffness-reduction techniques. The two topics that are investigated deal with two major applications respectively in the context of non-premixed and premixed combustion.

The issue of the thermal characterization of Liquid Rocket Engine was first tackled. The numerical framework for the simulation of two-dimensional and three-dimensional rocket combustion chambers is based on an efficient numerical uRANS framework, embedding a flamelet-based approach for turbulent non-premixed combustion modeling, as well as a wall-modeled description for the boundary layers. Additional feature were then introduced in the formulation to deal with different configurations:

- The baseline formulation of the numerical framework, relying on a low-Mach number assumption, was exploited investigate several aspects of the injector layout of an experimental gaseous oxygen/gaseous methane experimental combustor adopted as reference test-case in a two-dimensional axis-symmetric approximation. First the combustion chamber lateral wall was substituted with a symmetry boundary condition in order to mimic the mutual interaction between injectors located in the central part of a generic multi-injector chamber. The resulting symmetric configuration was compared to the canonical wall-bounded configuration to assess the effects on the ensuing flow fields. For each of the two configurations, different sets of boundary conditions for temperature have been tested, analyzing their effect on the resulting heat flux and wall temperature.
- A parametric analysis of the lateral confinement length effect was performed through a series of two-dimensional simulations, varying the lateral confinement length in a range of interest. Results in terms of surface averaged heat flux, heat transfer coefficient, wall temperature and mixture fraction were reported as functions of the confinement length. It was found that the heat flux and heat transfer coefficient follow a decreasing trend on the combustion chamber lateral wall, while temperature and mixture fraction show a negligible variation. Conversely, the major effect of the confinement increase on the injection plates of both the wall-bounded and symmetric configurations is a steep temperature increase, that causes a decreasing heat transfer coefficient despite the increasing heat flux with increasing confinement length. This was explained observing the interaction between the recirculating flow and the flame with

varying dimension of the lateral confinement. Comparing the data collected on the injection plates, scaling exponents were finally calculated in order to characterize the effects of confinement lengths.

- A data-driven model for the thermal load prediction on generic multi injector geometries was preliminary discussed, based on the correlation between heat flux and geometry gleaned from the database collection. Such a model is based on the definition, for each injector on the firing plate, of an equivalent confinement depending on the mutual placement of the surrounding injectors and on the distance from the chamber wall, and is meant to actively support the design stage of a multi-injector combustion chamber once the injector layout is known by providing an estimate of the thermal load without resorting to computationally onerous three-dimensional simulations. The model was found to reproduce well the main field features.

- The low-Mach number formulation was then scaled-up to a multi-region and multi-physics framework for the time-resolved modeling of turbulent combustion and heat transfer across neighbouring continua. The solver tackles multiple solid and fluid domains, prescribing temperature and heat flux continuity across the interfaces, and aims at being predictive over the wall thermal characterization avoiding any modeling assumption. The coupling strategy was optimized for convection-dominated phenomena, providing a framework which is both predictive for the time-dependent temperature evolution and affordable from the point of view of cost-effectiveness. The solver was validated by comparison with the analytical solution of a multi-layer wall, replicating the literature results on a benchmark backward facing step mono-species flow and finally reproducing the complete run of 2D and 3D experimental capacitively cooled combustors, either single and multi injector showing overall promising performance for lab-scale thermal analysis.

- A further scaling-up of the numerical framework fidelity was then obtained introducing the modeling of compressibility effects. First a parametric analysis of the inlet mass-flow effect was conducted through the collection of a database of two-dimensional single-region simulations. It was found that the wall heat flux and pressure, increase with increasing mass-flows, as well as the density. Scaling exponents were calculated to assess the dependence of the thermal and mechanical load from the inlet mass-flow and one from each other.

- The compressible formulation was finally embedded in the multi-region framework, allowing for the coupled simulation of a capacitively cooled combustor from the injection to the nozzle expansion. The complete duration of the experimental run was reproduced and the results were compared to the reference literature data.

The second field of applications tackled in the Thesis was the premixed combustion modeling typical of devices for power generation. In particular, the issue of lean premixed hydrogen flame was addressed. A filtered tabulated chemistry model was proposed and preliminary validated in an a-priori fashion. The model falls under the category of the lower-dimensional manifold representations and is based on the filtering of a fully-resolved, two-dimensional, thermo-diffusively unstable flame to recover, for each spatial filter size, all filtered thermochemical quantities as a function of

two conserved scalars, namely the mass fraction of molecular hydrogen and water. The model was finally validated a-priori, comparing the filtered DNS with the corresponding filtered fields constructed accessing the tables.

# Appendix A

# Pseudo-code

A more detailed explanation of the data-driven model presented in Sec. 4.5 is given here. The algorithm has been implemented in Matlab [77], therefore its notation will be used in the following.

### Input parameters

| | | |
|---|---|---|
| $\mathtt{n_{inj}}$ | = | Number of injector in the first ring |
| $\mathtt{n_{rings}}$ | = | Number of injector rings |
| `phase` | = | Angular position of the first injector for each ring |
| `Rad` | = | Chamber radius |
| $\mathtt{r_{inj}}$ | = | Injector radius |
| $\mathtt{r_{ring}}$ | = | Distance between equispaced rings |
| `w` | = | Symmetry angle of the multi-injector plate |

### Definition of the multi-injector plate layout

Definition of the matrix `layout`, with a number of rows equal to the total number of injectors on the firing plate and four columns associated to the following information about the $i$-th injector layout:

- 1. Radial distance from the plate centre
- 2. Angular position with respect to the vertical axis of symmetry
- 3-4. $x$ and $y$ Cartesian coordinates

---

**for** i = 1:$\mathtt{n_{rings}}$ **do**
    radii(i, 1:$\mathtt{n_{inj}}$*$i$) = i*r
**end for**
layout(:,1) = nonzeros(radii); ▷ Radial coordinate
**for** i = 1:$\mathtt{n_{rings}}$ **do**
    **for** j = 1:$\mathtt{n_{rings}}$*$\mathtt{n_{inj}}$ **do**
        angles(i,j) = phase(i)+(j-1)*(wedge/i)
    **end for**

---

```
end for
layout(:,2) = nonzeros(angles);                          ▷ Angular position
for i = 1:length(layout) do
    layout(i,3) = layout(i,1)*sin(layout(i,3))           ▷ x-coordinate
    layout(i,4) = layout(i,1)*cos(layout(i,3))           ▷ y-coordinate
end for
```

### Topological tiling

The topological tiling is performed on the basis of geometrical criteria. First a matrix `injRing` is defined, with $n_{rings}$ rows, each one containing as non-zero elements the index of the injectors present on that ring. Starting from this matrix, two rings of injectors are iteratively selected, namely an "inner" ring and and "outer" ring, and a matrix called `slope(j,k)` containing the slope between the `j`-th and `k`-th injector is defined. Finally several conditions on the mutual slopes are applied to identify the tiles edges. If the slope between two injectors, respectively belonging to the inner and outer rings, is equal to a multiple of the symmetry angle of the plate, then the labels of the two injectors are stored in a matrix called `edges`. The external ring is divided into equi-spaced cells centered in each injector, to define the edges a matrix `externalRing` stores the coordinates of the mid-point between neighbouring injectors and of their projection on the chamber wall.

```
for i = 1:n_rings do
    injRing(i,n_inj*i) = find(layout(:,1) == i*r)
end for
for i = 2:n_rings do
    inj_inner = nonzeros(injRing(i-1,:))                 ▷ Injectors on the inner ring
    inj_outer = nonzeros(injRing(i,:))                   ▷ Injectors on the outer ring
    for j = 1:inj_inner do
        for k = 1:inj_outer do
            slope(j,k) = (layout(j,3) − layout(k,3)) / (layout(j,4) − layout(k,4))
        end for
    end for
end for
for i = 2:length(layout) do
    for j = 1:n_rings do+1
        for k = 1:n_rings do+1
            if slope(j,k) = n*w then
                edges(end+1,:) = [inj_inner(j), inj_outer(k)]   ▷ Inner rings tiles vertices
            end if
        end for
    end for
end forinj_external = nonzeros(injRing(end,:))           ▷ Injectors on the external ring
for i = 1:length(inj_external) do
    externalRing(i,1) = n_rings*r_ring                   ▷ Radial coordinate
    externalRing(i,2) = (layout(external(i),2) + layout(external(i+1),2)) / 2   ▷ Angular position
```

```
externalRing(i,3) = externalRing(i,1)*sin(externalRing(i,2))  ▷ x-coord external ring
externalRing(i,4) = externalRing(i,1)*cos(externalRing(i,2))  ▷ y-coord external ring
externalRing(i,5) = Rad*sin(externalRing(i,2))                ▷ x-coord external wall
externalRing(i,5) = Rad*cos(externalRing(i,2))                ▷ y-coord external wall
end for
```

with $n \in [1, 2\pi/\mathtt{w}]$.

### Identification of tiles shapes

Once all the edges of the topological tiles have been drawn, the algorithm must identify which king of tile is (either triangle, diamond or pentagon), by means of some conditions on the consecutiveness of injectors and on the slope of the edges. A matrix named `shapes` is defined, with as many rows as the tiles, and 8 columns with:

- 1-2. $x$ and $y$ coordinates of the cell's centroid
- 3-7. Index of the injectors at the vertices of the cell (0 if less than five vertices)
- 8. Number of cell vertices

Based on this, another matrix named `confinements` is defined. It has again as many rows as the number of tiles, and contains the distance lengths between consecutive vertices and between each vertex and the cell centroid. For the sake of brevity, the geometrical conditions will be qualitatively described without referring to the matrix formulation, and also the calculation of centroids' coordinates and confinement lengths will be omitted. The latter can be easily derived resorting to simple math and trigonometry.

```
for i = 1:length(edges) do
    for j = 1:length(edges) do
        if Two consecutive injectors of the outer ring (j and j+1) correspond to the same injector of the inner ring (i) then
            The shape is a triangle.
        else if Two consecutive injectors of the outer ring (j and j+1) correspond to two consecutive injectors of the inner ring (i and i+1) then
            The shape is a diamond.
        else if Two consecutive injectors of the inner ring (i and i+1) correspond to two injectors of the outer ring with indices j and j+2 then
            The shape is a pentagon.
        end if
    end for
end for
for i = 1:length(shapes) do
    for j = 1:5 do
        confinements(:,i) = distance between consecutive vertices;
        Null elements are left in the last columns for cells with less than 5 vertices.
    end for
```

17: **for** `k = 6:11` **do**
18: `confinements(:,i)` = distance between each vertex and the cell centroid;
19: Null elements are left in the last columns for cells with less than 5 vertices.
20: **end for**
21: **end for**

### Mapping and interpolation

For each confinement length defined in the `confinements` matrix previously introduced a value of heat flux is taken from the database and associated to the corresponding coordinates on the multi-injector faceplate. The ensemble of mapped heat fluxes is finally interpolated on a uniform grid trough the Matlab function `scatteredInterpolant` to obtain the final heat flux field on the firing plate. In particular, the `nearest` method is used, referring to the nearest neighbor interpolation strategy and providing $C^1$ continuous results, as an alternative to the standard linear interpolation.

# Appendix B

# Posters

# Thermal characterization and heat transfer in Liquid Rocket Engines

Arianna Remiddi
"La Sapienza" University of Rome

ICISS on Near-Wall Reactive Flows, Virtual Summer School, June 7th – 10th, 2021

## Summary


- Development of a multi-region solver for turbulent combustion and heat transfer through different continua.
- Framework integrating flamelet-based turbulent combustion, wall modeling and Conjugate Heat Transfer.
- Validation test case: capacitively cooled GCH4/GOX combustor from the Technical University of Munich [1].


## Numerical formulation

- Thermal Fourier equation solved in the solid domains and unsteady Reynols-Averages Navier-Stokes (URANS) equations within the fluid ones.
- Flamelet-based approach tackling non-adiabatic effects to reduce the stiffness of the combustion modeling, well posed under low-Mach number conditions [2].

$$\widetilde{\psi} = \widetilde{\psi}(\widetilde{Z}, \widetilde{Z''^2}, \widetilde{\chi_{st}}, \widetilde{\phi_H})$$

- Resort to thermal wall-functions adjusted for flamelet-based solvers, allowing to avoid the stifness of boundary layers [3].
- Development of the described tool in the context of the open-source frameworks OpenFOAM and OpenSMOKE++ [4].
- 2D axis-symmetric approximation

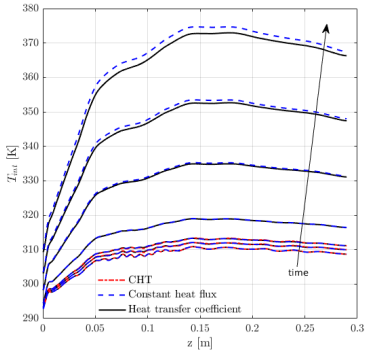


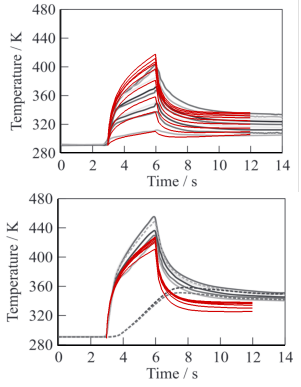


## Coupling at the interface

- Direct coupling: the Conjugate Heat Transfer (CHT) condition enforces the heat fluxes continuity between domains and calculates the resulting interface temperature at each iteration.

$$k_S * \frac{T_S - T_{int}}{\Delta_S} = k_F * \frac{T_F - T_{int}}{\Delta_F}$$

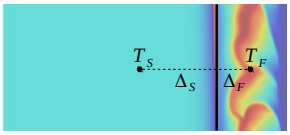


- Loose coupling: once the flow field approaches a steady state condition it is possible to relax the coupling interrupting the fluid-dynamic simulation, in order to proceed on solid conduction time-scales.
  - ✗ A constant heat flux value can be prescribed to the solid domain. This assumption neglects the variation of heat flux with interface temperature and leads to overestimation in the long run.
  - ✔ The convecting heating can be well represented by the corresponding heat transfer coefficient, recasting the interface temperature calculation.

$$k_S * \frac{T_S - T_{int}}{\Delta_S} = h_C * (T_{ad} - T_{int})$$

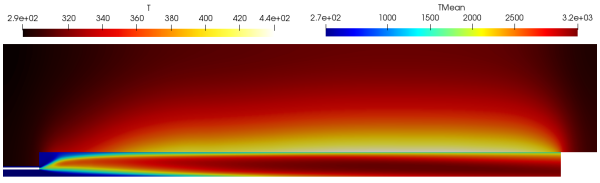


## Results

The newly developed solver can model high-pressure turbulent combustion in LRE-relevant conditions and heat transfer through the solid walls.

A proper alternation of boundary conditions allows to optimize computational resources maintaining a good agreement with the comparative exerimental data.

**Acknowledgments**

This work has been supported by the Italian Ministry of University and Research (MIUR).

**Contacts**

arianna.remiddi@uniroma1.it

**References**

[1] M.P. Celano et al, Progress in Propulsion Physics, 8 (2016) 145-164
[2] P.E. Lapenna et al, Acta Astronautica, 158 (2019) 460–469
[3] G. Indelicato et al, International Journal of Heat and Mass Transfer, 169 (2021) 120913
[4] A. Cuoci et al, Computer Physics Communications, 192 (2015) 237–264
[5] B. Betti et al, Journal of Propulsion and Power, 30 (2014) 360-367

39th INTERNATIONAL SYMPOSIUM ON COMBUSTION
24-29 JULY 2022
VANCOUVER, CANADA

# Numerical investigation of thermal loads in the injection region of liquid rocket engines

P. E. Lapenna*, A. Remiddi*, G. Indelicato*, M. Valorani*, M. Pizzarelli** and F. Creta*

*Department of Mechanical and Aerospace Engineering, Sapienza University of Rome
**Italian Space Agency (ASI)

Contacts: pasquale.lapenna@uniroma1.it ; arianna.remiddi@uniroma1.it

Agenzia Spaziale Italiana

SAPIENZA UNIVERSITÀ DI ROMA

## Background and motivation

- Characterization of heat loads in Liquid Rocket Engines (LRE) combustion chamber is key for:
  - Safety, development and testing
  - Sustainability and Reusability
- Crucial parts of LREs combustion chambers are not easily accessible experimentally
  - Lateral walls and throat region largely investigated
  - Limited knowledge on the injection plate

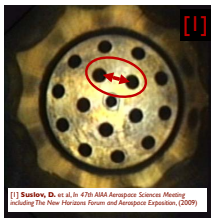


### Objectives of this work:

- Understand how the injector arrangement influence thermal loads in the injection region
- Data-driven scalings for preliminary design and heat flux estimation on the firing plate

## Methods

- **Parametric 2D axi-sym CFD analysis on injectors confinement**
- **Needs:**
  - Running a large number of cases for scalings and data-driven surrogate models
  - Efficient modeling of high-pressure, non-premixed, turbulent combustion + heat transfer
- **Numerical Approach:**
  - Consistent low-Mach number approximation of r-NS equations [1,2]
  - Non-adiabatic flamelet-based turbulent combustion model [3]
  - Unsteady RANS with standard k-epsilon turbulence model [4]
  - Algebraic (flamelet-suited) thermal wall functions for boundary layers [3]
  - OpenFOAM and OpenSMOKE++ numerical frameworks [5]

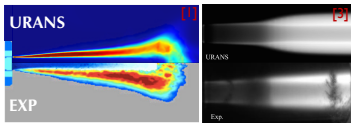


[1] P. E. Lapenna et al. *Acta Astronautica* (2019)
[2] G. Indelicato et al. *Combust. Sci. Technol.* (2020)
[3] G. Indelicato et al. *Int. Jour. Heat Mass Tansf.* (2021)
[4] C. Lian and C.L. Merkle *Comput. Fluids* (2011)
[5] A. Cuoci et al. *Comput. Phys. Commun.* (2015)
[6] M.P. Celano et al. *Prog. Prop. Phys.* (2016)

- **Additional 3D simulation**
  - 37 Injector elements replicating the TUM single injector geometry
  - Test the axi-sym 2D dataset on a reference 3D simulation
  - Same numerical settings and b.c. of 2D cases on a ~10Mill grid points

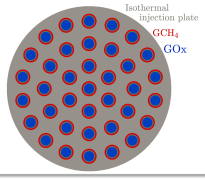


- 2 configurations (wall-bounded and sym-bounded) to simulate interactions in a generic multi-injector plate

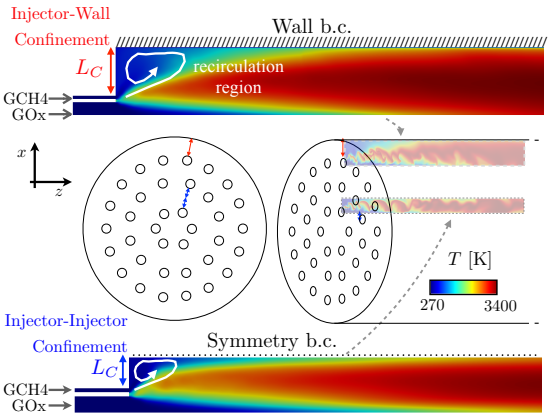


- The reference is the TUMrig single injector [6]
- The confinement $Lc$ is parametrically modified
- Nominal $Lc$ from the reference injector on which the code has been validated [3]
- Scalings for heat flux and heat transfer coefficients can be derived

## Results

- **Effect of increasing confinement length $Lc$ on the flow-field**

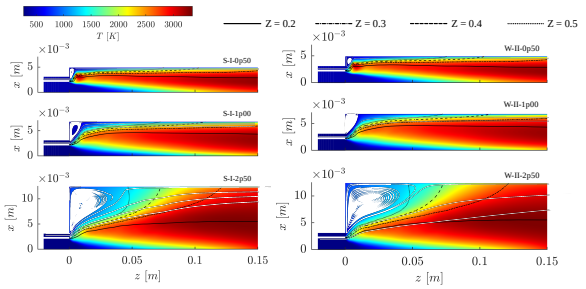


- Sym-bounded case
- Wall-bounded case

- **Effect of increasing confinement length $Lc$ on injection plate heat flux**

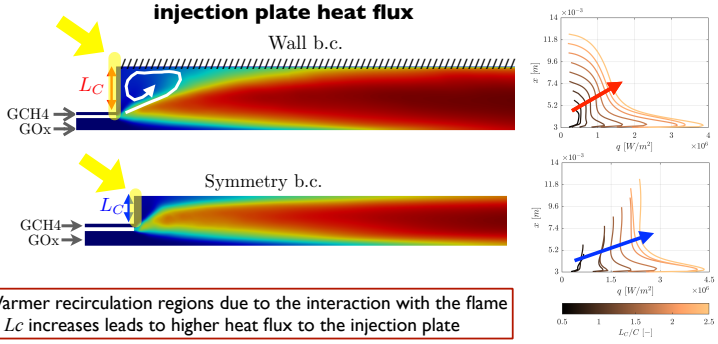


- Warmer recirculation regions due to the interaction with the flame as $Lc$ increases leads to higher heat flux to the injection plate

- **Reference 37 Injectors 3D simulation**

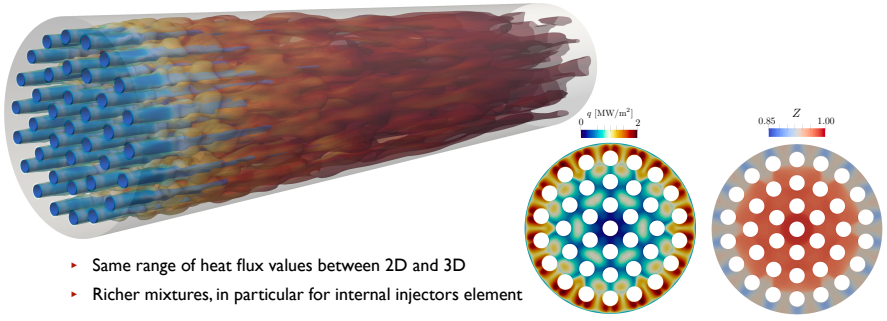


- Same range of heat flux values between 2D and 3D
- Richer mixtures, in particular for internal injectors element

- **Scaling coefficients for injection plates**

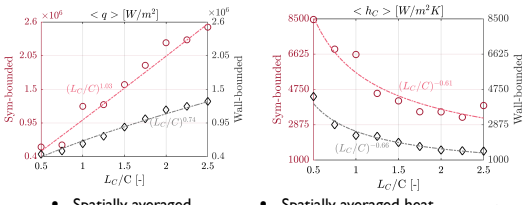


- Spatially averaged mean heat flux
- Spatially averaged heat transfer coefficient $h_C = \frac{q}{T_{ad} - T_w}$

**Acknowledgments**
This research was jointly funded by Sapienza University and the Italian Space Agency - Agenzia Spaziale Italiana (ASI) as part of the research N.2019-4-HH.0 carried out under the framework agreement N.2015-1-Q.0 CUP:F86C17000080005

# A flamelet-based numerical framework for Conjugate Heat Transfer in rocket combustion chambers

A. Remiddi*, G. Indelicato, P.E. Lapenna, F. Creta

*Dept. of Mechanical and Aerospace Engineering,"La Sapienza" University of Rome*
*arianna.remiddi@uniroma1.it

First Italian OpenFOAM User Meeting – Milano, October 19th 2022

## Background and motivation

- Importance of thermal management for rocket combustion chambers
- Numerical simulation to replace experiments
- Interplay of multi-scale and multi-physics phenomena

## Objective

Development of an efficient multi-domain tool for time-resolved thermal characterization of rocket combustion chambers

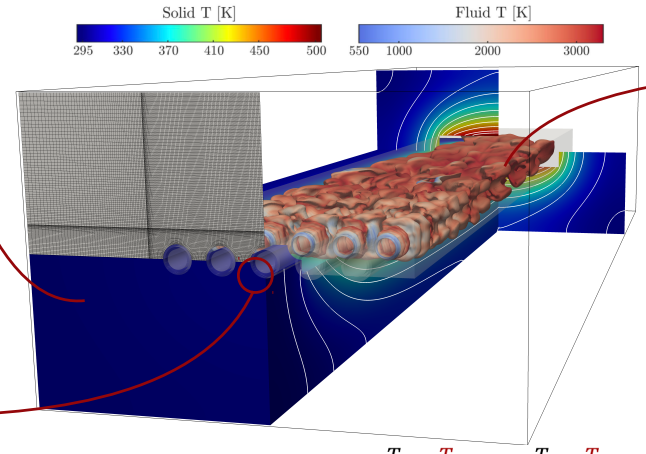


## Solid domain

Thermal Fourier equation

Suitable for porous or anisotropic continua

$$\frac{\partial(\rho h)}{\partial t} = \frac{\partial}{\partial x_j}\left(\alpha\left(\frac{\partial h}{\partial x_j}\right)\right)$$

## Fluid domain

Unsteady RANS

Low-Mach number [1]

k-ε turbulence model

Non-adiabatic flamelet-based turbulent combustion model [2]

Wall modeled [2]

$$\tilde{\psi} = \tilde{\psi}\left(\tilde{Z}, \widetilde{Z''^2}, \tilde{\chi}_{st}, \tilde{\phi}_H\right)$$

## Interface coupling

Combination of Conjugate Heat Transfer and thermal chaining [3]

Allows for the simulation of laboratory and industrial-scale

Suitable for mono- and multi-species flows, both laminar and turbulent

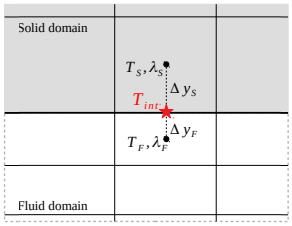


$$\lambda_F \frac{T_F - T_{int}}{\Delta_F} = \lambda_S \frac{T_S - T_{int}}{\Delta_S}$$

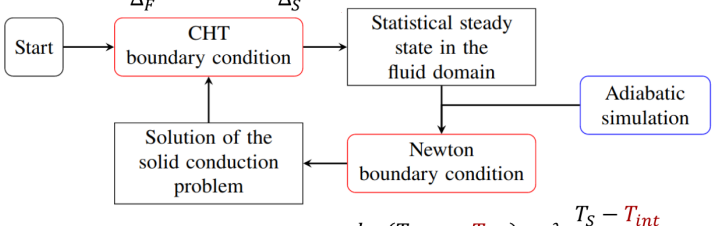


$$h_C\,(T_{F,ad} - T_{int}) = \lambda_S \frac{T_S - T_{int}}{\Delta_S}$$

**Test-case:** Capacitively cooled TUMrig combustors [4,5]

## Results

### Single-injector 2D axis-sym configuration

The solver is capable of reproducing the entire experimental run

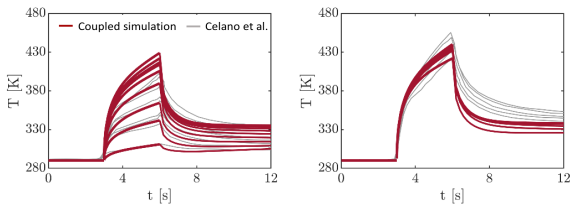


The temperature signals in time and the wall heat flux are in good agreement with the experimental data [2,4,5]

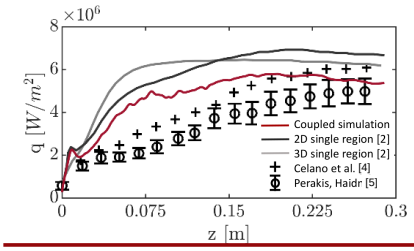


### Single-injector 3D configuration

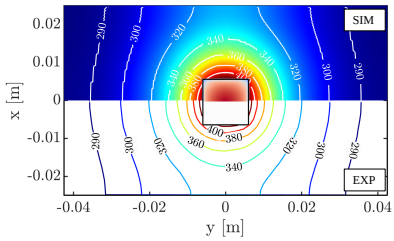


Agreement between the temperature field in the solid domain and the reference data [5]

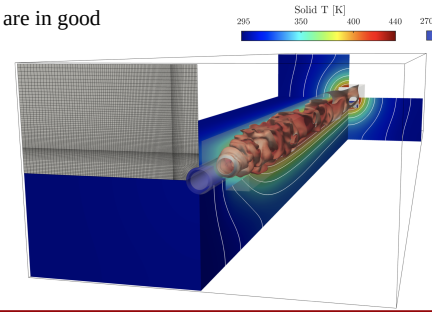


The interface temperature calculated with the Newton condition is in perfect continuity with the CHT approach

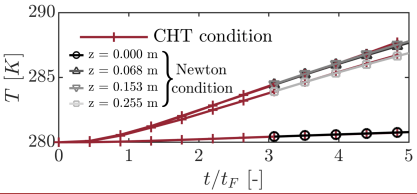


## References

[1] P.E. Lapenna et al. Acta Astronautica (158) 460-469, 2019

[2] G. Indelicato et al. Int. Jour. Heat Mass Transf. (169) 120913, 2021

[3] A. Remiddi et al. Proc. Combust. Inst. (in press) 2022

[4] M.P. Celano et al. 52Nd AIAA/SAE/ASEE Joint Prop. Conf. (8) 145-164, 2016

[5] N. Perakis, O. Haidn. Int. Jour. Heat Mass Transf. (131) 150-166, 2019

# Bibliography


[1] S. Ahdy, M. Boraey, H. Abdel Hameed, and H. El Salmawy. Effect of the wall thermal boundary condition on the structure of a confined swirling diffusion flame. *Journal of the Brazilian Society of Mechanical Sciences and Engineering*, 41(11), 2019.

[2] C. Altantzis, C. Frouzakis, A. Tomboulides, S. Kerkemeier, and K. Boulouchos. Detailed numerical simulations of intrinsically unstable two-dimensional planar lean premixed hydrogen/air flames. *Proceedings of the Combustion Institute*, 33:1261–1268, 12 2011.

[3] C. Angelberger, T. Poinsot, and B. Delhay. Improving near-wall combustion and wall heat transfer modeling in si engine computations. Technical report, SAE Technical Paper, 1997.

[4] H. Asakawa, H. Nanri, K. Aoki, I. Kubota, H. Mori, Y. Ishikawa, K. Kimoto, S. Ishihara, and S. Ishizaki. *The status of the research and development of LNG rocket engines in Japan*. Springer, 2017.

[5] D. T. Banuti. A thermodynamic look at injection in aerospace propulsion systems. 01 2020.

[6] P. Bellomi, M. Rudnykh, S. Carapellese, D. Liuzzi, G. Caggiano, L. Arione, A. Gurtovoy, S. Lobov, V. Rachuk, E. D'Aversa, et al. Development of LM10-MIRA liquid oxygen–liquid natural gas expander cycle demonstrator engine. *Progress in Propulsion Physics–Volume 11*, 11:447–466, 2019.

[7] L. Berger, A. Attili, and H. Pitsch. Intrinsic instabilities in premixed hydrogen flames: parametric variation of pressure, equivalence ratio, and temperature. part 2 – non-linear regime and flame speed enhancement. *Combustion and Flame*, 240:111936, 2022.

[8] L. Berger, K. Kleinheinz, A. Attili, and H. Pitsch. Characteristic patterns of thermodiffusively unstable premixed lean hydrogen flames. *Proceedings of the Combustion Institute*, 37:1879–1886, 07 2019.

[9] B. Betti. *Flow field and heat transfer analysis of oxygen/methane liquid rocket engine thrust chambers.* PhD Thesis, 2012.

[10] B. Betti, D. Bianchi, F. Nasuti, and E. Martelli. Chemical reaction effects on heat loads of CH4/O2 and H2/O2 rockets. *AIAA Journal*, 54(5):1693–1703, 2016.

[11] B. Betti, M. Pizzarelli, and F. Nasuti. Coupled heat transfer analysis in regeneratively cooled thrust chambers. *J. Prop. Power*, 30(2):360–367, 2014.

[12] J. Bredberg. On the wall boundary condition for turbulence models. *Chalmers University of Technology, Department of Thermo and Fluid Dynamics. Internal Report 00/4. G oteborg*, pages 8–16, 2000.

[13] M. P. Burke, M. Chaos, Y. Ju, F. L. Dryer, and S. J. Klippenstein. Comprehensive h2/o2 kinetic model for high-pressure combustion. *International Journal of Chemical Kinetics*, 44(7):444–474, 2012.

[14] O. Cabrit and F. Nicoud. Direct simulations for wall modeling of multicomponent reacting compressible turbulent flows. *Physics of Fluids*, 21(5):055108, 2009.

[15] M. P. Celano, S. Silvestri, G. Schlieben, C. Kirchberger, O. J. Haidn, and O. Knab. Injector characterization for a gaseous oxygen-methane single element combustion chamber. *Prog. Prop. Phys.*, 8:145–164, 2016.

[16] A. Chemnitz, T. Sattelmayer, C. Roth, O. Haidn, Y. Daimon, R. Keller, P. Gerlinger, J. Zips, and M. Pfitzner. Numerical investigation of reacting flow in a methane rocket combustor: turbulence modeling. *J. Prop. Power*, 34(4):864–877, 2018.

[17] R. Cheng, D. Littlejohn, P. Strakey, and T. Sidwell. Laboratory investigations of a low-swirl injector with h2 and ch4 at gas turbine conditions. *Proceedings of the Combustion Institute*, 32:3001–3009, 03 2009.

[18] I. Chterev and I. Boxx. Effect of hydrogen enrichment on the dynamics of a lean technically premixed elevated pressure flame. *Combustion and Flame*, 225:149–159, 2021.

[19] W. T. Chung, A. A. Mishra, N. Perakis, and M. Ihme. Data-assisted combustion simulations with dynamic submodel assignment using random forests. *Combust.Flame*, 227:172–185, 2021.

[20] R. Courant, K. O. Friedrichs, and H. Lewy. Uber die partiellen differenzgleichungen der matematishen physik. *Matematishe Annalen*, 100:32–74, 1928.

[21] F. Creta, R. Lamioni, P. Lapenna, and G. Troiani. Interplay of darrieus-landau instability and weak turbulence in premixed flame propagation. *Physical Review E*, 94, 11 2016.

[22] F. Creta, P. E. Lapenna, R. Lamioni, N. Fogla, and M. Matalon. Propagation of premixed flames in the presence of darrieus–landau and thermal diffusive instabilities. *Combustion and Flame*, 216:256–270, 2020.

[23] A. Cuoci, A. Frassoldati, T. Faravelli, and E. Ranzi. Opensmoke++: An object-oriented framework for the numerical modeling of reactive systems with detailed kinetic mechanisms. *Computer Physics Communications*, 192:237–264, 2015.

[24] M. Day, S. Tachibana, J. Bell, M. Lijewski, V. Beckner, and R. K. Cheng. A combined computational and experimental characterization of lean premixed turbulent low swirl laboratory flames ii. hydrogen flames. *Combustion and Flame*, 162(5):2148–2165, 2015.

[25] E. Erturk. Numerical solutions of 2-d steady incompressible flow over a backward-facing step, part i: High reynolds number solutions. *Computers Fluids*, 37(6):633–655, 2008.

[26] J. H. Ferziger, M. Perić, and R. L. Street. *Computational methods for fluid dynamics*, volume 3. Springer, 2002.

[27] V. Fico, L. Cutrone, and F. Battista. Assessment of wall-functions ke turbulence models for the prediction of the wall heat flux in rocket combustion chambers. In *44th AIAA/ASME/SAE/ASEE Joint Propulsion Conference & Exhibit*, page 4558, 2008.

[28] B. Fiorina, R. Vicquelin, P. Auzillon, N. Darabiha, O. Gicquel, and D. Veynante. A filtered tabulated chemistry model for les of premixed combustion. *Combustion and Flame*, 157(3):465–475, 2010.

[29] C. E. Frouzakis, N. Fogla, A. G. Tomboulides, C. Altantzis, and M. Matalon. Numerical study of unstable hydrogen/air flames: Shape and propagation speed. *Proceedings of the Combustion Institute*, 35(1):1087–1095, 2015.

[30] D. K. Gartling. A test problem for outflow boundary conditions—flow over a backward-facing step. *International Journal for Numerical Methods in Fluids*, 11(7):953–967, 1990.

[31] O. Gicquel, N. Darabiha, and D. Thévenin. Liminar premixed hydrogen/air counterflow flame simulations using flame prolongation of ildm with differential diffusion. *Proceedings of the Combustion Institute*, 28(2):1901–1908, 2000.

[32] S. Girimaji. Assumed $\beta$-pdf model for turbulent mixing: Validation and extension to multiple scalar mixing. *Combustion Science and Technology*, 78(4-6):177–196, 1991.

[33] Z. Han and R. D. Reitz. A temperature wall function formulation for variable-density turbulent flows with application to engine convective heat transfer modeling. *Int. j. Heat Mass Transf.*, 40(3):613–625, 1997.

[34] H. Huo and V. Yang. Large-eddy simulation of supercritical combustion: Model validation against gaseous h 2–o 2 injector. *Journal of Propulsion and Power*, 33(5):1272–1284, 2017.

[35] A. Iannetti, N. Girard, D. Tchou-Kien, C. Bonhomme, N. Ravier, and E. Edeline. Prometheus, a LOX/LCH4 reusable rocket engine. In *Proceedings of 7th EUCASS*, pages 3–6, 2017.

[36] G. Indelicato. *Modelling of wall-bounded high pressure flows in Liquid Rocket Engines*. PhD Thesis, 2022.

[37] G. Indelicato, P. Lapenna, A. Remiddi, and F. Creta. An efficient modeling framework for wall heat flux prediction in rocket combustion chambers using non adiabatic flamelets and wall-functions. *Int. j. Heat Mass Transf.*, 169:120913, 2021.

[38] G. Indelicato, P. E. Lapenna, R. Concetti, M. Caputo, M. Valorani, G. Magnotti, and F. Creta. Numerical investigation of high pressure CO2-diluted combustion using a flamelet-based approach. *Combustion Science and Technology*, 192(11):2028–2049, 2020.

[39] G. Indelicato, F. Vona, A. Remiddi, P. E. Lapenna, and F. Creta. A flamelet-based numerical framework for the simulation of low-to-high Mach number flows in LRE. In *AIAA Propulsion and Energy 2020 Forum*, page 3822, 2020.

[40] R. Issa. Solution of the implicitly discretised fluid flow equations by operator-splitting. *Journal of Computational Physics*, 62(1):40–65, 1986.

[41] H. Jasak. *Error analysis and estimation for the finite volume method with applications to fluid flows*. PhD Thesis, 1996.

[42] G.-S. Jiang and C.-W. Shu. Efficient implementation of weighted eno schemes. *Journal of Computational Physics*, 126(1):202–228, 1996.

[43] S. Kadowaki and T. Hasegawa. Numerical simulation of dynamics of premixed flames: flame instability and vortex–flame interaction. *Progress in Energy and Combustion Science*, 31(3):193–241, 2005.

[44] S. Kadowaki, H. Suzuki, and H. Kobayashi. The unstable behavior of cellular premixed flames induced by intrinsic instability. *Proceedings of the Combustion Institute*, 30(1):169–176, 2005.

[45] P. Kanna and M. K. Das. Conjugate heat transfer study of backward-facing step flow – a benchmark problem. *International Journal of Heat and Mass Transfer*, 49(21):3929–3941, 2006.

[46] W. M. Kays. Turbulent Prandtl Number—Where Are We? *Journal of Heat Transfer*, 116(2):284–295, 05 1994.

[47] S.-K. Kim, M. Joh, H. S. Choi, and T. S. Park. Multidisciplinary simulation of a regeneratively cooled thrust chamber of liquid rocket engine: Turbulent combustion and nozzle flow. *International Journal of Heat and Mass Transfer*, 70:1066–1077, 2014.

[48] T. Kim, Y. Kim, and S.-K. Kim. Numerical analysis of gaseous hydrogen/liquid oxygen flamelet at supercritical pressures. *International Journal of Hydrogen Energy*, 36(10):6303–6316, 2011.

[49] T. Kim, Y. Kim, and S.-K. Kim. Effects of pressure and inlet temperature on coaxial gaseous methane/liquid oxygen turbulent jet flame under transcritical conditions. *The Journal of Supercritical Fluids*, 81:164–174, 2013.

[50] A. Kishimoto, H. Moriai, K. Takenaka, T. Nishiie, M. Adachi, A. Ogawara, and R. Kurose. Application of a nonadiabatic flamelet/progress-variable approach to large-eddy simulation of h2/o2 combustion under a pressurized condition. *Journal of Heat Transfer*, 139(12), 2017.

[51] E. Knudsen and H. Pitsch. A general flamelet transformation useful for distinguishing between premixed and non-premixed modes of combustion. *Combustion and Flame*, 156(3):678–696, 2009.

[52] E. Knudsen and H. Pitsch. Capabilities and limitations of multi-regime flamelet combustion models. *Combustion and Flame - COMBUST FLAME*, 159, 01 2012.

[53] H. Kobayashi and H. Kawazoe. Flame instability effects on the smallest wrinkling scale and burning velocity of high-pressure turbulent premixed flames. *Proceedings of the Combustion Institute*, 28:375–382, 12 2000.

[54] M. Krügener, J. F. Zapata Usandivaras, M. Bauerheim, and A. Urbano. Coaxial-injector surrogate modeling based on reynolds-averaged navier–stokes simulations using deep learning. *Journal of Propulsion and Power*, 38(5):783–798, 2022.

[55] P. E. Lapenna, R. Amaduzzi, D. Durigon, G. Indelicato, F. Nasuti, and F. Creta. Simulation of a single-element GCH4/GOx rocket combustor using a non-adiabatic flamelet method. In *AIAA-paper*, page 4872, 2018.

[56] P. E. Lapenna, L. Berger, A. Attili, R. Lamioni, N. Fogla, H. Pitsch, and F. Creta. Data-driven subfilter modelling of thermo-diffusively unstable hydrogen–air premixed flames. *Combustion Theory and Modelling*, 25(6):1064–1085, 2021.

[57] P. E. Lapenna, L. Berger, F. Creta, and H. Pitsch. *"Chapter on Laminar Hydrogen Flame" in "Hydrogen for Future Thermal Engines"*. E. Tingas, Springer, (To appear).

[58] P. E. Lapenna, P. P. Ciottoli, and F. Creta. Unsteady non-premixed methane/oxygen flame structures at supercritical pressures. *Combustion Science and Technology*, 189(12):2056–2082, 2017.

[59] P. E. Lapenna, P. P. Ciottoli, and F. Creta. The effect of fuel composition on the non-premixed flame structure of lng/lox mixtures at supercritical pressure. *AIAA Paper 2016–0690*, January 2016.

[60] P. E. Lapenna and F. Creta. Mixing under transcritical conditions: An a-priori study using direct numerical simulation. *The Journal of Supercritical Fluids*, 128:263–278, 2017.

[61] P. E. Lapenna and F. Creta. Direct numerical simulation of transcritical jets at moderate reynolds number. *AIAA Journal*, 57(6):2254–2263, 2019.

[62] P. E. Lapenna, G. Indelicato, R. Lamioni, and F. Creta. Modeling the equations of state using a flamelet approach in LRE-like conditions. *Acta Astronautica*, 158:460–469, 2019.

[63] P. E. Lapenna, R. Lamioni, and F. Creta. Subgrid modeling of intrinsic instabilities in premixed flame propagation. *Proceedings of the Combustion Institute*, 38(2):2001–2011, 2021.

[64] P. E. Lapenna, R. Lamioni, G. Troiani, and F. Creta. Large scale effects in weakly turbulent premixed flames. *Proceedings of the Combustion Institute*, 37(2):1945–1952, 2019.

[65] B. Launder and D. Spalding. The numerical computation of turbulent flows. *Computer Methods in Applied Mechanics and Engineering*, 3(2):269–289, 1974.

[66] C. K. Law. *Combustion Physics*. Cambridge University Press, 2006.

[67] D. Lee, S. Thakur, J. Wright, M. Ihme, and W. Shyy. Characterization of flow field structure and species composition in a shear coaxial rocket GH2/GO2 injector: modeling of wall heat losses. In *AIAA Paper 2011–6125*, July 2011.

[68] C. Lian and C. L. Merkle. Contrast between steady and time-averaged unsteady combustion simulations. *Computers & fluids*, 44(1):328–338, 2011.

[69] K. Liang, B. Yang, and Z. Zhang. Investigation of heat transfer and coking characteristics of hydrocarbon fuels. *Journal of Propulsion and Power*, 14(5):789–796, 1998.

[70] S. Luca, A. Attili, E. Lo Schiavo, F. Creta, and F. Bisetti. On the statistics of flame stretch in turbulent premixed jet flames in the thin reaction zone regime at varying reynolds number. *Proceedings of the Combustion Institute*, 37(2):2451–2459, 2019.

[71] P. C. Ma, H. Wu, M. Ihme, and J.-P. Hickey. Nonadiabatic flamelet formulation for predicting wall heat transfer in rocket engines. *AIAA Journal*, 56(6):2336–2349, 2018.

[72] D. Maestro, B. Cuenot, and L. Selle. Large Eddy Simulation of Combustion and Heat Transfer in a Single Element GCH4/GOx Rocket Combustor. *Flow Turb. Combust.*, 103, 09 2019.

[73] B. Marracino and D. Lentini. Radiation modelling in non-luminous nonpremixed turbulent flames. *Combustion science and technology*, 128(1-6):23–48, 1997.

[74] M. Matalon. Intrinsic flame instabilities in premixed and nonpremixed combustion. *Annual Review of Fluid Mechanics*, 39(1):163–191, 2007.

[75] M. Matalon. Flame dynamics. *Proceedings of the Combustion Institute*, 32(1):57–82, 2009.

[76] M. Matalon. The darrieus–landau instability of premixed flames. *Fluid Dynamics Research*, 50(5):051412, aug 2018.

[77] The Mathworks, Inc., Natick, Massachusetts. *MATLAB version 9.10.0.1613233 (R2021a)*, 2021.

[78] J. C. Melcher and R. L. Morehead. Combustion stability characteristics of the project morpheus liquid oxygen/liquid methane main engine. *AIAA Paper 2014–3681*, July 2014.

[79] D. Muto, Y. Daimon, H. Negishi, and T. Shimizu. Wall modeling of turbulent methane/oxygen reacting flows for predicting heat transfer. *Int. j. Heat Mass Transf.*, 87:108755, 2021.

[80] D. Muto, Y. Daimon, T. Shimizu, and H. Negishi. An equilibrium wall model for reacting turbulent flows with heat transfer. *Int. j. Heat Mass Transf.*, 141:1187–1195, 2019.

[81] H. Müller, J. Zips, M. Pfitzner, D. Maestro, B. Cuenot, S. Menon, R. Ranjan, P. Tudisco, and L. Selle. Numerical investigation of flow and combustion in a single-element gch4/gox rocket combustor: A comparative les study. *52nd AIAA/SAE/ASEE Joint Propulsion Conference*.

[82] S. V. Patankar. *Numerical heat transfer and fluid flow*. Hemisphere Publishing Corporation, 1981.

[83] N. Perakis and O. J. Haidn. Inverse heat transfer method applied to capacitively cooled rocket thrust chambers. *Int. j. Heat Mass Transf.*, 131:150–166, 2019.

[84] N. Perakis, O. J. Haidn, and M. Ihme. Investigation of CO recombination in the boundary layer of CH4/O2 rocket engines. *Proc. Combust. Inst.*, 38(4):6403–6411, 2021.

[85] N. Perakis, D. Rahn, O. J. Haidn, and D. Eiringhaus. Heat transfer and combustion simulation of seven-element O2/CH4 rocket combustor. *J. Prop. Power*, 35(6):1080–1097, 2019.

[86] N. Peters. Laminar diffusion flamelet models in non-premixed turbulent combustion. *Progress in Energy and Combustion Science*, 10(3):319–339, 1984.

[87] C. Pierce. *Progress-variable approach for large-eddy simulation of turbulent combustion.* PhD Thesis, 2001.

[88] C. D. Pierce and P. Moin. Progress-variable approach for large-eddy simulation of non-premixed turbulent combustion. *Journal of Fluid Mechanics*, 504:73 – 97, 2004.

[89] H. Pitsch. *FlameMaster, a C++ computer program for 0D combustion and 1D laminar flame calculations*.

[90] H. Pitsch and H. Steiner. Large-eddy simulation of a turbulent piloted methane/air diffusion flame (sandia flame d). *Physics of fluids*, 12(10):2541–2554, 2000.

[91] M. Pizzarelli. An algebraic model for structural and life analysis of regeneratively-cooled thrust chambers. *Journal of Propulsion and Power*, 36(2):191–201, 2020.

[92] M. Pizzarelli. Overview and analysis of the experimentally measured throat heat transfer in liquid rocket engine thrust chambers. *Acta Astronautica*, 184:46–58, 2021.

[93] M. Pizzarelli, F. Nasuti, R. Votta, and F. Battista. Validation of conjugate heat transfer model for rocket cooling with supercritical methane. *Journal of Propulsion and Power*, 32(3):726–733, 2016.

[94] T. Poinsot and D. Veynante. *Theoretical and Numerical Combustion*. RT Edwards, Inc. Philadelphia, PA, USA, 2005.

[95] S. B. Pope. Small scales, many species and the manifold challenges of turbulent combustion. *Proceedings of the Combustion Institute*, 34(1):1–31, 2013.

[96] D. Preclik, G. Hagemann, O. Knab, L. Brummer, C. Mading, D. Wiedmann, and P. Vuillermoz. LOX/hydrocarbon propellant trade considerations for future reusable liquid booster engines. *AIAA Paper 2005–3567*, July 2005.

[97] D. Rahn, H. Riedmann, and O. Haidn. Conjugate heat transfer simulation of a subscale rocket thrust chamber using a timescale based frozen non-adiabatic flamelet combustion model. *AIAA Propulsion and Energy Forum*, 2019.

[98] D. Rahn, H. Riedmann, and O. Haidn. Multi-phase impact on the heat load characteristics of a multi-element methane-oxygen rocket thrust chamber. *Int. j. Heat Mass Transf.*, 172:121113, 2021.

[99] C. Rakopoulos, G. Kosmadakis, and E. Pariotis. Critical evaluation of current heat transfer models used in cfd in-cylinder engine simulations and establishment of a comprehensive wall-function formulation. *Applied Energy*, 87(5):1612–1630, 2010.

[100] M. Ramšak. Conjugate heat transfer of backward-facing step flow: A benchmark problem revisited. *Int. j. Heat Mass Transf.*, 84:791–799, 2015.

[101] J. D. Regele, E. Knudsen, H. Pitsch, and G. Blanquart. A two-equation model for non-unity lewis number differential diffusion in lean premixed laminar flames. *Combustion and Flame*, 160(2):240–250, 2013.

[102] A. Remiddi. *Combustion chamber wall heat flux modeling*. Master Thesis, 2019.

[103] C. M. Roth, O. J. Haidn, A. Chemnitz, T. Sattelmayer, G. Frank, H. Müller, J. Zips, R. Keller, P. M. Gerlinger, D. Maestro, B. Cuenot, H. Riedmann, and L. Selle. Numerical investigation of flow and combustion in a single element gch4/gox rocket combustor. *52nd AIAA/SAE/ASEE Joint Propulsion Conference*, 2016.

[104] M. Rudnykh, S. Carapellese, D. Liuzzi, L. Arione, G. Caggiano, P. Bellomi, E. D'Aversa, R. Pellegrini, S. Lobov, A. Gurtovoy, et al. Development of lm10-mira lox/lng expander cycle demonstrator engine. *Acta Astronautica*, 126:364–374, 2016.

[105] R. L. Schacht and R. J. Quentmeyer. *Axial and Circumferential Variations of Hot-gas-side Heat-transfer Rates in a Hydrogen-oxygen Rocket*. NASA CR-6396, 1971.

[106] S. Shanbhogue, Y. Sanusi, S. Taamallah, M. Habib, E. Mokheimer, and A. Ghoniem. Flame macrostructures, combustion instability and extinction strain scaling in swirl-stabilized premixed ch4/h2 combustion. *Combustion and Flame*, 2016.

[107] G. J. Sharpe and S. A. E. G. Falle. Nonlinear cellular instabilities of planar premixed flames: numerical simulations of the reactive navier–stokes equations. *Combustion Theory and Modelling*, 10(3):483–514, 2006.

[108] R. Sibson. A brief description of natural neighbor interpolation. 1981.

[109] S. Silvestri, C. Kirchberger, G. Schlieben, M. P. Celano, and O. Haidn. Experimental and numerical investigation of a multi-injector gox-gch4 combustion chamber. *Transaction of the Japan Society for Aeronautical and Space Sciences, Aerospace Technology Japan*, 16(5):374–381, 2018.

[110] G. P. Smith, D. M. Golden, M. Frenklach, N. W. Moriarty, B. Eiteneer, M. Goldenberg, C. Bowman, R. Hanson, S. Song, W. Gardiner Jr, et al. Gri-mech 3.0. *URL http://www. me. berkeley. edu/gri_mech*, 2000.

[111] J. Song and B. Sun. Coupled numerical simulation of combustion and regenerative cooling in LOX/Methane rocket engine. *Appl. Thermal Engineer.*, 106:762–773, 2016.

[112] G. Strang. On the construction and comparison of difference schemes. *SIAM Journal on Numerical Analysis*, 5(3):506–517, 1968.

[113] D. Suslov, R. Arnold, and O. Haidn. Investigation of two dimensional thermal loads in the region near the injector head of a high pressure subscale combustion chamber. *AIAA Paper 2009–450*, January 2009.

[114] A. G. Tomboulides, J. C. Y. Lee, and S. A. Orszag. Numerical simulation of low mach number reactive flows. *Journal of Scientific Computing*, 12(2):139–167, 1997.

[115] C. Traxinger, J. Zips, and M. Pfitzner. Large-eddy simulation of a multi-element lox/ch4 thrust chamber demonstrator of a liquid rocket engine. In *8th European Conference for Aeronautics and Aerospace Sciences*, 2019.

[116] C. Traxinger, J. Zips, C. Stemmer, and M. Pfitzner. Numerical investigation of injection, mixing and combustion in rocket engines under high-pressure conditions. In *Future Space-Transport-System Components under High Thermal and Mechanical Loads*, pages 209–221. Springer, Cham, 2021.

[117] E. R. Van Driest. Turbulent boundary layer in compressible fluids. *Journal of the Aeronautical Sciences*, 18(3):145–160, 1951.

[118] J. van Oijen, F. Lammers, and L. de Goey. Modeling of complex premixed burner systems by using flamelet-generated manifolds. *Combustion and Flame*, 127(3):2124–2134, 2001.

[119] W. R. Wagner and J. M. Shoji. Advanced regenerative cooling techniques for future space transportation systems. *AIAA Paper 75-1247*, 1975.

[120] D. Wheeler and F. Kirby. *High-pressure LOX/CH4 injector program*. NASA-CR-161342, 1979.

[121] D. C. Wilcox et al. *Turbulence modeling for CFD*, volume 2. DCW industries La Canada, CA, 1998.

[122] F. F. Winter, N. Perakis, and O. J. Haidn. Emission imaging and CFD simulation of a coaxial single-element GOX/GCH4 rocket combustor. In *AIAA-paper*, page 4764, 2018.

[123] P. Wollny, B. Rogg, and A. Kempf. Modelling heat loss effects in high temperature oxy-fuel flames with an efficient and robust non-premixed flamelet approach. *Fuel*, 216:44–52, 2018.

[124] J. Xu, P. Jin, R. Li, J. Wang, and G. Cai. Effect of coaxial injector parameters on lox/methane engines: A numerical analysis. *Acta Astronautica*, 171:226–237, 2020.

[125] J. Yang and J. K. Martin. Approximate Solution—One-Dimensional Energy Equation for Transient, Compressible, Low Mach Number Turbulent Boundary Layer Flows. *Journal of Heat Transfer*, 111(3):619–624, 08 1989.

[126] J. Yuan, Y. Ju, and C. K. Law. On flame-front instability at elevated pressures. *Proceedings of the Combustion Institute*, 31(1):1267–1274, 2007.

[127] Z. Zhou, F. E. Hernández-Pérez, Y. Shoshin, J. A. van Oijen, and L. P. de Goey. Effect of soret diffusion on lean hydrogen/air flames at normal and elevated pressure and temperature. *Combustion Theory and Modelling*, 21(5):879–896, 2017.

[128] J. Zips, C. Traxinger, P. Breda, and M. Pfitzner. Assessment of presumed/transported probability density function methods for rocket combustion simulations. *Journal of Propulsion and Power*, 35(4):747–764, 2019.

[129] J. Zips, C. Traxinger, and M. Pfitzner. Time-Resolved Flow Field and Thermal Loads in a Single-Element GOx/GCH4 Rocket Combustor. *Int. j. Heat Mass Transf.*, 143, 08 2019.